

ALMA MATER STUDIORUM · UNIVERSITY OF BOLOGNA

School of Science
Department of Physics and Astronomy
Master Degree in Physics

Characterization of a prototype for Cone Beam Breast Computed Tomography

Supervisor:
Prof. Nico Lanconelli

Submitted by:
Emma Signorile

Co-supervisor:
Dr. Alessandro Turco

Academic Year 2021/2022

Contents

1	Introduction	3
2	Breast Imaging Techniques	5
2.1	Mammography	5
2.1.1	Screen-Film Mammography	8
2.1.2	Full-Field Digital Mammography	9
2.2	Digital Breast Tomosynthesis	10
2.3	Cone Beam Computed Tomography	12
2.4	Complementary examinations	14
3	Materials and methods	15
3.1	Materials	15
3.1.1	Description of the CBCT device	15
3.1.2	Phantoms	17
3.1.3	Dose meters	20
3.1.4	Spectra simulation toolkit	22
3.1.5	Image J	23
3.2	Methods	23
3.2.1	Characterization of the high voltage generator	24
3.2.2	Spectra simulation	26
3.2.3	Characterization of the detector	26
3.2.4	CBCT reconstruction algorithms	32
3.2.5	Dosimetry	35
3.2.6	Initial setting of the Automatic Exposure Control system . .	41
3.2.7	Image quality evaluation	42
3.2.8	Homogeneity	46
3.2.9	Modulation Transfer Function	46
3.2.10	Geometric accuracy	47

4	Results	50
4.1	Characterization of the high voltage generator	50
4.2	Spectra simulation	52
4.3	Detector	55
4.3.1	Response function	55
4.3.2	Modulation Transfer Function	58
4.3.3	Noise Power Spectrum	69
4.3.4	Detective Quantum Efficiency	72
4.4	Dosimetry	76
4.4.1	Tube output	76
4.4.2	Half value layer	78
4.5	Initial setting of the Automatic Exposure Control	78
4.5.1	Image quality evaluation	85
5	Conclusions	100

Chapter 1

Introduction

This thesis work was carried out in collaboration with IMS Giotto S.p.A., an Italian company active since 1965 and specialized in high-tech systems for the diagnosis of breast cancer.

The project aims to experiment the Cone Beam Breast Computed Tomography (CBBCT) technique using a standard digital mammography system. Clinical studies and scientific literature have reported the equivalence of diagnostic power and an increase in patient comfort for the CBBCT technique compared to existing diagnostic techniques, especially in the case of high-density breasts.

The work is focused on the definition of a protocol of quality measurements for the pre-clinical evaluation of the machine. The tested prototype has been developed as modification of a standard and clinically approved digital mammography device, for a preliminary feasibility study and to be used in a clinical trial, with the purpose of evaluating the sensitivity and specificity of the CBBCT exam in comparison with the actual mammography techniques. This implies the need for compliance with the applicable national and international standards and regulations.

The paper is developed in two parts. The first is specifically concerned with the methods used to define the image quality and dosimetry aspects specific for digital mammography devices. A complete characterization of the system has been performed according to the applicable IEC standards to assure the performances of the equipment and define the quality levels. Due to the lack of a quality control protocol dedicated to CBBCT mammography scanner, a new equivalent test procedure has been proposed.

The second part of the paper is focused on the evaluation, through quantitative and visual analyzes, of the CBCT exam feasibility in the hardware and software conditions currently proposed by IMS Giotto. The prototype was in fact developed differing from the technical choices of competing companies and developed for a different intended use. The main difference with respect to the existing breast CT

scanners is the possibility of performing on the same system the CBBCT scanning but also all the mammographic techniques including Full-Field Digital Mammography (FFDM), Digital Breast Tomosynthesis (DBT), Contrast Enhanced Spectral Mammography (CESM) and Stereotactic and Tomosynthesis Biopsies. In this thesis, we aim to assess whether, in the current setup, considering a dosimetric range very close to that used in the clinic, the tests produce results that can be considered acceptable or at least indicative of the feasibility of the entire project from a commercial point of view. For this purpose, the final reconstruction images, obtained by two previously developed software, are analyzed.

Chapter 2

Breast Imaging Techniques

In medicine, breast imaging is a specialized section of diagnostic radiology that involves imaging of the breasts for screening or diagnostic purposes. According to AIRC (Italian Association for Cancer Research), breast cancer accounts for 30.3% of all cancers that affect women and 14.6% of all cancers. It is confirmed to be the most frequent cancer in the Italian female population. Despite that, the survival rate after five years is very high (87.8%). The possibility of an early diagnosis plays a fundamental role in this process and it is mainly due to innovative tools and a national screening program, which, for this disease, can reduce mortality by 40%. Radiological research, in recent years, has therefore invested its energies in the development of increasingly effective techniques for the diagnosis of breast cancer.

2.1 Mammography

Mammography is a type of medical imaging that uses X-rays to capture images of the internal structures of the breast. It is a radiographic technique which uses low energy x-rays (usually around 30 kVp) to produce images of compressed breast tissue. The goal of mammography is the early detection of breast cancer, so these images are then reviewed for abnormal findings that may be characteristic such as masses or microcalcifications.

Historically, the first radiological images of the breast date back to 1913, when the German surgeon Albert Salomon studied 3,000 mastectomy using x-rays and observing microcalcifications; it was thanks to these radiographic images that he was able to distinguish between cancerous and non-cancerous breast tumors. The radiological investigation for the diagnosis of breast cancer only took off in the 1950s, when mammography was finally promoted as an aid for diagnosis and as a screening tool.

There are, in fact, two main modalities in which this technique is employed: screening and diagnostic. In order to make early diagnosis in asymptomatic women with no personal history of breast cancer, mammography screening is performed as secondary prevention activity. In Italy, screening provides for free mammography every two years for all women aged between 50 and 69. Diagnostic exams are reserved to patients with breast symptoms, changes, or abnormal findings from their screening mammograms. Actually, diagnostic mammography are also performed on patients with breast implants, breast reductions, and patients with a personal or family history of breast cancer.

Until some years ago, mammography, as all the other radiographic imaging techniques was performed with conventional analog methods (film) for image acquisition, analysis and display. This method of mammography acquisition is termed screen-film mammography (SFM). Today, the scenario is almost completely digital. The transition to digital detectors has brought us in the era of Full Field Digital Mammography (FFDM). The passing was much slower in mammography with respect to general radiology. This mainly due to the high spatial resolution demands of mammography and therefore, to the necessity to justify this change by ensuring equivalence with the analog without increasing the dose to the patient or decreasing the diagnostic accuracy. The digitization of the signal has also opened to the possibility of processing the signal for optimization to the display.

Main characteristics

Breast heterogeneous structure includes different types of tissues, but they all fall under the definition of soft tissues. They mainly consist in a more dense glandular structure, surrounded by a background of adipose tissue. The proportion between the two can differ from one person to another. This composition is the main reason why identifying a small tumor in a mammal tissue is difficult. Often it is in fact located in a glandular tissue, which has practically the same absorption coefficient as the tumoral tissue. The tumor is instead more easily identified when it is contained in an adipose tissue (fat).

x-ray mammography is used to detect distortions, asymmetries, masses and clusters of microcalcifications within the breast. Microcalcifications are small calcium deposits embedded in a protein matrix. They present x-ray attenuation coefficients substantially higher than breast tissue and therefore appear as bright spots in the x-ray images. Even though the diameter of a microcalcification is typically below 1 mm, breast microcalcifications present many shapes and sizes. They can be round, linear, coarse or granular. Differently, a mass is a radiological finding demonstrating an increased density versus the surrounding tissue. There is a large variation on mass size and shape. Usually a suspicious mass is larger than 8 mm

and has irregular or spiculated margins.

So, for the soft tissue analysis, both a high spatial resolution and a good contrast are required. In order to increase the contrast between the various structures of interest, that rarely have different attenuation coefficients, moving towards low energies allows for better discrimination. Since the breast is mainly composed of soft tissue and components of interest that rarely have very different attenuation coefficients, moving towards low energies allows for better discrimination (Figure 2.1).

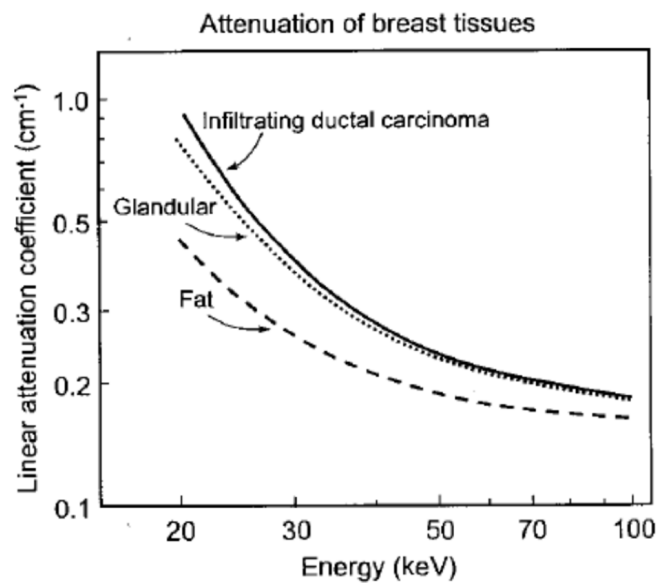


Figure 2.1: Attenuation coefficient of the different breast tissues.

Compression

Breast compression is a necessary part of the mammography examination. The compression plate has function of compressing vertically the breast. Parallel-plate compression has the purpose to even out and reduce the thickness of breast tissue, reducing the tissue that x-rays must penetrate. The amount of scattered radiation is therefore reduced and the image quality increased. Moreover, compression holds the breast still preventing artifacts and blurring caused by the patient movements, and allows a reduction in the required dose for the examination.

Scattering

Scattering is also an important characteristic to correct in mammography. The amount of scatter in mammography increases with increasing breast thickness and breast area, and it is relatively constant with the kVp value. So, without some form of scatter rejection, most of the inherent subject contrast can be lost. The fraction of scattered radiation in the image can be greatly reduced by the use of anti-scatter grids.

2.1.1 Screen-Film Mammography

The screen-film mammography (SFM) was the first technology to be implemented for radiological breast analysis. The device setup is shown below in Figure 2.2 and it is very similar to that of subsequent digital mammograms. It consists of an x-ray tube, a collimator, a compressor and a film cassette on which the image is impressed. The SFM technique requires four separate views and involves changing

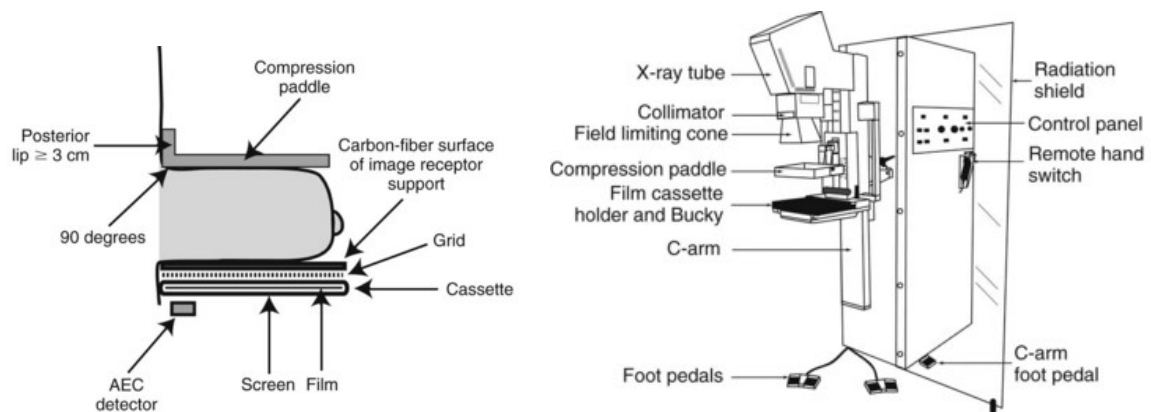


Figure 2.2: Schematic representation of a screen-film mammography device

film between each view. After each acquisition, a considerable amount of time is necessary in order to individually develop and produce the images for display. The developing process can be carried out in a darkroom or, more recently, in an automated film processor. Obviously, SFM suffers from important limitations. Several are the factors that are able to corrupt the image. First surely the day-to-day variability that is inherent in an automated film processor, but also the reduced latitude and the film processing artifacts. Some of these artifacts can be overexposure, underexposure, artifacts, fog, issues with developer or fixer fluid make the images not completely reliable and reproducible.

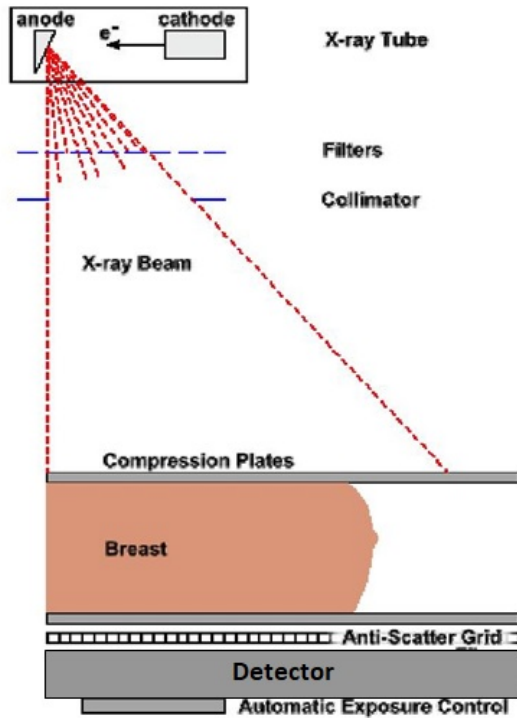
2.1.2 Full-Field Digital Mammography

In the last years, the transition to digital acquisition and storage of images occurred across all fields of diagnostic imaging. Improvements associated with digital diagnostic imaging included ease of acquisition, analysis and display. This transition brought to Full Field Digital Mammography (FFDM).

With FFDM, the mammogram, which is itself digital, acquires, processes and stores electronically all the information. The entire film developing step in the imaging workflow is eliminated and technologists no longer have to stop and change film between images. Digital images are immediately displayed to the medical radiation technologist who can evaluate them and proceed with additional views if necessary; whereas in the analog workflow, the patient is required to wait for potential additional or repeat images while the film images were processed. Given that, the major advantage of FFDM is not only the faster processing time, but the fact that acquisition, processing, display and storage can be performed and optimized independently. So, digital imaging has the ability to enhance image quality by improving the contrast resolution and rely on image processing techniques able to enhance regions of interest by modifying the brightness and/or the contrast of the original image. In particular, the large dynamic range of FFDM allows the use of a more energetic spectra, giving rise to further several advantages such as: a better penetration in dense breasts, a reduction of the average dose and also a reduction in compression necessary to perform the test. So, it is possible to optimize the beam obtaining, especially for thick breasts, an higher SNR selecting harder beams and shorter exposure times.

The bi-dimensional full-field digital mammography (2D-FFDM) technique allows the acquisition of 2D digital projections of the breast. A digital mammography unit consists of an x-ray tube, a generator, a compression system and a detector for the acquisition of projections, as shown in Figure (2.3). There is an anti-scatter grid to reduce the portion of scattered radiation due to the interaction between tissue and x-rays. During the exam, the breast is compressed using a dedicated paddle. In fact, with digital mammography, the exposure variation could be corrected with post-processing, while the breast compression is still indispensable to hold the breast away from the chest wall, to reduce the blur due to physical motion, to reduce the absorbed dose of ionizing photons or to reduce image degrading scatter. So, compression has been, until the present day, a necessary part of the examination.

The breast can be compressed according to two or more inclination angles. The standard mammography views used in screening are the cranio-caudal (CC) and mid-lateral oblique (MLO) projections, shown in Figure (2.4). The 2D technique involves the superimposition of layers of fibroglandular tissues which reduce the visibility of the lesions, giving rise to false negatives. Moreover, in the case of



(a) A schematic representation of a digital mammography system



(b) Giotto Class 30000 device

Figure 2.3: Representation of a 2D FFDM device.

particularly dense breasts, the overlapping of the tissues produces abnormalities, that could also result in false positives and consequent unnecessary recalls of the patients. Compression also helps in separating these overlapping structures.

2.2 Digital Breast Tomosynthesis

The Digital Breast Tomosynthesis (DBT) it is a radiological tomography technique which consists in the reconstruction of a series of "slices", 2D images of multiple breast layers. In fact, while a mammogram usually takes two x-rays of each breast from different angles, the digital tomosynthesis creates a three-dimensional picture showing the breast plane by plane at different depths.

It is a technique that provides a higher diagnostic accuracy compared to conventional mammography. In fact, as said above, one major limitation impacting the performance of 2D mammography is tissue superposition. Both screen-film and digital mammography are x-ray projection studies that produce a two-dimensional radiograph of the three-dimensional breast. Dense glandular tissue located above

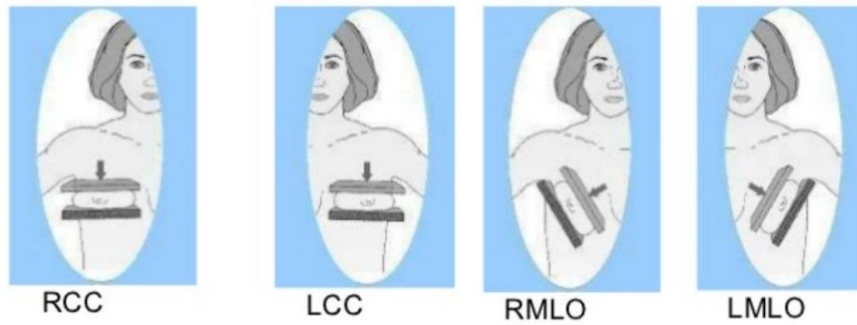
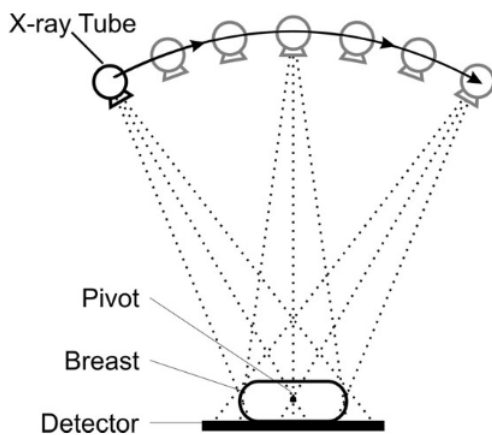


Figure 2.4: Standard mammography views.

and/or below a lesion can occlude or otherwise reduce the visibility of the lesion on the mammogram, and two or more normal features separated in the vertical plane can appear to be a lesion. The former reduces the sensitivity of the study while the latter reduces the specificity.

A tomosynthesis device is structured exactly like a mammography one, but in this case the x-ray tube rotates along an arc, capturing projections of the breast at different angles, as shown in Figure 2.5. A flat panel detector is used and keep



(a) Image acquisition with tomosynthesis (b) Giotto Tomo DBT first prototype

Figure 2.5: Representation of a tomosynthesis device.

stationary during the examination. There is no need of anti-scatter grid. Obviously, in this setup, it is important to carefully consider the dose. The amount of dose emitted for each acquisition in each angle, should be equal to a fraction of the total dose of the equivalent mammogram. This is necessary to ensure that the

patient is not subjected to an overall dose much greater than the recommended one. Also for the same reason, the number of projections should be rather low. As an example the Giotto Tomo device can be considered, developed by the company for the DBT. It exploits thirteen projections made in an angular range ranging from -20° to 20° (Figure 2.5).

Using specific reconstruction algorithms, quasi-three-dimensional images are obtained, partially avoiding in this way, the overlap between the mammary structures. The DBT modality, therefore, allows to obtain better diagnostic performances compared to 2D-FFDM. There is an improvement both in specificity and sensitivity. Respectively, the number of false positives is lower thanks to a clear visualization of the margins and internal structures of the lesion and false negatives are avoided though the identification of very small, hidden lesion. In fact, in 2D imaging the spatial arrangement of tissues cannot be preserved, causing a loss of morphologic information. That is why the detection of small breast cancers can be hampered by the overlapping of the different tissues.

However, also in this technique, compression of the breast remains a necessity, which is limiting in cases of very dense breasts, when the compression can be painful or cause for discomfort. For example in patients suffering from mastodynia or in cases when it is not possible to perform compression following post-operative interventions or due to surgical implants. Furthermore, the diagnostic efficacy of both FFDM and DBT is inversely proportional to breast density.

2.3 Cone Beam Computed Tomography

Dedicated breast Computed tomography (CT) is an emerging 3D isotropic imaging technology for breast, which overcomes the limitations of 2D compression mammography and limited angle tomosynthesis while providing some of the advantages of magnetic resonance imaging. Efforts at building a dedicated CT scanner for the breast date back to the 1970s. Gisvold and his colleagues working with scientists at General Electric (GE), developed the first prototype scanner called CT mammography (CT/M). Due to the immature CT technology the results were terribly disappointing. Long scanning time, relatively low spatial resolution and the used of a sub-optimal detector contributed to images that were not even comparable with the simpler mammograph of the time. New efforts started in the early 2000s in USA. The development of a high-resolution detector and improvement in computational power and reconstruction algorithm were major factors that have contributed to the revival of exploration in Breast Computed Tomography (BCT). And in 2015 Koning BCT machine received the Food and Drug Administration (FDA) approval for diagnostic use. Today, most absorption contrast BCT systems are Cone-Beam Breast CT (CBBCT).

CBCT units are distinguished from CT units in part by their imaging geometry. The x-ray beam in a cone beam unit diverges as a cone to the patient rather than being collimated into a fan beam like in a CT unit. The geometric and acquisition configuration for the cone beam technique are theoretically simple. An x-ray source does a single partial or full rotational scan around a fixed fulcrum within the patient's breast while a reciprocating two-dimensional detector moves simultaneously with the x-ray source. During the scan rotation, each projection image is made by sequential, single-image capture of attenuated x-ray beams by the detector.

Koning BCT consists of an ergonomically designed exam table with a horizontal CT gantry, an x-ray tube and an x-ray flat-panel detector. The examination is performed with the patient lying prone on the exam table. The diagnostic image is then obtained from 300 projections acquired during a 360° scan around the breast. Each with a total scan duration of 10 s. A schematic representation of the setup is visible in Figure 3.1. At present also IMS Giotto is developing a personal CBBCT

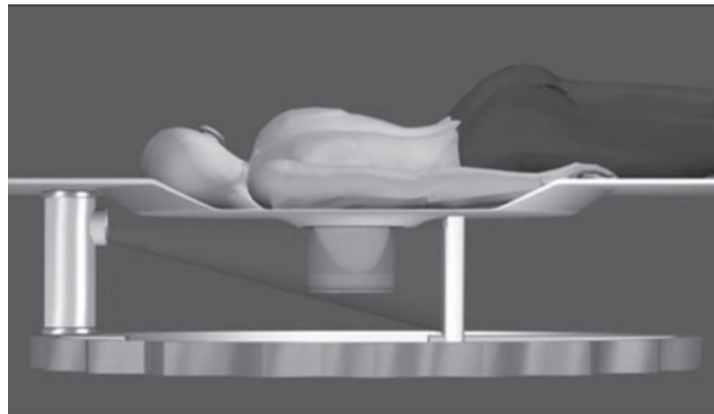


Figure 2.6: Representation of a CBCT exam configuration and positioning.

technique in order to achieve the following benefits:

- Absence of breast compression with increased comfort
- 3D breast visualization with isotropic voxel
- Possibility of detecting difficult masses for dense breasts
- Evaluation of prosthesis integrity
- Skin thickness evaluation
- More accurate assessment of glandularity

- Evaluation of the glandular volume and masses for therapeutic treatments

In fact, even if there are other devices on the market capable of carrying out a CBBCT exam, they are in any case dedicated devices, with a large footprint and high cost. The hope is to obtain a machine that is practical and that, in the final stages of the project, will be able to perform all traditional radiological examinations, such as those already described, and CBBCT, becoming the only one system in the world capable of doing so.

2.4 Complementary examinations

As underlined in the previous paragraph, mammography presents certain limitations, which is why a number of complementary examinations are used to obtain further confirmations and insights. Some of them are:

- **Ultrasound.** This technique is particularly used for young women who usually have denser breasts due to the presence of a greater glandular component. The density of a breast, in fact, is classified according to the relationship between glandular and adipose tissue. The technique is based on the emission of ultrasounds. A transducer is placed in contact with the breast and the echos of the self-emitted sound waves are then studied. Breast ultrasound allows you to distinguish whether a lump is solid or liquid. The big downside is the poor visibility of the microcalcifications. Even if now the technique is mainly two-dimensional, some new 3D devices are in development.
- **Contrast Enhanced Spectral Mammography (CESM)** also known as dual energy mammography technique with contrast medium uses iodized contrast agent, administered intravenously. It involves the acquisition of two low and high energy two-dimensional mammography images, taken before and after the injection, to obtain a subtraction image that allows to reduce the anatomical background noise and highlight the structures in which there is a higher concentration of contrast medium, typically areas where lesions develop. This technique still produces two-dimensional images, involves the use of breast compression and involves a higher dose level due to double exposure.
- **Magnetic Resonance Imaging (MRI).** It's the most sensitive examination existing today in the breast field, with a high diagnostic power. However, it is a technique with very expensive equipment and maintenance costs, long waiting times, and definitely impractical if compared to previous techniques, which is why it is carried out only in selected cases that require it.

Chapter 3

Materials and methods

3.1 Materials

All the materials that were necessary for the analyses carried out in this thesis work are listed below. Their specific characteristics are reported in order to give the reader a complete overview on the materials.

3.1.1 Description of the CBCT device

The design of the Giotto Class CBCT model is based on the Cone Beam Breast Computed Tomography (CBBCT) technique, which, as said above, is revolutionary since it does not involve breast compression. The name derives precisely from the conical beam shape used to scan the breast. The prototype has been developed modifying the Giotto Class model 30000 and introducing a dedicated patient support table device, in order to create a machine able to perform the CBBCT exam. The patient support system is composed of an ergonomic support surface covered with a mattress to improve patient comfort, and equipped with motorized movement to allow easy positioning of the patient directly from the upright position. The device is also equipped with support and protection bars to help the patient during the positioning operation. It will be mechanically coupled to the Giotto base.

In this acquisition system the classical mammography setup is tilted and the patient is placed on the bed in the prone position, with the breast resting on an uncompressed protective cup. A simple representation of the project is shown in Figure 3.1. The device is equipped with an x-ray source consisting of a high-voltage generator and inverter for high frequency (20 kHz) and high power (8 kW) mammography applications. It is also equipped with a metal-ceramic x-ray tube (IAE model XK1016T) with bi-angular rotating anode ($10^{\circ}/16^{\circ}$ - focal spot 0.1/0.3 mm), tungsten track, operating with a voltage between 19 and 49 kV. The

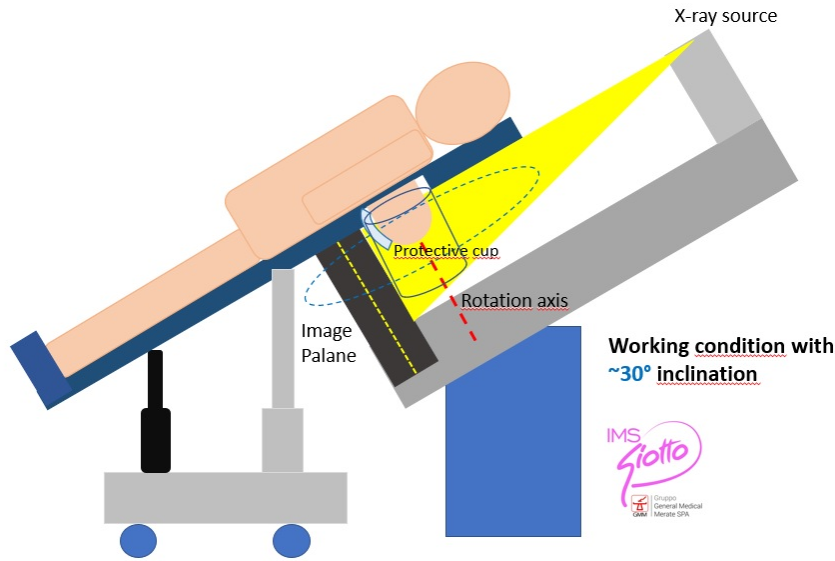


Figure 3.1: Giotto Class CBCT project

inherent filtration of the tube is composed of 0.5 mm of beryllium (Be) and the additional filtration of the x-ray beam is made of 0.05 mm Silver (Ag).

The digital image receptor is an indirect conversion model (Varex model PaxScan 3024MX [®]). It is made of a cesium iodide (CsI) scintillator layer, a layer of amorphous silicon photodiodes (a-Si) and the reading matrix with technology TFT. The sensitive area is $24 \times 30 \text{ cm}^2$ with a square pixel of 0.083 mm side, resulting in an image of 2812×3580 pixels. The acquired projections are reconstructed and processed maintaining a high level of spatial resolution (isotropic voxel of 0.1 mm). The x-ray device operates with a fixed inclination of the gantry (30° with respect to the floor) and is able to perform a rotation of the gantry of 200° for the acquisition of two-dimensional images of breast projection. The acquired projections are then reconstructed and processed with an algorithm that allows high image quality maintaining the high spatial resolution. All the acquired images are displayed by the operator on the integrated Acquisition Work Station (AWS) which allows to enter patient data and transmit them to a Review Work Station (RWS) for interpretation of the reconstructed three-dimensional images.

On the market, two are the devices able to perform a CBCT exam that are approved for clinical use. These have been tested in preliminary clinical studies in order to determine the field of application and evaluate their performance compared to current mammography techniques. In particular the Giotto Class CBCT device exploits some technical aspects that are common to the Koning Corporation device. The similarities consist mainly in the scanning geometry (conical x-ray

beam) and in the comparability of the two x-ray sources (same focal spot size 0.3 mm, same tube voltage limit of 49 kV, comparable anode current range 200 mA). Despite this, however, the two machines have substantial differences. First of all, the dimension of the pixel in the IMS Giotto Class system (83 micron) is lower than the Koning system (100 micron). The 200° scanning technique combined with an iterative reconstruction has the potential to ensure comparable or superior image quality with a reduced number of projections (low dose) compared to the Koning system that uses an analytical reconstruction and a number of 300 projections on a full 360° rotation. Lastly, the speed of the system detector allows Koning (with 30 fps) to use a shorter scanning time (10s) compared to the IMS device (3 fps). The technical data of the Koning device were obtained from the user’s manual for the Koning Breast CT system [26].

3.1.2 Phantoms

A phantom, or imaging phantom, is a highly specialized object utilized in medical imaging for quality control, equipment calibration, dosimetry, and education. Two are the main types of phantom: anthropomorphic and calibration. The first ones are object designed to simulate the patient, made of materials with similar tissue characteristics to normal biological organisms. The latter ones are often cylinders, or plate with known characteristics. They are utilized in quality control to ensure images are reconstructing the imaged phantom in the correct way. In this thesis, phantoms are used in order to evaluate the accuracy of the reconstruction methods, the image quality and to have data necessary for the characterization of the machine.

For the 2D, almost all the test phantoms have a uniform background and include one or more physical objects. The presence of these characteristics aims to produce features in the image able to challenge the performance of the mammography system and provide images suitable for the image quality assessment. The details can either reproduce clinically relevant features, such as small masses, microcalcifications, or include specific objects, like spatial resolution patterns or step wedges, to allow measurements of physical parameters. Commercial image quality phantoms used for 2D mammography are usually made of rigid plastic material, usually poly methyl methacrylate (PMMA), with a thickness that ranges between 20-70 mm to mimic the attenuation characteristic of an equivalent 20-90 mm compressed breast with average glandularity of 50%. (Figure 3.2).

To perform some three-dimensional tests and analyses, specific phantoms were designed and created ad hoc for this project. Their properties are described below.

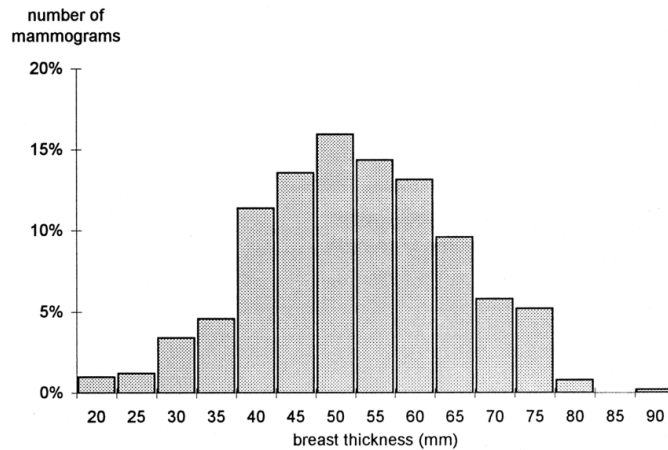


Figure 3.2: Thickness distribution of compressed breasts in the female population

MTF phantoms

There are several methods, and therefore several phantoms, for the evaluation of the Modulation Transfer Function (MTF). Historically, it was obtained measuring the system's Line Spread Function (LSF) using narrow slits. However, this method requires precise fabrication and alignment of the slit and high radiation exposure. Other phantoms have been created for the specific goal of evaluating the system's spatial resolution through the MTF. Among these are the bar-pattern phantom, the wire and the sharp edge devices. The latter is the one indicated in the IEC 62220-1-2:2007 [23] technical standard which establishes the characteristic of the testing object and the procedure, the testing conditions and the analysis method for calculating the MTF to then obtain the Detective Quantum Efficiency (DQE). All the four aforementioned phantoms have been used in the thesis in order to assess the best modality for the detector and CBCT reconstructed image characterization. These objects, their corresponding MTF calculation methods and the results dependence on the acquisition parameters will be compared in the following sections. Here just a brief description of their characteristics can be found.

Bar pattern

Line-pair targets are milled into a 1 mm lead bar. In Figure 3.3 we can see the following spatial frequencies in line pairs per millimeter (lp/mm): 1.0, 1.11, 1.23, 1.37, 1.52, 1.69, 1.88, 2.09, 2.32, 2.58, 2.87, 3.19, 3.93, 4.37, 4.86.

Tungsten wire

This phantom is composed of two 20 μm tungsten wires that have been stretched and slightly angulated in both directions (vertical and horizontal) and fixed within



Figure 3.3: Bar-pattern phantom for the evaluation of the MTF.

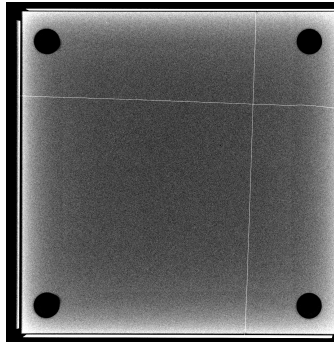


Figure 3.4: Tungsten wire for the evaluation of the MTF. In white the wires that are fixed in two layers of PMMA.

two layers of PMMA with total thickness of 2 cm (Figure 3.4).

Slit camera

The slit camera testing device can be described as a lead collimator with an aperture of $10 \mu\text{m}$.

Edge

This phantom is a simple polished stainless steel block with sharp edge. The dimensions are 120 x 60 x 0.8 mm.

AEC phantom

To try and implement an Automatic Exposure Control (AEC) system, an ad hoc phantom was created. It is entirely made of poly methyl methacrylate (PMMA), it has an height of 15 cm with variable diameters ranging from 6 to 14 cm (Figure 3.5).

Image Quality phantom

The phantom shown in Figure 3.7 was used in the thesis to evaluate the image quality. The phantom has a cylindrical structure, with a height of 7.5 cm and a



Figure 3.5: Composition of the AEC phantom

diameter of 8 cm. Inside, three layers of interest, each necessary for the evaluation of a different aspect of image quality.

The first layer contains the wax insert of the ACR Nuclear Associates model 18-250 phantom, with details of clinical interest (fibers, microcalcifications, masses). The exact composition of this layer is pictured in Figure 3.6. The second layer is composed of a series of 1 mm air holes and it is used for the evaluation of possible geometric distortions. From their eventual distortion in the reconstructed images, it is possible to evaluate the correctness of the scan geometry, and thus, of the reconstruction model. The third is the layer for calculating the MTF and the CNR. This layer contains a PVC insert perforated in the center and therefore constitutes an interface layer of three different materials. The last layer is the one used for the calculation of the NPS and homogeneity and is simply presented as a homogeneous layer without special characteristics. A closer look to the layer composition is in Figure 3.7.

3.1.3 Dose meters

Radiation dose meters are devices that measure dose uptake of external ionizing radiation. In this thesis three different dosimeters were compared and used for the measurements (Figure 3.8). Below, also their specific information can be found (Table 3.1).

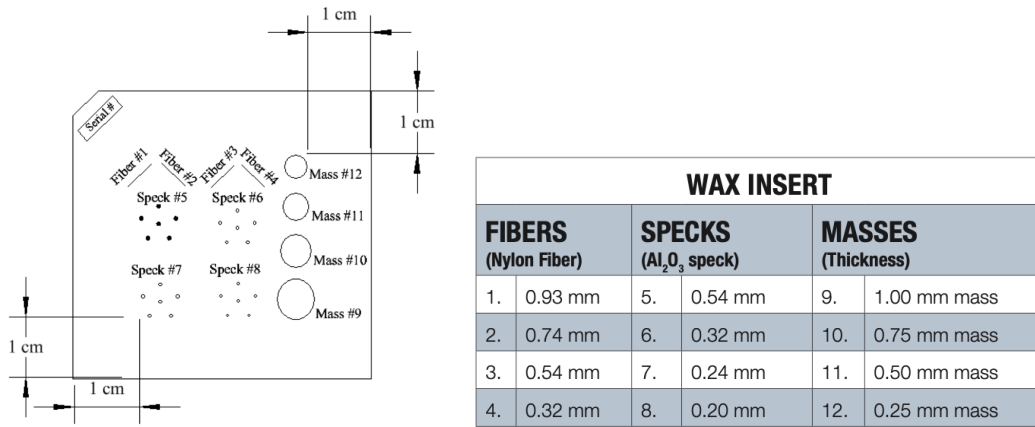
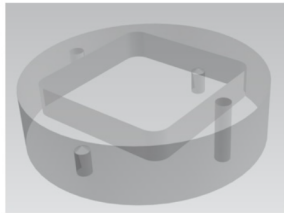
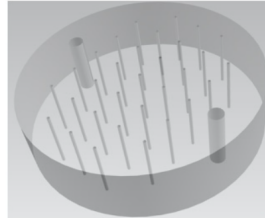


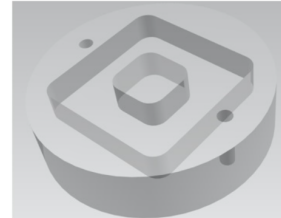
Figure 3.6: Specific composition of the clinical detail layer (ACR 18-250) of the image quality phantom



(a) First layer with wax insert (ACR model 18-250) for the evaluation of clinical details



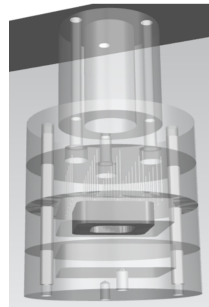
(b) Second layer with 1 mm air holes for the evaluation of the geometrical distortions



(c) Third layer with PVC insert used for the evaluation of MTF e CNR



(d) Fourth layer for the evaluation of homogeneity



(e) Complete view of the phantom

Figure 3.7: Image quality phantom layers



Figure 3.8: The three dosimeters used in the study

	Unfors Xi	RTI Piranha	PTW Nomex
Voltage range (kV)	20–40	20-40	23-35
Air kerma (Gy)	5 μ Gy – 9999 Gy	1 nGy - 1000 Gy	0.5 μ Gy - 500 Gy
HVL (mmAl)	0.2–1.2	0.19-4.3	0.25-0.75

Table 3.1: The table highlights the differences in the specific characteristics of the three dosimeters.

3.1.4 Spectra simulation toolkit

Predicting the x-ray spectra emitted from x-ray tubes has a history going back a 100 yr. It has evolved from an academic pursuit for understanding empirical observation into a practical tool for routine use in hospitals, education, industry, and research. In x-ray diagnostic, in fact, both patient dose and image quality are dependent on the photon energy spectrum used during an exposure. This is why reliable estimations of the emissions from x-ray tubes are sought after for a wide range of tube/filter/geometry configurations covering all the possible clinic operating conditions.

It is often impractical to measure the photon energy spectrum directly from the x-ray tube, this is because specific equipment, precisely determined geometry and a very broad knowledge of the field are required to obtain reliable results. Therefore, a method that is widely used to estimate the emission spectra from an x-ray tube is to simulate the physics behind x-ray production using the Monte Carlo (MC) method. But also this approach has its own flaws. It requires considerable computational resources, and again a detailed knowledge of the imaging equipment and geometry of acquisition. A third approach is to model the x-ray spectra, in a completely deterministic way, with the implementation of a purpose-built software application. In this approach, models of spectra can be derived purely from theoretical principles, based on empirical data, or combine theory with experimental results (semi-empirical). There are a variety of software applications and toolkits

available for use in medical physics.

SpeckPy

SpeckPy [1] is a free Python toolkit for calculating and manipulating x-ray tube spectra. It is compatible with Python language versions 2 and 3 and it requires the standard NumPy and SciPy Python libraries. The program allows the customization of all the acquisition characteristics from the geometry to the materials used for filtering and shielding. With this simulator it was possible to previously analyze a large range of spectra, in various acquisition conditions, in order to cover the entire range of the machine possibilities.

3.1.5 Image J

ImageJ is a public domain Java image processing program. It was developed at the National Institutes of Health and the Laboratory for Optical and Computational Instrumentation (LOCI, University of Wisconsin). The program was released in 1997 and was based on a similar freeware image analysis program: the closed-source NIH Image for Macintosh computers. ImageJ runs either as an online applet or as a downloadable application for Windows, Mac OS, Mac OS X and Linux. It can display, edit, analyze, process, save and print 8-bit, 16-bit and 32-bit images. The program can manage different formats including TIFF, GIF, JPEG, BMP, DICOM, FITS and "raw", moreover it can also support "stacks" (a series of images merged into a single sequence).

ImageJ was designed with an open architecture that provides the possibility to write Java plugins to extend the the basic format of the program. Custom acquisition, analysis and processing plugins can be developed using ImageJ's built in editor and Java compiler. User-written plugins make it possible to solve almost any image processing or analysis problem and allows the creation of customized routines as in the case of this thesis work. The image analysis in the thesis was entirely completed through the use of this specific program. Custom macros have been developed, specific for each type of test, able to automatically put into practice any necessary analysis. The data extrapolated from the images were then quantified and analyzed in order to obtain interesting statistics.

3.2 Methods

This section defines all the analysis methods used first for the characterization of the machine and then for the definition of some tests for evaluating the quality of the image produced by the reconstruction. The measures described below are

directly derived from national and international standards that ensure the performance of mammography machines. Given the difficulty of obtaining a single and perfectly determined protocol, the guidelines to be followed for the analysis of the image and the various phantoms to be used to test it are reported in various European guidelines. In particular, the standards that have been followed are the EUREF protocol [21], IEC 62220-1-2:2007 [23] and EFOMP (both for mammography and dental CBCT) [24] [25]. In 2006 the European Commission, in cooperation with EUREF (European Reference Organisation for Quality Assured Breast Screening and Diagnostic Services), published the 4th edition of the European Guidelines for quality assurance in breast cancer screening and diagnosis. The other protocol that will be taken into consideration in this thesis work, and placed at the basis of the image analysis work, is the EFOMP (European Federation of Organisations for Medical Physics) protocol. EFOMP was founded in May 1980 in London to serve as an umbrella organisation for all NMOs (National Member Organisations).

However, there are no breast CBCT protocols yet. Therefore, the image analysis techniques, for a machine that acts in three dimensions, were developed directly from the protocols of the two-dimensional technique of mammography and semi-three-dimensional one of tomosynthesis but have also been integrated with the protocols of dental CBCT which is the only available protocol for CBCT up to the present day. The need to use as a basis also a protocol already set up for 3D arises mainly from the difference in the size of the voxel which, in tomosynthesis, is different on the xy plane and in the z direction, while in the CBCT it is isotropic. Without these protocols it would not be possible to produce and distribute the machine on the market, nor could it be brought to the stage of pre-clinical tests. Since the prototype developed by IMS Giotto is a mammography machine which however also works in CBBCT mode, some of these measures have been modified and adapted to the specific case of CBBCT. In this section, therefore, the measures that together make up the control and characterization protocol for the CBBCT machine are defined in detail.

3.2.1 Characterization of the high voltage generator

The x-ray generator produces x-rays when an electrical current is applied to it. In particular, high-frequency generators provide superior exposure reproducibility along with the most compact size. The generator is required for delivering, modulating, and regulating the electrical energy required by the x-ray tube (cathode-heating current, tube current, anode drive, and automatic exposure control). The wave form of the tube current as well as the generator power output help determine the radiation yield, exposure time, and image quality.

For mammograms, there is a serious operating limit in the need to have reduced

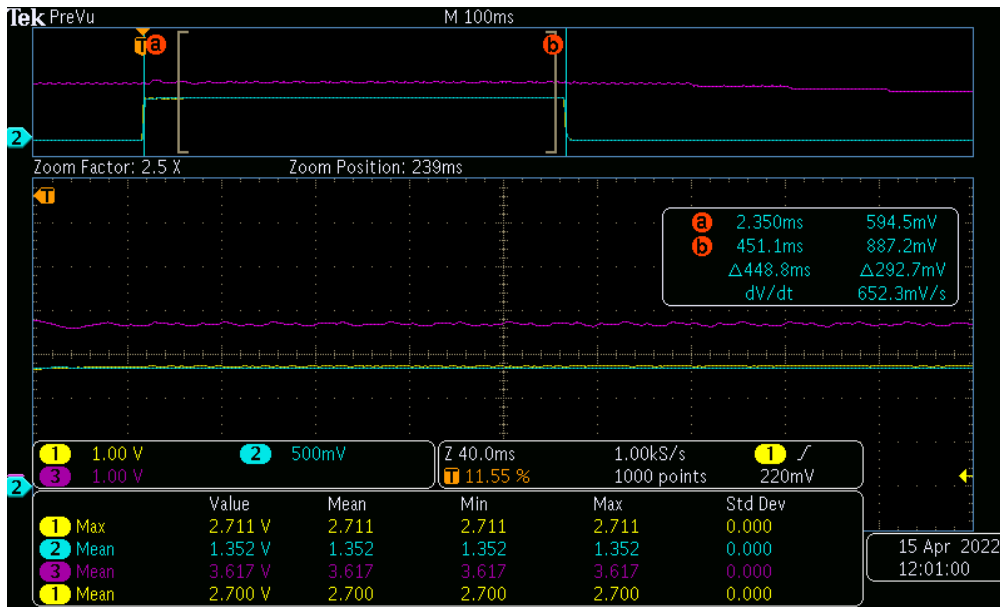


Figure 3.9: Screenshot of the oscilloscope during the acquisition of the measurements for the characterization of the high-voltage generator

exposure times (or high output rates or rather, dose emitted per unit of time) in order to reduce the patient pain as much as possible and to prevent organ movements, which reduce the quality of the diagnostic image.

According to the EUREF protocol, three tests are sufficient to diagnose the operational status of the x-ray tube: the kV accuracy and reproducibility measurements, the x-ray tube emission values efficiency measurements and the exposure time measurement in clinical condition.

To assure the tube voltage accuracy and reproducibility a test device, able to measure kV within the mammographic kV range (20-40 kV) to an accuracy of ± 1 kV and a precision of 0.5 kV, is necessary. Various exposures must be made and then the deviation of the linearized pixel value of this exposures must be evaluated. It is necessary to cover the entire area of the digital detector with a lead or steel sheet in order to protect it from possible ghosts. On the other hand the compressor paddle must be removed.

It was decided to proceed with an invasive measurement, which directly touched a test point linked to the circuit, in order to better characterize the high voltage generator. A voltage divider was used to lower the kV intensity by 1000 times in order to obtain the standard 27 kV. Observing the measures directly from an oscilloscope (Figure 3.9), it was verified that the signal was constant after the initial ramp climb. For all control parameters (kV, mA, filament current and exposure time) obtained from the measurements with the oscilloscope, eight exposure were

made for each value using the W/Ag target/filter combination and at least 30 mAs.

3.2.2 Spectra simulation

Using the SpeckPy toolkit, some simulations were carried out in order to characterize the tube and the spectrum of the device. The parameters that have been kept fixed in the various simulations are shown below. They account for the intrinsic characteristics of the tube and of the geometric setup.

- Tungsten (W) anode with a 16° angle
- Intrinsic beryllium (Be) filtration of 0.5 mm from the output window of the x-ray tube
- Air filtration of 690 mm between the detector and the skin entrance point
- Silver (Ag) filter of 0.05 mm

With these initial parameters set, the simulations were carried out in a range from 35 to 49 kV with a 1 kV step.

From these simulated spectra the average energies and the Half Value Layers (HVL) were then obtained. HVL can be defined as the thickness of absorber which attenuates the air kerma of a non-monochromatic x-ray beam by half.

These spectra simulations were then validated through the use of three different dose meters. The validation has the purpose to assess the distance between simulated and measured data in order to know how reliable the simulations can be considered. The radiation quality of the emitted x-ray beam is determined by tube voltage, anode material and filtration. However, various dose meters have different sensitivities to forward scattered radiation from the compression paddle. For this reason, it was decided to compare three different models and evaluate the differences in the values obtained, so as to characterize the system with greater precision. The same experimental setup is proposed for the measurements, independently of the dose meter type. Figure 3.8 show the dose meters used for the measurements: Unfors Xi, RTI Piranha and PTW Nomex. Measures were taken with the detector shielded by a metal plate and with the dose meter fixed ensuring that the sensitive area is located at 6 cm from the chest wall edge of the breast support and laterally centered, as to meet the standards requirements.

3.2.3 Characterization of the detector

The image detector performance could, theoretically, be fully characterized applying the Linear Shift-Invariant (LSI) system theory. LSI describes how a system

(the image detector) acts on the input signal to produce the output (the image itself) via the transfer function. This theory can only be considered true if two main constraints are met: there must be a linear proportionality between input and output and the response must not depend on what position of the detector the response is measured at (shift-invariant). The latter can be assumed also if limited response intervals and limited areas are considered.

Since we are dealing with the real world and real detectors, it is not possible to fully transfer the input signal into the output image without introducing noise and losing part of the signal. Hence, the physical characterization of transfer properties of an image detector has to be done in the spatial frequency domain both for the signal (using the modulation transfer function) and the noise (using the noise power spectrum). From these measurements, the Detective Quantum Efficiency (DQE) is then derived.

The acquisitions that are reported in this section were carried out both in mammography (FFDM, low gain) and tomography (DBT, high gain) modality, keeping the acquisition angle fixed at 0° . While the images acquired in DBT mode are already 11 images (coming from the 11 projections), the images in FFDM mode were repeated 4 times to have more average values. In this way, what is characterized is the detector and the characteristics linked to the 2D planar images.

All the measurements described in this section are acquired removing the compression plate from the x-ray beam. In the EUREF protocol, the measurement procedure is described with the same x-ray spectrum used for a standard image, but with the addition of 2 mm of Al at the x-ray tube. All the measures done for MTF, NPS and DQE respected this indication.

The characterization is entirely carried out for both detectors available IMS Giotto company in order to carry out a comparison between the two and to motivate the final choice of the model mounted on the prototype. The first one is the Varex PaxScan® 2530DX indirect conversion detector with amorphous silicon technology (a-Si) and cesium iodine (CsI) scintillator. The second one is the Analogic ScreenPlus direct conversion detector, based on amorphous selenium technology (a-Se). For practical reasons it was not possible to install the two detectors on the same CBCT system. Two different systems were therefore used: a two-column and a single-column device that have been considered equivalent. This equivalence is justified because the two machines have the same radiative source and the same acquisition geometry with fixed distance between focal spot and image plane. Furthermore, the usage of the anode trace, which determines the emission efficiency of the tube, is also comparable. We remember that the efficiency can be defined as the output dose per unit of mAs. Because of that, the two different systems can be used in that the emissions are similar.

Response function

The first quantitative analysis that has to be performed is to check the consistency of the response function with the expected trend (linear in this particular case). The response function relates the air kerma at the detector input plane to the pixel value. It is used for the linearization of the images from which the quantitative image quality metrics are calculated. It allows the identification of the dynamic range, the range of exposure over which a meaningful image can be obtained.

A set of specific mAs values to consider in the measure was established according to the protocols. In these, it is specified how it is really important to sample low mAs settings more finely. This both because the linearity can be worse at low mAs values, and because it is likely that those will be used for the NPS estimation. Flat-field images were acquired according to Table 3.2. The mean pixel value and

FFDM	DBT	
mAs	mAs	kV
		24
		26
2, 4, 10	22, 44	28
20, 40	66, 88	30
		32
		34

Table 3.2: Exposure time and voltage values at which flat-field images have been acquired.

the standard deviation in the reference ROI on the unprocessed image must be measured. Then, the mean pixel value has to be plot against the entrance surface air kerma. The linearity has to be determined by the evaluation of the best fit through all measured points and the calculation of the square of the correlation coefficient (R^2).

Modulation transfer Function

Modulation Transfer Function (MTF) is a measure of the ability of an imaging detector to reproduce image contrast from subject contrast at various spatial frequencies. It progressively decreases with the increasing of the spatial frequency but it is normalized to unit at zero spatial frequency by convention.

There are several methods, for the evaluation of the MTF. Historically, it was obtained measuring the system's Line Spread Function (LSF) using narrow slits. However, this method requires precise fabrication and alignment of the slit and

high radiation exposure. Other methods include the use of a bar-pattern, a wire or a sharp edge device. The latter is the one indicated in the IEC 62220-1-2:2007 protocol which establishes the method of calculating the MTF and NPS to then obtain the Detective Quantum Efficiency (DQE). Despite that, a meticulous analysis of the various calculation methods was followed in this thesis to choose the most suitable to calculate the MTF not only of the 2D characterization detector, but also for the calculation of the MTF in the 3D case later on, in order also to fully understand the protocol's choice of edge.

The measurement of MTF through the use of the edge test device was first introduced by Samei in 1997 [12]. The article introduced the possibility to determine the MTF with the measurements of the Edge Spread Function (ESF) using an opaque object with a straight edge. In the IEC 62220-1-2 this method is the one indicated for the measurement and also in this thesis work it will be the one followed for the analysis.

The pre-sampling MTF must be determined along two mutually perpendicular axes and, for its determination, the complete length of the ESF must be used. The integer number (N) of lines following the lateral shift of the edge in the direction of the line is determined. This most closely corresponds to the pixel sampling distance. The method that is used in order to determine it is described as follows. The first thing is to determine the edge tilting angle (α). N is then calculated as $N = (\frac{1}{\tan\alpha})$ accurate to integer precision. The pixel value of the linearized data of N consecutive lines across the edge are used to generate an oversampled edge profile or ESF. To calculate the average ESF, this procedure is repeated for other groups of N consecutive lines along the edge. The average of all edge spread functions is determined, and the MTF is calculated based on this averaged oversampled ESF. The sampling distance in the oversampled ESF is assumed to be constant and is given by the pixel spacing (Δx) divided by N. From this, the Line Spread Function (LSF)

$$LSF(x) = \frac{d}{dx}ESF(x) \quad (3.1)$$

is computed and the modulus of its Fourier Transform yields the MTF.

$$MTF = |F[LSF(x)]| \quad (3.2)$$

The acquisition setup has been considered the same for all the explored methods and according to the standards. A 2 mm Al foil has been put between the tube and the detector and the grid was removed. We therefore went to investigate all the possible influences deriving from the acquisition method on the results of the final MTF curve. The aspects investigated are: the positioning of the object with respect to the pixel matrix in terms of angular rotation and distance between the chest wall side of the detector. Also the impact of the exposure parameters i.e.

beam energy (kV) and dose (mAs) was evaluated together with the dependency from the gain modality of the detector.

Noise Power Spectrum

The noise power spectrum (NPS), also known as the power spectral density, of a signal, is the Fourier transform of the noise autocorrelation. It gives the intensity of noise as a function of the spatial frequency. So, it can be thought of as the variance of image intensity distributed among the various frequency components of the image. The NPS can play an important role in the study of reconstruction algorithms or other parameters that can influence the performance of small object detection. Despite that, it is not easy to determine a simple method for an NPS quantitative evaluation and the consequent definition of acceptance thresholds. The amount of noise present within an image strongly depends on the level of the exposure used for acquiring the image itself. NPS is computed from uniformly exposed images acquired at different exposures.

IEC 62220-1-2:2007 defines an area of 50 mm × 50 mm for the NPS estimation, divided into ROIs of 256 × 256 pixels that overlap each other by 128 pixels. The Fourier transform of these various windows is computed and square modulus are averaged on the ensemble. From this, the one-dimensional NPS is derived.

$$NPS(u, v) = \frac{\Delta_x \Delta_y}{M 256 256} \sum_{m=1}^M \left| \sum_{i=1}^{256} \sum_{j=1}^{256} (I(x_i, y_j) - S(x, y)) e^{-2\pi i(u_n x_i + v_k y_j)} \right|^2 \quad (3.3)$$

In this formula, as said above, a ROI dimension of 256 x256 pixels has been considered. M is the number of ROIs, Δ_x is the pixel spacing in the x direction, Δ_y is the pixel spacing in the y direction, $I(x_i, y_j)$ are the (linearized) pixel data, $S(x, y)$ is a 2-dimensional polynomial function fitted to the entire extracted region used for the NPS analysis (not to the individual ROIs).

Obliviously, the spectra sectioned from the 0° and 90° axes have to be recorded separately. The axes, in fact, contain information about axial structured noise. The spectral ensemble is then normalized to give the Normalized Noise Power Spectrum (NNPS) dividing by the mean pixel value of the linearized flood image. After evaluating that the NNPS in the directions of the two axes is sufficiently superimposable, the radial NNPS from the horizontal and the vertical component can be obtained.

The acquisition configuration is the one proposed in the IEC 62220-1-2:2007 standard and does not contains the anti-scatter grid. This is particularly important in order to not introduce structured noise, predominantly of low spatial frequencies, that can be seen along the axes. The grid, due to its spatially periodic nature, could also introduce spikes, indicating increased noise power at distinct spatial

frequencies.

Measures were made to go deeper into the physical characteristics of the NPS measurement. To establish the degree of dependence of the NPS on the variation of the spectrum, the voltage and mAs were varied according to Table 3.2. Again, as described in the Section 3.2.3, four images for each combination were acquired in the FFDM modality, while for the DBT the angle was kept fixed at 0° in order to already have eleven images.

Detective Quantum Efficiency

Detective Quantum Efficiency (DQE) is one of the fundamental physical variables related to image quality in radiography and refers to the efficiency of a detector in converting incident x-ray energy into an image signal. DQE is one of the best and most widely accepted overall measures of detector image quality performance. The DQE is calculated from the MTF and the NPS with the following formula.

$$DQE(n, v) = \frac{MTF(n, v)^2}{(K_i SNR_{in}^2) NNPS(n, v)} \quad (3.4)$$

As explained in the previous sections, MTF and NNPS (Normalized Noise Power Spectrum) can be calculated directly from the image. K_i is the estimated air kerma at the detector surface and SNR_{in}^2 is the number of x-ray photons ($\mu Gy^{-1} mm^{-2}$) for the beam quality used. Therefore, $K_i SNR_{in}^2$ gives the total number of x-ray photons at the detector input. The dose arriving at the detector (K_i) is directly estimated with the dosimeter. The SNR_{in}^2 value is instead directly tabulated in the IEC 62220-1-2:2007 standard. However, the IEC standard does not provide a table for devices that use the tungsten/silver (W/Ag) combination as anode and filter. Therefore, since the IMS device mounts this device configuration, the SNR_{in}^2 value was calculated from some spectra simulations according to the data of Boone and colleagues (Boon et al., 1997 [27]) using the formula:

$$SNR_{in}^2 = \int \frac{\Phi(E, V)}{K_i} dE \quad (3.5)$$

where $\Phi(E, V)$ is the photon fluence at energy E when a tube voltage V is applied. The simulations were conducted with the same toolkit already described in Section 3.2.2. The simulation configuration that was considered for the calculation of the DQE simulates the conditions in which the measurements for the calculation of the MTF and NPS were taken. From these simulations the fluence value was obtained for the calculation of the SNR_{in}^2 value according to the above formula.

3.2.4 CBCT reconstruction algorithms

As previously mentioned, the CBCT technique consists in acquiring various projections on an angle of more or less 360° around the object of interest (in this case the breast). This implies that, to obtain the final image (or rather the final set of images) to be presented to the doctor, the information coming from the various projections must be grouped and a reconstruction algorithm will allow the final visualization of the object.

The projection on an object obtained during a radiographic examination reflects the absorption of the photons that make up the x-rays. Therefore, the reconstructed images represents nothing more than a map of the attenuation coefficients of the object that the rays have crossed. Considering a monochromatic beam with parallel rays, the model that describes the attenuation is the Beer-Lambert law.

$$m(w) = m_0 e^{-\mu w} \quad (3.6)$$

where w represents the point of the object crossed by the beam, $m(w)$ is the beam intensity exiting from that point and m_0 is the beam initial intensity, while μ represents the attenuation coefficient of the object that depends on the object material.

Considering a tomographic measurement process at a given angle θ , his projection is a set of line integrals. A set of many of these projections, under different angles, organized in two dimensions is called a sinogram. Data that make up the sinogram derive from the Radon transform. This is the integral transform which takes a function f defined on the plane to a function Rf defined on the (two-dimensional) space of lines in the plane, whose value at a particular line is equal to the line integral of the function over that line. So, if a function f represents an unknown density, then the Radon transform represents the projection data obtained as the output of a tomographic scan. Hence, the inverse of the Radon transform can be used to reconstruct the original density from the projection data. That is why to reconstruct the image from the sinogram, the inverse Radon transform is applied to the image. Figure 3.10 shows the process of acquiring projections in the two-dimensional case. A single projection is represented by the yellow line. A set of projections is obtained by scanning the object according to several angles; θ is therefore varied in a certain angular range, which depends on the system. The graphic representation of the projections as the angle varies is called sinogram and is shown in the image on the right.

Starting from this mathematical formula, many reconstruction techniques have been developed to calculate the inverse transform. The three that have been considered and developed for the CBCT project are explained below.

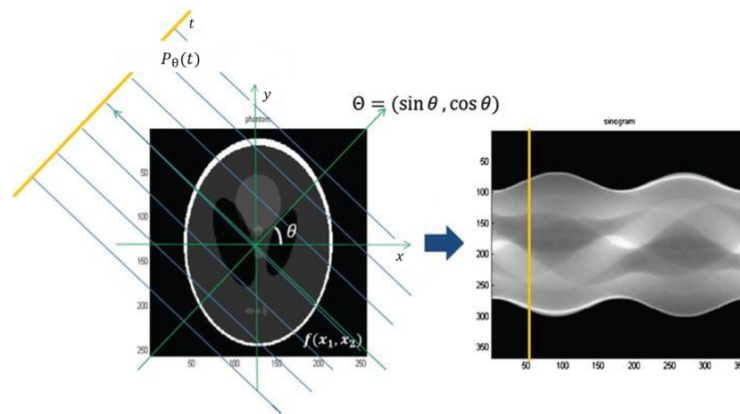


Figure 3.10: Example of a Sinogram resulting from a two-dimensional scan of the Shepp-Logan phantom, widely used for computed tomography tests.

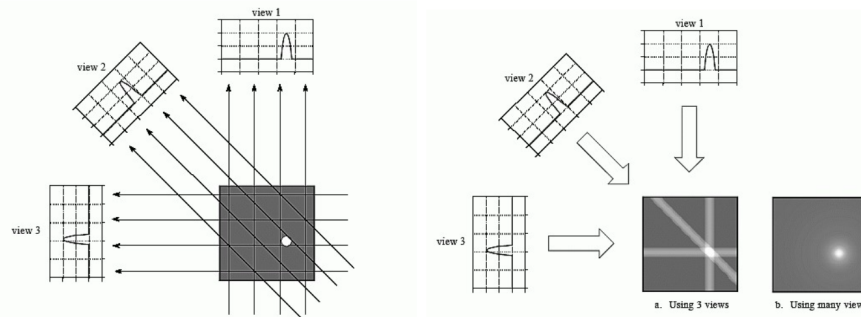


Figure 3.11: Operation of a FBP algorithm. In the first image the projections of a dot are acquired according to three different angles, in the second the data is rear-projected. It is noted that as the number of angles increases, the reproduction is more accurate.

Filtered Back Projection

The most common and simple among the three methods is the Filtered Back Projection (FBP). The basic idea is the re-distribution of the filtered data, acquired at a certain angle θ , along the same lines from where the photon was emitted from, and then add the contributions for each θ . The concept of back-projection is clearly explained in Figure 3.11. The whole process is articulated in few steps. First, the projection of the original data and the formation of the sinogram, then the transformation of those data in the Fourier domain. After that, the data are filtered in the Fourier space and then, they are transformed back into the spatial domain with the inverse Fourier transform. At last comes the proper back-projection. Filtering is necessary in order to fight the intrinsic effect of back-projection of

amplifying low-frequency signals and the inherent noise in the data due to the random nature of radioactivity itself. So, the filtering has the purpose to smooth out the statistical noise. For time reasons, the filtering action is carried out in the Fourier space. In this way the whole process is less time-consuming.

The FBP algorithm was the first method implemented for the reconstruction of tomographic images and is still used today in some commercial software mainly for its ability to produce images in a very short time, an essential feature in a medical context. However, it is known that it presents some problems. To obtain an high-quality image it is necessary to have a particularly high number of projection angles. This is not achievable in a practical context otherwise the dose delivered to the patient would be too high. With a limited number of angles, the algorithm produces images corrupted by artifacts and noise, affecting the quality.

Iterative methods

To overcome the limitations of FBP, new models of the problem based on the discretization of the Beer-Lambert law (Formula 3.6), were introduced, more accurate with respect to the image formation process. Utilising these models it is possible to obtain a quantitative image reconstruction and noise reduction.

Iterative methods refer to certain image reconstruction algorithms that begin with an image assumption, and compare it to real time measured values while making constant adjustments until the two are in agreement. Iterative reconstruction has three distinct stages. Using the raw data a standard filtered back projection algorithm (FBP) is utilized to create a primary image. After that, a forward projection to the primary image creates artificial raw data, simulated data is then correlated to the measured raw data where an updated image is generated, and then a filtered back projection is used to back-project the updated image onto the new updated image. This is repeated until the differences in the images reach a preset value. The massive change with respect to FBP is that there is no need of explicit mathematical expression for the inverse transformation. These algorithms are very flexible to adapt to different imaging geometries.

In this thesis two different iterative methods, also compared to the simple FBP, were used to test the reconstruction of CBCT images. A very brief description of these methods follows. A more formal mathematical description can be found in a previous thesis work [16].

FISTA

Among the most popular iterative methods there is the ISTA method (Iterative Shrinkage-Thresholding Algorithm). It is a proximal-gradient method, a generalization of the classic descent gradient algorithm. The FISTA (Fast Iterative Shrinkage-Thresholding Algorithm) method consists of an acceleration of the ISTA

method. FISTA is a first order optimization method, but with the speed of quadratic convergence. This is the feature that makes it more advantageous.

PDHG

The primal-dual algorithm, known as Primal Dual Hybrid Gradient (PDHG), was proposed by Chambolle and Pock as a first order method for solving non-differentiable convex optimization problems. The PDHG algorithm essentially consists of a gradient ascent step in the dual variable y and a gradient descent step in the primal variable x , followed by further relaxation of the primal variable.

3.2.5 Dosimetry

Many are the testes that can be performed on the x-ray source, but those which are considered necessary are those related to patient dose estimation. Therefore, in this section the measurements that will be taken into account are: the tube output, measured at known distance from the source, and the Half Value Layer (HVL) or beam quality, which characterizes penetration capability of a polychromatic x-ray beam.

The acquisition setup does not require the compressor to be mounted on the machine. This is done to estimate the incident dose at the patient's breast under the same conditions in which the examination will be performed. In CBCT the breast is in fact pendant and does not require compression. The image detector must be shielded with a metal plate in order to not impress a ghost image on it. The dose meter must be fixed ensuring that the sensitive area is located at 6 cm from the chest wall edge of the breast support and laterally centered. Since both measurements (tube output and HVL) depend on the selected x-ray beam (anode/filter combination and kVp value), in principle, it would be necessary to measure both parameters for each x-ray beam used in the clinical practice.

Tube output

The x-ray tube output, $Y(d)$, is the quotient of the air kerma at a specific distance (d) from the x-ray tube focus, by the tube current-exposure time product, also called tube loading and usually expressed in units of mGy/mAs or $\mu\text{Gy/mAs}$. The x-ray tube output permits the calculation of the incident air kerma (K_i) if tube loading (mAs) and compressed breast thickness are known.

Incident air kerma is the kerma to air from an incident x-ray beam measured on the central beam axis at the position of the patient or phantom surface. It includes only the incident radiation. On the contrary, the entrance surface air kerma (K_e) is obtained from the incident air kerma multiplied by the backscatter factor.

Therefore, through these measures, the purpose is to estimate the tube output in

units of $\mu\text{Gy}/\text{mAs}$, at known distance from the x-ray tube focus for all the spectra clinically used.

Half value layer

As mentioned above, the HVL (Half Value Layer) can be defined as the thickness of absorber which attenuates the air kerma of a non-monochromatic x-ray beam by half. Measures were taken in the setup described above in order to estimate the HVL in units of mmAl for all the x-ray spectra clinically used. The HVL value is in fact read directly on the dose meter. Traditionally (as described in the EUREF and EFOMP protocols) the HVL values should be obtained with the addition of thin aluminum foils on the compressor and reducing the collimator aperture to have only the dose meter in the exposed field. For reasons of practicality and accuracy of measurement, it was instead preferred to take the values directly from the solid-state digital dosimeter. In fact, it has been verified that the latter is more repeatable and accurate since the error relating to the thickness of the sheets and the dose value measured in the traditional case is greater.

Estimation of the Mean Glandular Dose

Dosimetry is a fundamental aspect in mammography context. As discussed above, dose is the main concern in the context of mammography examinations. This aspect is only amplified in the context of a CBCT exam where the greater number of projections and the dose administered for each projection, makes available a large amount of information for reconstruction, which leads to a new image capable of giving a new perspective to the breast exam. Despite that, it is desirable to keep the dose absorbed by the patient as low as possible for a specific diagnostic purpose. The international organization that deals with radiation protection is the International Commission on Radiological Protection (ICRP). According to the ICRP, the radiation protection system is based on three fundamental principles:

- principle of justification: any decision that alters the radiation exposure situation must bring more benefits to the individual than harm;
- principle of optimization: doses should be kept at the lowest level reasonably obtainable, taking into account the economic and social factors (also known as the ALARA principle - As Low As Reasonably Achievable);
- principle of dose limitation: the total dose for each individual must not exceed the limits prescribed by the legislation.

These principles summarize the basic concept of a low but sufficient dose for the examination to lead to satisfactory results. The goal is, therefore, to find the right

compromise between the quality of the reconstructed image and the amount of radiation.

Dose and number of projections in the Giotto Class CBCT device are chosen so that the amount of radiation absorbed is not greater than that corresponding to a double-view mammogram and that microcalcifications with a diameter of at least 250 μm can be seen.

In the discussion about dosimetry, it is therefore necessary to consider the average glandular dose. Also known as Mean Glandular Dose (MGD), it is the quantity used to describe the absorbed dose of radiation to the breast in mammography and is the preferred measure of the potential risk from mammography. This value is in fact reported to estimate the dose that was given to the patient during the examination. MGD is used to determine diagnostic reference levels on mammography exposures by national and international organization. For a standard breast (defined as 4.2 cm thick when compressed, with a 50:50 ratio of glandular tissue to fat), the MGD has different values according to the type of exam under consideration. The EUREF limit is set at 3 mGy per view for a single screening mammography exam for 50 mm of compressed breast [21]. In particular, for IMS machines MGDs for the standard breast (50 mm) are:

- $\simeq 1$ for digital screening mammography (FFDM);
- $\simeq 1.5$ for tomosynthesis (DBT);
- $\simeq 2.5$ for combined modality FFDM + DBT (COMBO);
- $\simeq 3$ for magnification modality (MAG);
- $\simeq 2$ for contrast enhanced spectral mammography (CESM).

The listed scale factors are usable for all thicknesses. In Figure 3.12 it is possible to see the trend of the MGD for different breast thicknesses. The EUREF limit is dashed in red.

The MGD is a function of the breast thickness, its composition and also the quality of the radiation. Since it is impossible to know the exact conformation of the patient's breast, Dance [28] has estimated some factors which, based on different Monte Carlo simulations, allow the calculation of the dose to the patient. From a measured incident air kerma at the upper surface of the breast (K), MGD can be calculated as follows:

$$MGD = Kgcst \quad (Gy) \tag{3.7}$$

g corresponds to a glandularity of 50% and is obtained according to the known breast thickness (obtained from the compression height) and the HVL. c corrects

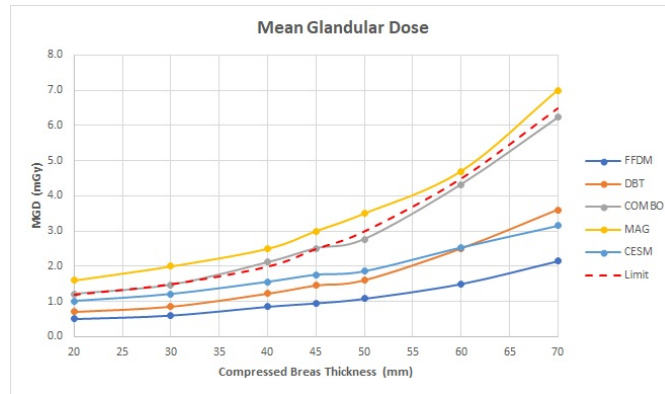


Figure 3.12: MGD in mGy for different compressed breast thicknesses and different examination modalities. The EUREF limit per view for a single screening mammography exam is dashed in red

for the difference in composition of typical breasts from 50% glandularity and is given for typical breasts in the age range 50 to 64. s corrects for the x-ray spectra in use and refers to a table of different target/filter combinations. t is the correction factor of the incidence angle of the x-ray tube for DBT exams. The tables which indicate the factors c , g , t and s for compressed breasts simulated with PMMA obtained from the simulations of Dance et al. reported in the EUREF document. Given the need for compression in order to extrapolate factors g and c , a problem arises in using this method for estimating the mean glandular dose in the case of CBCT. In the standard technique, the Monte Carlo simulations conducted by Dance et al. consider the compressed breast. In fact, not only the thickness is extrapolated from the compression paddle height, but also the tables themselves are calibrated on compressed breast composition. Therefore, the extrapolated factors can be used only in case of a compressed breast and would be completely incorrect to consider in the pendant breast configuration. For this very reason, it was necessary to create a new way to estimate the average glandular dose.

The whole construction of the MGD estimation method for the CBCT starts from an article by Sarno et al. published in 2018 [13]. This team, working on an equivalent machine (Koning Corp. cone-beam BCT apparatus), have obtained two datasets of coefficients for monoenergetic and polyenergetic spectra for the calculation of the MGD. These coefficients were estimated, in the article, through Monte Carlo simulations in a range from 4.25 to 82.25 keV. The pendant breast was modelled as a cylinder composed of an homogeneous mixture of adipose and glandular tissue. Different glandular fractions have been considered (glandular fractions by mass of 0.1%, 14.3%, 25%, 50% or 100%) with a diameter varying between 8 and 18 cm. Defined the geometry, for a fixed anode/filter combination,

several coefficients were computed in order to cover a broad range of x-ray beam HVL. The tables resulting from the study are shown in the Appendix.

Since the analysis carried out in the paper is restricted to certain simulated breast sizes and HVL values, it was not possible to directly utilize those coefficients. The Koning machine operates, in fact, at higher energies with respect to the IMS one. This results in tables with HVL values that are far from the one obtainable for the machine under development. To expand the results and obtain a wider range of values both for the HVL values and for the breast sizes, linear trend lines were scrambled from the tables obtained in the paper. The linearity of the trend was assumed even at much lower energies such as those of the CBCT project. Therefore, the steps of the reasoning that have been followed are:

- Calculation of the DgN_{CT} as a function of the HVL
- Calculation of the tables of linear fit parameters $m\%$ and $q\%$ as a function of the glandularity for the various cm of diameter
- Calculation of the 3 values of DgN_{CT} for $h/r = 1, 1.5$ and 2 as a function of the breast diameter
- Calculation of the final value of DgN_{CT} as a function of the morphology (r and h) of the breast

Once the conversion factors (DgN_{CT}) necessary for the MGD calculation have been obtained and corrected for the experimental setup of the IMS machine, it is necessary to calculate the dose entering the rotation axis. In the CBCT case, in fact, there is no meaning in mentioning the skin entrance dose because the machine rotates 360° around the pendant breast. Therefore, to estimate the dose given to the patient it is necessary to consider the machine rotation axis. The acquisition geometry is shown in Figure 3.13. The final dose value entering the rotation axis ($ESAK_{SRD}$) is calculated with the following formula:

$$ESAK_{SRD} = \frac{mGy}{mAs} mAs d \quad (3.8)$$

where d is the distance factor, calculated in $(\frac{dm}{SRD})^2$ where dm is the distance used for the measurements and SRD is the source-rotation-distance. The first term, calculated in $\frac{mGy}{mAs}$, is the tube efficiency calculated obtained from the tube output measurements (Figure 4.28).

Some parameters, such as the speed of the detector, are fixed, while on others it is possible to act in order to obtain, by modifying them, a better ESAK. Among these parameters we find the rotation speed, which obviously has an effect on the rotation time and on the number of projections. The other thing that can be

- SID = Source-to-Image Distance
- SRD = Source-to-Rotation Distance
- RID = Rotation-to-Image Distance
- FibID = Fiber -to-Image
- Air Gap = Object-to-Fiber distance

$$M = \text{SID}/\text{SRD}$$

$$\varnothing_{\text{FOV}} = (\text{RID} - \text{FibID} - \text{Air Gap}) \times 2$$

$$H_{\text{FOV}} = H_{\text{Detector}} / M$$

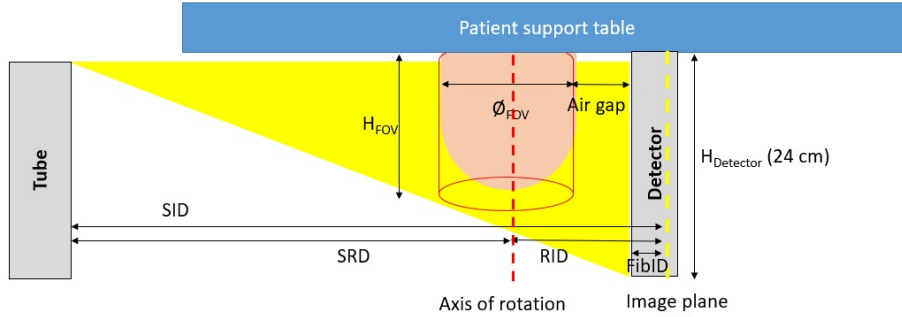


Figure 3.13: Acquisition geometry for dosimetry measurements

Source-Image Distance (SID)	691	mm
Detector width	300	mm
Detector height	240	mm
Beam rays angle	12.25	°
Rotation range	192.2	°
Rotation speed	6.6	°/s
Rotation time	29.1	s
N. projection	80	#
Ø FOV max	150	mm
Source-Rotation Distance (SRD)	594	mm
Magnification	1.16	x
H FOV max	206	mm

Table 3.3: Scanning parameters for the CBCT device in the 80 projections case

modified is the acquisition geometry that strongly depends on the SRD. To have a maximum diameter of 150 mm for the breast under examination, it is necessary to have an SRD of 594 mm, as reported in Table 3.3. At the same time, to stay under the 30 s rotation time limit, 80 is the maximum number of projections that can be carried out. In Table 3.3 all acquisition parameters for this latter case are shown. 80 is also an upper limit given to the number of feasible projections as it represents the buffer limit of the detector which, due to the integration and reading time, cannot exceed this value.

3.2.6 Initial setting of the Automatic Exposure Control system

The automatic exposure control (AEC) is the device designed to select all the parameters which control the detector dose, such as the anode/filter combination, kVp, and mAs, according to the effective absorption by each individual breast. The AEC aim is to keep the image quality sufficiently high for diagnostic purposes and constant as well, while delivering the appropriate dose level.

In screen-film mammography, due to the limited dynamic range of film, the AEC was designed to keep the radiation dose at the film constant. The proper functioning was verified varying the phantom thickness and checking that the mean optical density on the film was constant. In digital mammography, there is a much wider dynamic range and a completely different impact of noise on image quality. Therefore, in order to preserve the latter, the automatic exposure control should take noise into account. So, the AEC should adjust the technique factors to "compensate" the dose level at the image detector as a function of the breast absorption, to keep the image quality above a given minimum level and, in particular, the number of counts above a minimum value. Another thing to consider is that, in digital mammography, image acquisition and display are two separated processes. AEC optimization is performed on unprocessed images.

Obliviously, for reasons mentioned in the previous sections, the breast characteristic that mainly affect x-ray absorption is the thickness. Most of the systems use the compressed breast thickness measured by the height of the compression paddle to select the x-ray spectrum. In the case of CBCT, where compression is not anymore in the picture, there is the need to completely change this procedure. This is why, the majority of CBCT devices have a semi-automatic approach. The hope with IMS Giotto is to develop in the future an AEC system able to not rely just on the operator evaluation.

For now, the development of an AEC system in the prototype of the IMS Giotto still regards the initial phase. A next step, that will have to be implemented for the final definition of the CBCT AEC, is to find a way to estimate the thickness of the breast from the pre-exposure image.

For the purpose of this thesis, it is proposed to obtain an indicative number of the target counts obtainable for each single projection and to carry out a comparison with the ones actually used in FFDM and DBT modalities.

To get an idea of the average number of counts obtained on an image as the thickness varies, the AEC phantom explained in Section 3.1.2 was used. The images were taken in tomography 0° mode without compression paddle. The span considered goes from 30 to 45 kV with steps of 5 kV each for 3, 5 and 10 mAs respectively. A summary table can be found below (Table 3.15).

As the diameter, and therefore the planes of the phantom vary, a region of interest

(ROI) is defined and for each of them. From these the means and standard deviations are taken and the SNR is calculated. The ROIs used for image analysis are shown in Figure 3.14. From the acquired data, the variation of the signal and SNR

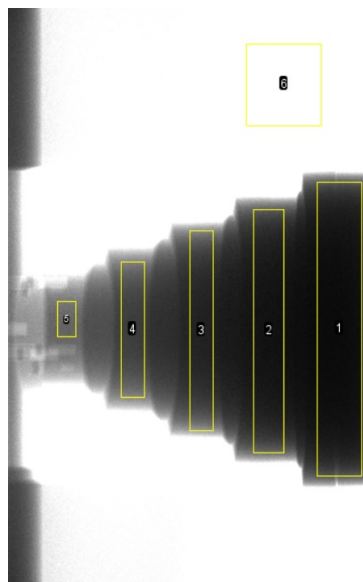


Figure 3.14: ROIs positioning for the analysis of the AEC phantom

mAs	kV
	30
3, 5, 10	35
	40
	45

Figure 3.15: Voltage and radiographic exposure at which images for AEC evaluation were acquired

with the increasing diameter is evaluated. Also the dose arriving at the detector is computed, directly from a dose meter, in all the Table 3.15 conditions. From ROI 6 also background grey level information have been obtained, from which the background saturation dose at the different voltages have been extrapolated. The idea, in a nutshell, is to relate the number of counts obtainable, by varying the diameter of the phantom, with the dose necessary to produce a signal sufficient for the image visualization. This is to be able to define the goal to aim for, while remaining within the clinically permitted dose range.

3.2.7 Image quality evaluation

Image quality can be described as a weighted combination of all the attributes that in an image are visually significant in order to assess its pleasantness for the human observer. The process of determining the level of accuracy is called Image Quality Assessment (IQA). "Quality" is a subjective notion and it is dependent on the function of the image. However, objective measures of image quality can

be defined and computed. Therefore, image quality can be tested with two main methods: subjective and objective. Subjective methods are based on the perceptual assessment of an human viewer about the attributes of an image or a set of images. These methods require a large number of people and are impossible to automate in real-time. On the other hand, objective methods are based on computational models that can predict perceptual image quality. This is why this second class of methods is preferred and the goal of image quality assessment research focuses on the design of algorithms for objective assessment that are also consistent with subjective assessment. In fact, the two methods are not necessarily consistent or accurate between each other.

Because of that, it is necessary to clarify that, in this thesis, the term image quality will indicate the so-called technical image quality (TIQ), i.e. the parameters measured from images obtained by exposing reproducible and known objects, commonly designated as test objects or phantoms. Conversely, clinical image quality (CIQ), which includes many clinical images and several radiologists in order to count for wide variability in human perception and decision criteria, will not be taken into account. Obviously, even if it is not considered in this work CIQ remains fundamental in the final image quality assessment and it will be considered in future stages of the project. If it is reasonable to assume that improvements in TIQ are likely to lead to improvements also in CIQ, it is very difficult to establish an acceptable level of diagnostic image quality based on absolute or relative thresholds for TIQ parameters.

Given the difficulty of obtaining a single and perfectly determined protocol, the guidelines to be followed for the analysis of the image and the various phantoms to be used to test it are reported in some European guidelines (see Section 3.2). The following parameters have been selected for image quality control of CBCT devices: signal-to-noise ratio (SNR), contrast-to-noise ratio (CNR), spatial resolution (MTF), homogeneity and geometrical distortion. All these parameters have been obtained starting from the reconstructed images and evaluated through the use of a customized ImageJ macro. The necessary formulas and the functioning of the macro are explained in more detail in the following sections.

All measurements acquired in this section refer to the image quality evaluation phantom (Section 3.1.2). In Figure 3.7 the layers of interest of the phantom are shown as first, second, third and fourth layers. In the following sections we will refer to the various layers according to the caption of the figure.

Prior to the explanation of the methodology for calculating the individual parameters, it must be said that all the images obtained from the reconstructions have been merged into stacks. After that, an automatic contrast enhancement is applied to the entire stack of images which is also duplicated. The duplication is done to avoid the definitive modification of the images, since filters will be subsequently

applied (in ImageJ filters permanently modify the stack). After the identification of the optimal layers for the calculation of the MTF, we proceed to the application of two filters: Unsharp Mask (radius = 4, mask = 0.8) and Median (radius = + 2 / voxel size). Unsharp masking subtracts a blurred copy of the image and re-scales the image to obtain the same contrast of large (low-frequency) structures as in the input image. This is equivalent to adding a high-pass filtered image and thus sharpens the image. "Radius" is the standard deviation of the Gaussian blur that is subtracted, while "mask" determines the strength of filtering. Instead median filtering replaces each pixel with the median value in its neighborhood (identified by the radius).

Signal-to-Noise ratio

Signal-to-Noise ratio (SNR) is a measure used to compare the level of a desired signal to the level of the background noise. It is calculated as follows:

$$SNR = \frac{Signal}{Noise} = \frac{\mu}{\sigma} \quad (3.9)$$

where μ is the mean value of a region of interest (ROI) and σ is the standard deviation in the same ROI.

The phantom layer in which these measurements are made is the third. For the evaluation of the SNR and the CNR it is necessary to obtain ROIs for each material. First the ROI of the PMMA is placed in the central position. The mean, the standard deviation and the SNR are then calculated from the single ROI according to Formula 3.9. For the positioning of the other two ROIs, starting from the coordinates of the internal square, the Makeband command is used and a band ROI with an empty section in the center is created. This allows the realization of a ROI that exactly coincides with the material. In this way both ROI for PVC and air are defined. Also for them, the same analyzes are conducted.

Below, an image taken directly from the ImageJ analysis software is shown where the ROIs of the various materials are shown on the image. The PMMA area is in red, the PVC area in blue and the air area in light blue.

Contrast-to-noise ratio

Contrast-to-noise ratio (CNR) is a measure used to evaluate contrast resolution in an image. The low-contrast resolution is the ability to distinguish between a signal and its background, when their value is pretty similar. The CNR formula is pretty similar to the SNR one but it takes into account two different portions of the image. The absolute contrast of a signal against a given background can be calculated simply subtracting the mean pixel values in each of these regions.

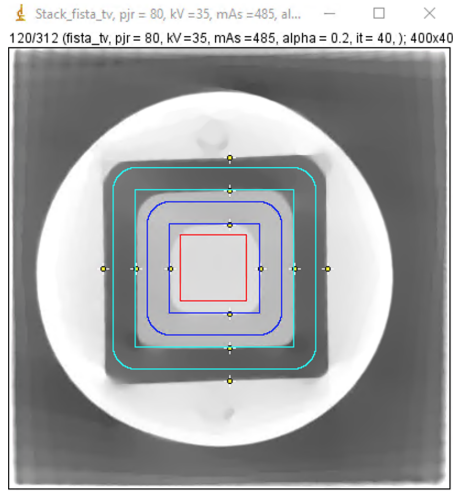


Figure 3.16: In the image the analysis ROIs of the various materials are shown. The PMMA area is in red, the PVC area in blue and the air area in light blue.

The relative contrast is this signal difference normalized to either the background signal or to the sum of the signal and the background. However, instead of this normalization, it is common, in medical imaging, to divide the absolute contrast by the background noise to obtain the CNR.

$$\frac{|\mu_A - \mu_B|}{\sigma_o} \quad (3.10)$$

Where μ_A and μ_B are the mean signal intensities in the two regions A (signal) and B (background) and σ_o is the standard deviation of the pure image noise.

CNR acquires extreme importance in a case such as that of mammography in which tumors and other pathologies are most often composed of the same organic tissue as the rest of the area which, however, has assumed malignant behavior. Therefore, malignant tissue has almost the same characteristics of the background. In particular a very similar x-ray attenuation coefficient. This is why, especially in breast radiography, where these criticality are amplified, being able to clearly define the boundaries of each structure is extremely important. So, low-contrast resolution is an essential measure.

To perform the measure, a phantom with at least two structures (one signal and one background) is needed. In fact, in the layer of interest of the phantom (always the third) we use the interfaces between the three materials to calculate the CNR. The ROIs that are used are the same as shown in Figure 3.16. After having obtained all the statistics related to the three materials, the CNR is evaluated according to formula 3.10 considering as A the region of PMMA and B the region with PVC,

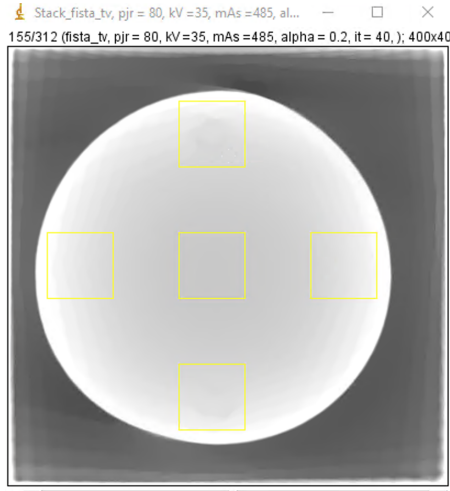


Figure 3.17: Positioning of the ROIs for the homogeneity evaluation.

while the normalization is made considering the PMMA standard deviation:

$$CNR = \frac{PMMA_{Mean} - PVC_{Mean}}{PMMA_{StandardDeviation}} \quad (3.11)$$

3.2.8 Homogeneity

Homogeneity is investigated in the fourth layer of the phantom. To assess homogeneity five regions of interest (ROIs) are placed as shown in Figure 3.17.

For each of them, the average value of the gray levels and the standard deviation are calculated in order to obtain a SNR measure. The average value of the five ROIs is then calculated together with the percentage deviation of the single ROI with respect to the average value, both for the gray levels and for the SNR. Obviously, the side of the squares and the positioning must be chosen carefully. The peripheral ROIs should be placed at sufficient distance from the phantom edge to not affect the mean pixel value, but also not too close to the central one to assess the absence of variability in all the image.

3.2.9 Modulation Transfer Function

For an accurate definition of the modulation transfer function (MTF) and its calculation method, see the Section 3.2.3. The phantom was built considering the edge as testing device for the MTF. This is both because it conforms to the IEC 62220-1-2 standard, because it is the recommended method in the EFOMP dental protocol for CBCT, and because of the conclusions drawn in Section ???. The various steps that allow the MTF calculation for the CBCT three-dimensional

technique are shown below, accompanied by images, in the order in which they are carried out on the ImageJ macro.

The first passage is the identification of the layer with the maximum standard deviation value in a region of interest (ROI) centered in the cylinder. At this point, starting from this slice, only those with a standard deviation value higher than 80 % are considered valid for the calculation of the MTF. After the identification of the optimal layers for the calculation of the MTF, an horizontal profile is taken and its derivative is calculated to find the maxima. In this way, the border points between the various materials are identified and displayed on the image. The same thing is done by taking a vertical profile. These first processes can be appreciated in Figure 3.18. After the identification of the interface points between the various materials, we proceed to the actual calculation of the MTF.

First, an edge is selected, based on the size of the reconstruction voxel, at the interface between the air and the PVC insert. From this the ESF (Edge Spread Function) is derived and, from its derivative, also the LSF (Line Spread Function). This is normalized and fitted with a gaussian fit. The MTF is then calculated according to Formula 3.2. These steps can be appreciated in Figure 3.19.

3.2.10 Geometric accuracy

This last parameter is something that needs to be checked only in the three-dimensional modality since the value of CBCT relies on its ability to produce a complete description of the anatomy of the patients. Because of that, it is essential that the relative spatial relationship of the internal structures in the image is representative of the real composition of the imaged object. Another fundamental aspect, especially in radiological applications, is that the imaging isocentre and the treatment isocentre are matched in order to ensure the correct positioning of the patient. Many factors can limit the geometrical accuracy of CBCT images: mechanical sag, flex of the CBCT arms and limitations in the reconstruction algorithms. In fact, a CBCT reconstruction algorithm needs as input the relative positions (x, y, z) between the source, the volume to be reconstructed and the detector, in order to project the data correctly. So, there is the need for a dedicated geometric calibration in order to obtain images not strongly compromised by artifacts and distortions.

In CBCT geometric accuracy is checked using the second layer of the image quality phantom. In reality, the analysis proposed in this thesis will be more qualitative than quantitative. As, for the phase in which the project currently is, any geometric distortions would only testify to the incorrect description of the initial scan geometry.

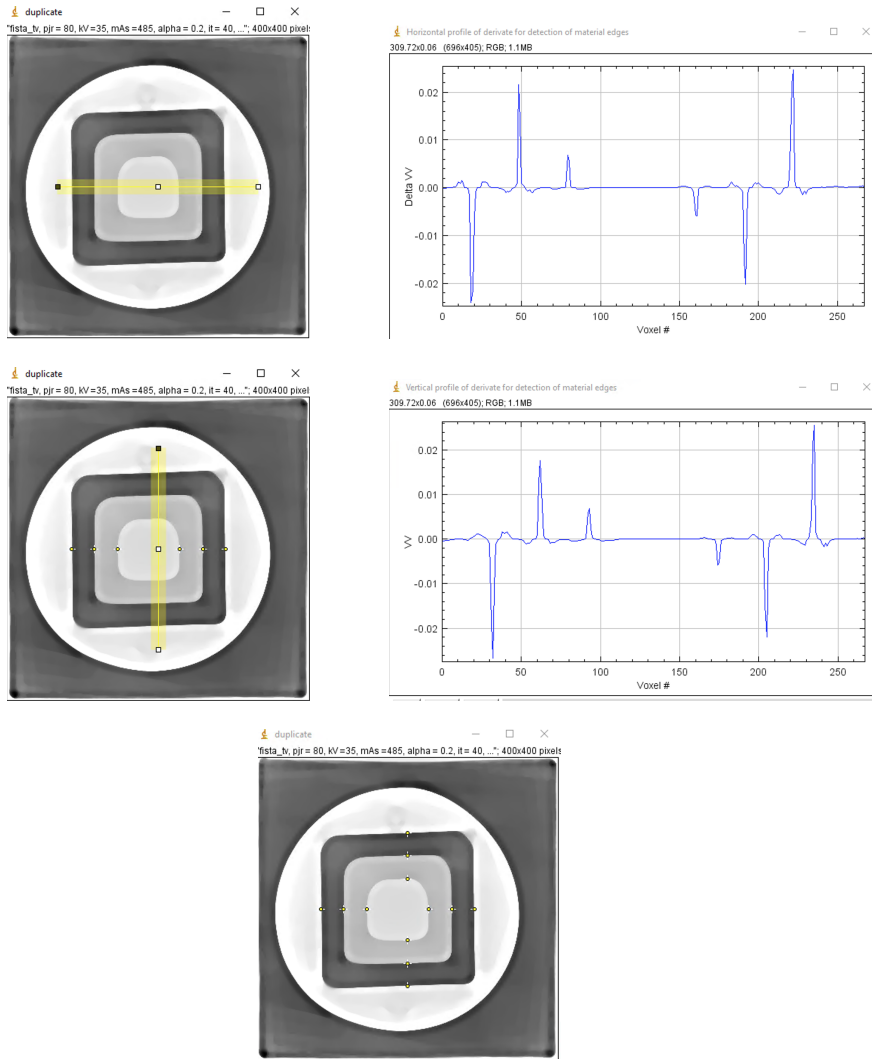
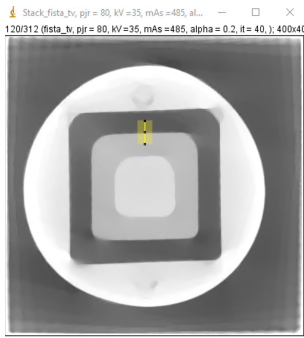
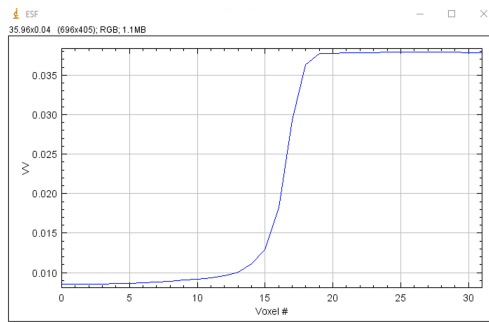


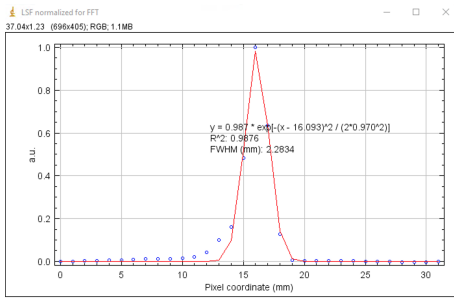
Figure 3.18: Process of identification of the interface points between the various materials in the phantom.



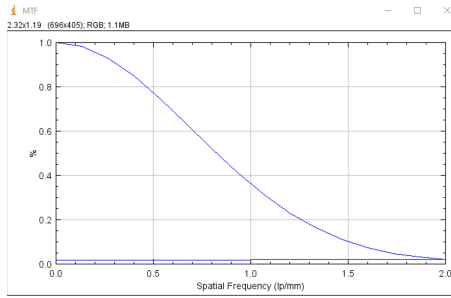
(a) Selection of the edge



(b) Edge Spread Function



(c) Line Spread Function with the application of a gaussian fit



(d) Modulation Transfer Function

Figure 3.19: Steps for the calculation of the MTF from the reconstructed images.

Chapter 4

Results

The results of the analyzes reported in the previous chapter, Section 3.2, are reported below. The order in which they are presented and the section titles coincide for ease of reading.

4.1 Characterization of the high voltage generator

Eight exposures were made for each kV value (from 19 to 49 kVp) using the W/Ag target/filter combination and at least 30 mAs.

The kVp value measured with the nominal kVp value set on each measurements are compared in Figure 4.1. In the image the eight exposures are in different colors. To determine the kVp reproducibility, the average and the average standard deviation of the kVp values are calculated together with the variation coefficient.

This same test was performed for all control parameters (kV, mA, filament current and exposure time) obtained from the measurements with the oscilloscope. Results are shown in Figures 4.2 and 4.3.

According to the EUREF standard the deviation from the mean value should stay under $\pm 5\%$ with an achievable limit of $\pm 2\%$. As already mentioned, the average percentage variability of the control parameters is measured precisely through the Coefficient of Variation (CV) defined as:

$$CV = \frac{s}{m} \quad (4.1)$$

where s and m are the standard deviation and the average of the samples. Results obtained for each kV value (from 19 to 49 kVp) explored are reported in Appendix. The maximum recorded value and the mean value of the variation coefficients are, instead, reported in Table 4.1.

The CV is always around 0.2% and never above 0.5%, the maximum recorded

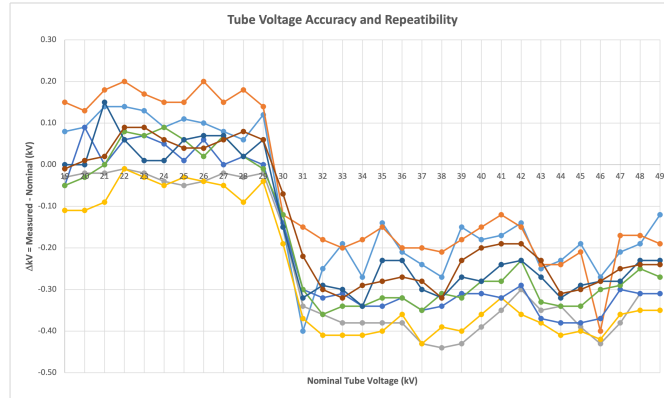


Figure 4.1: Graph of the accuracy and repeatability of the tube voltage. On the y axis is the distance between the nominal value and the measured value of the tube, while on the x the nominal value of the selected kV.

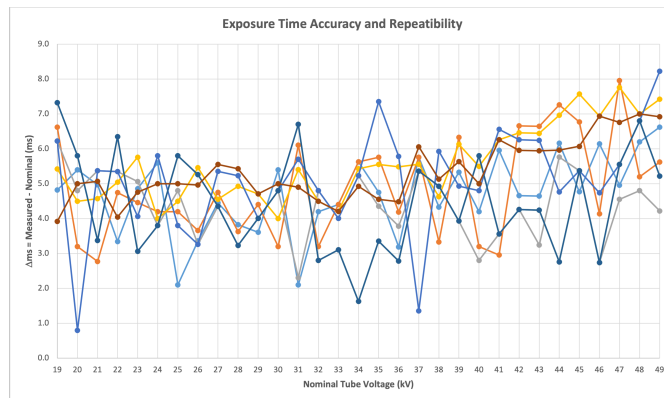


Figure 4.2: Graph of the accuracy and repeatability of the exposure time. On the y axis is the distance between the nominal value and the measured value of the exposure time, while on the x the nominal value of the selected kV.

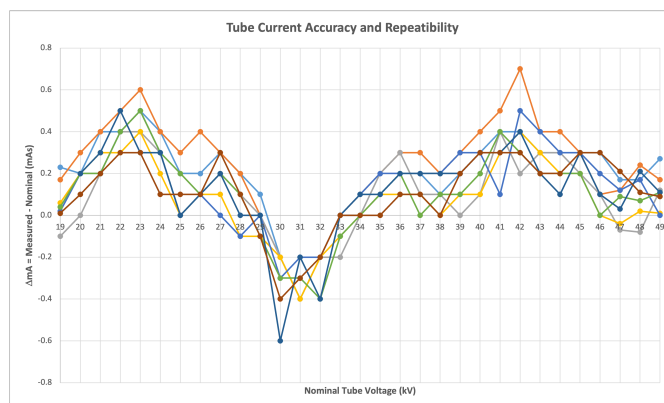


Figure 4.3: Graph of the accuracy and repeatability of the tube current. On the y axis is the distance between the nominal value and the measured value of the current, while on the x the nominal value of the selected kV.

CV					
kVp	kV_{mean}	mA_{mean}	$A_{filament}$	ms	
0.5%	0.5%	0.1%	0.2%	0.5%	Maximum recorded value
0.2%	0.2%	0.1%	0.1%	0.2%	Mean value

Table 4.1: Maximum recorded value and mean value for the variation coefficients (CV) for all the control parameters (kV, mA, filament current and exposure time).

value, defined as $\frac{Max-Min}{m}$, in the whole range of available kV, so the standards requirements are met.

4.2 Spectra simulation

As described in Section 3.2.2 a set of simulations were carried out in order to characterize the tube and the spectrum of the device. The inspected range goes from 35 to 49 kV with a 1 kV step. Results are shown in Figure 4.4.

From these simulated spectra, the average energies and the Half Value Layers (HVL) were then obtained directly from the output file generated by the Speckpy Python toolkit. These were then plotted against the kV value of each simulation. Results are shown in Figure 4.5 and in Figure 4.6.

In the graphs, the HVL values extrapolated from the simulated data are compared with the ones directly read on the dose meter for the three types of dose meters.

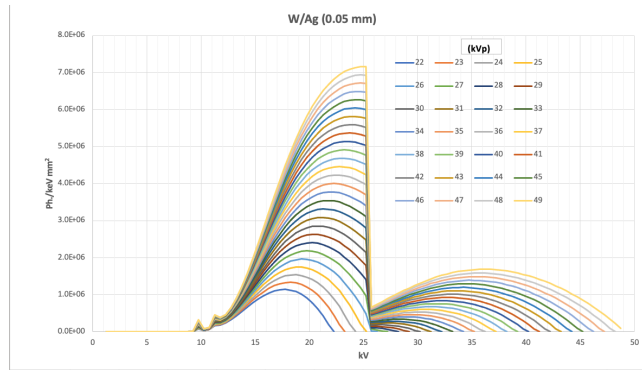


Figure 4.4: Spectra obtained from the Speckpy simulations.

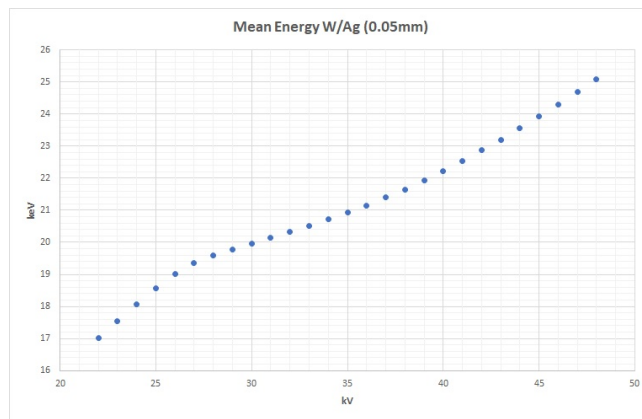


Figure 4.5: Mean energy values obtained from the Speckpy simulations plotted against the kV value of each simulation.

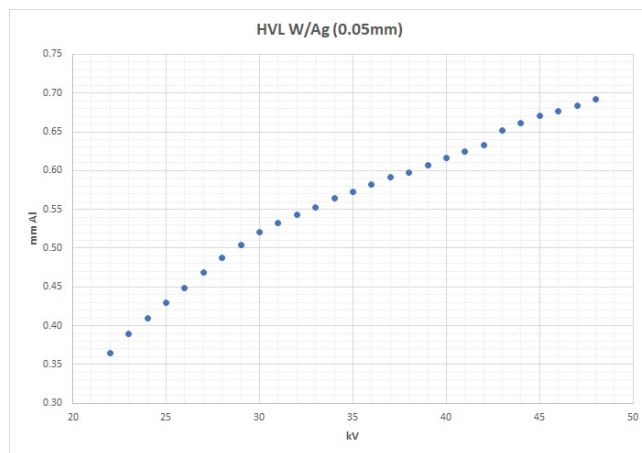


Figure 4.6: HVL values obtained from the Speckpy simulations plotted against the kV value of each simulation.

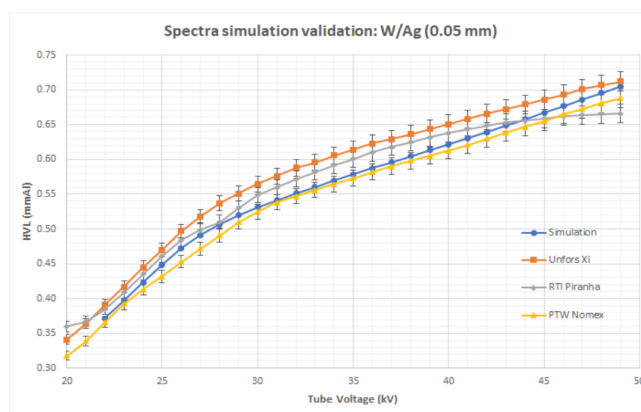


Figure 4.7: Validation of the HVL simulated data with respect to those read from three different dose meters.

The results of the validation for the W/Ag anode/filter combination are shown in Figure 4.7. As can be seen, the values of all three dose meters are totally comparable with the values obtained through simulations. For reasons of space, Table 4.2 shows only the central values of the curves in Figure 4.7. This has the purpose of making the HVL values reported by the simulations and by the dosimeters also qualitatively comparable.

From the table, it is clear that the distance between the simulated data and those

kV	Simulation	Unfors Xi	RTI Piranha	PTW Nomex
	mmAl			
28	0.51	0.54	0.51	0.49
29	0.52	0.55	0.52	0.52
30	0.53	0.56	0.55	0.53
31	0.54	0.57	0.56	0.54
32	0.55	0.58	0.57	0.55
33	0.56	0.59	0.58	0.56
34	0.57	0.6	0.59	0.56
35	0.58	0.61	0.6	0.57

Table 4.2: Central values of the inspected range for the simulations validation with the dose meters.

obtained by the dose meters is always below 0.05 mmAl and, therefore, we can conclude that the data are comparable and, thus, validate the simulations obtained with the python toolkit. Moreover, it is possible to conclude that the PTW Nomex

dose meter returns the closest values to those of Spekpy simulations. Therefore, from now on, this will be the dose meter that will be used in this thesis work.

4.3 Detector

Based on the methodologies explained in detail in Section 3.2, the results of the detector characterization are presented below in the order with which they were previously presented.

The data will be reported for both detectors considered in the study: the Screen-Plus (direct conversion) and the Varex (indirect conversion) at the end of this section a comparison between the two will follow in order to accurately justify the choice of the detector that was decided to mount on the prototype.

4.3.1 Response function

The response function can be evaluated by plotting the mean pixel values against the entrance surface air kerma as explained in Section 3.2.3. The linearity is determined by the evaluation of the best fit through all measured points and the calculation of the square of the correlation coefficient (R^2). Results for the various response function, calculated according to Table 3.2, in both FFDM and DBT modalities are shown in Figure 4.8.

For the FFDM modality the data of the four images taken at the same mAs value were averaged and reported. Instead, for the DBT modality, a more precise measurement was preferred. In fact, tomography is a less stable technique than mammography and averaging eleven images would have been way less precise. The dose for each single projection and the single mean and standard deviation value obtained from the standard ROI were therefore taken into account. For this reason, in the DBT graph (in Figure 4.8) we find many more clustered points in the selected mAs values.

We can however conclude, observing the graphs in Figure 4.8, that the linear trend of the response function is confirmed for both modalities and for every value in the kV range. According to the EUREF standard, the linearity is confirmed only for $R^2 > 0.99$. The fit parameters (in the $y = ax + b$ form) together with the R^2 values obtained for both the acquisition modalities are reported in Tables 4.3 (for Varex) and 4.4 (for ScreenPlus). As you can see, the linearity can be confirmed in both cases and for both modalities.

Below, the response functions of the two detectors (Varex and ScreenPus) are plotted in the energy range from 24 to 34 kV, for both FFDM and DBT modalities (Figures 4.8, 4.9).

In Figure 4.10 it is possible to witness how the gain of the detector, defined as

kV	FFDM			DBT		
	a	b	R^2	a	b	R^2
24	17.5	-22.2	0.99	40.4	13.8	0.99
26	20.7	-40.2	0.99	51.8	9.2	0.99
28	22.4	-35.9	0.99	58.4	33.6	0.99
30	23.5	-35.9	0.99	62.5	38.1	0.99
32	24.6	-38.3	0.99	65.7	93.9	0.99
34	25.8	-22.6	0.99	70.4	104.4	0.99

Table 4.3: Fit parameters and square of the correlation coefficient for both FFDM and DBT acquisition modalities. For the Varex detector.

kV	FFDM			DBT		
	a	b	R^2	a	b	R^2
24	3.8	0.5	0.99	17.7	14.4	0.99
26	4.6	1.5	0.99	21.6	28.4	0.99
28	5	4.9	0.99	23.8	41.9	0.99
30	5.3	7.5	0.99	25.2	59.3	0.99
32	5.6	12.2	0.99	26.6	80.2	0.99
34	5.9	16.3	0.99	28.4	11.6	0.99

Table 4.4: Fit parameters and square of the correlation coefficient for both FFDM and DBT acquisition modalities. For the ScreenPlus detector.

the signal produced per unit of dose arrived to the detector, increases in both modalities by increasing the energy and how this increase appears greater for the high gain operating mode (DBT modality). However, this effect seems to concern the indirect conversion detector more strongly. The interpretation that can be made is that, by increasing the beam energy, the number of visible light photons produced in the scintillator increases. This means that the number of photons that directly reach the detector reading layer (amorphous silicon TFT layer) is greater. Therefore, the gain tends to increase.

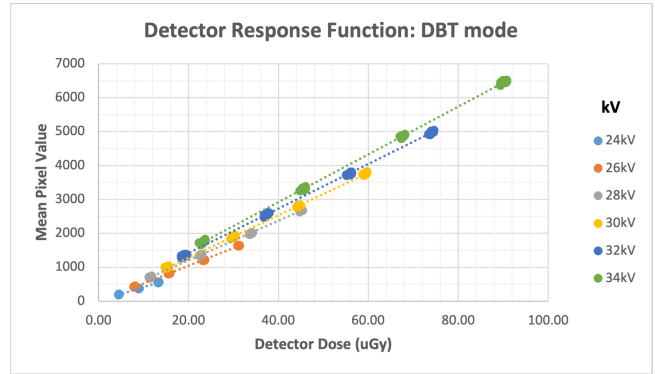
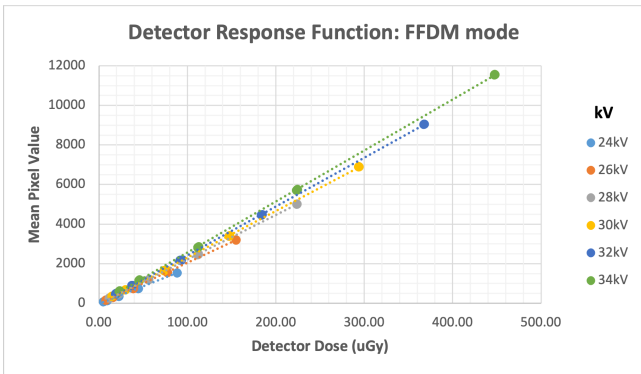


Figure 4.8: Varex detector response function in both DBT and FFDM modalities.

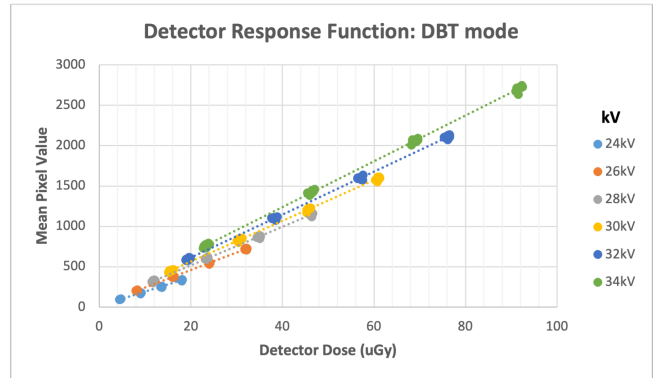
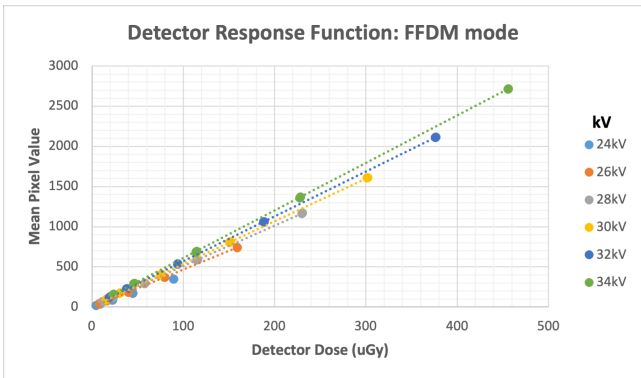
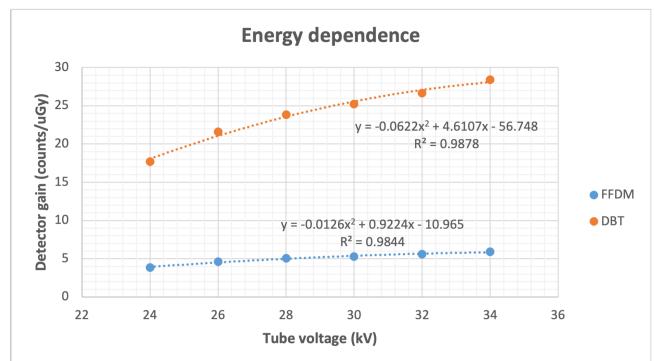
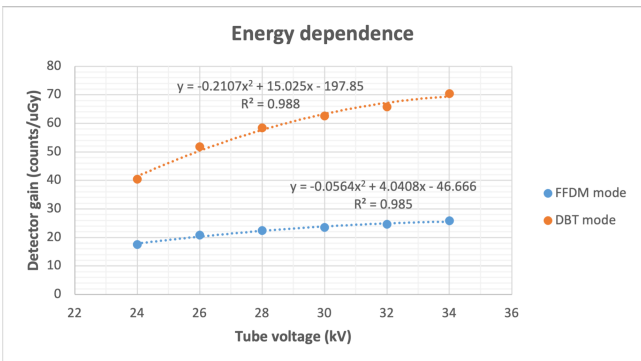


Figure 4.9: ScreenPlus detector response function in both DBT and FFDM modalities.



(a) Varex detector

(b) ScreenPlus detector

Figure 4.10: Detector gain for both Varex and ScreenPlus.

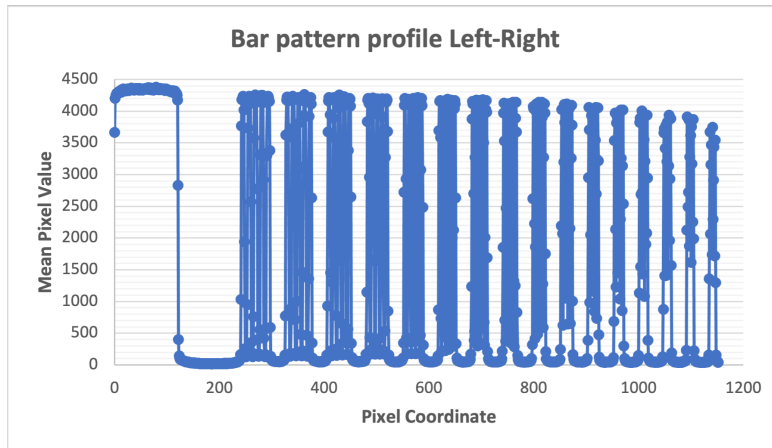


Figure 4.11: Left to right profile acquired from the bar-pattern.

4.3.2 Modulation Transfer Function

Below are all the analyzes on the various MTF measurement methods that have been introduced in Section 3.2.3. We remember that the acquisition setup has been considered the same for all the methods and according to the IEC 62220-1-2:2007 standard. A 2 mm Al foil was put between the tube and the detector and the grid was removed. The objective was to investigate all the possible influences deriving from the acquisition method on the results of the final MTF curve. From this analysis then, choose the best method for the evaluation of the MTF both in the case of the 2D characterization of both available detectors, and for the evaluation of the image quality in 3D.

Bar pattern

Four images of the phantom, in four distinct positions were taken in order to investigate the dependence of the final MTF curve on the initial positioning. The profile obtained from a bar-pattern phantom is illustrated in Figure 4.11. The first modulation corresponds to the distance between black and white and subsequently, going forward with the pairs of lines per millimeter, the distance between the peaks becomes shorter, demonstrating the difficulty of distinguishing between the two gray values. The MTF can be directly obtained from this profile by considering the distance between the peaks for each frequency and normalizing it with respect to the distance between black and white.

In Figure 4.12 the results for the four positioning are reported.

The bar pattern method is certainly highly variable on high frequencies because to determine the profile on high frequencies, where there are aliasing effects determined by the fact that we have a fixed sampling frequency due to the pixel size,

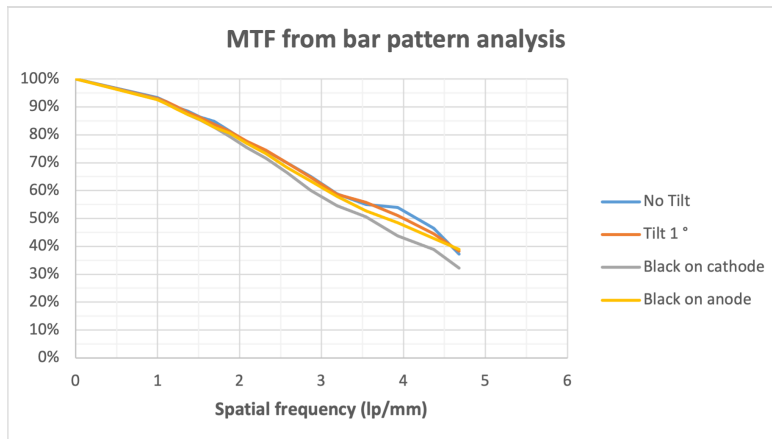


Figure 4.12: Dependence of the MTF from initial positioning of the bar-pattern obtained at 26 kV and 60 mAs.

brings some complications. This is precisely why this method, historically used in analog systems, has been completely abandoned in digital.

Apart from the bar-pattern phantom, for all the other method the oversampled procedure to produce the Linear Spread Function (LSF) used for the Fast Fourier Transform (FFT) calculation has been applied. Details on the procedure are described in Section 3.2.3 a Gaussian fit may or may not be applied to the LSF. The effect of its application is to make the data more linear and less related to the noisy oscillations that are present on the sides of the peak. For a stable and repeatable results of the LSF estimation in this thesis work the choice of using a Gaussian fit, applied at the raw data, was made. This Gaussian fit is essential for smoothing the noise at the tail of the distribution to smooth the final MTF curve. This clarification appears fundamental if it is underlined that the protocol specifies the data acquisition method and the few basic steps for obtaining the MTF. A certain profile is acquired, a derivative is made to obtain the LSF, the Fourier transform is applied for the final result. Every other data treatment is left to the user. This is why is really important to define the data treatment and analysis methodology. The different software available and ready for the analysis of the MTF, can produce different results because they can apply different data treatments with other types of fit that can alter the final result. Therefore, it is good to specify when describing a measurement protocol the exact steps taken during data processing.

Figure 4.13 shows the application of the Gaussian fit to the LSF for the three methods. While, in Figure 4.14, the effect of its application on the final MTFs. From the figures it is evident that the application of this Gaussian fit has different

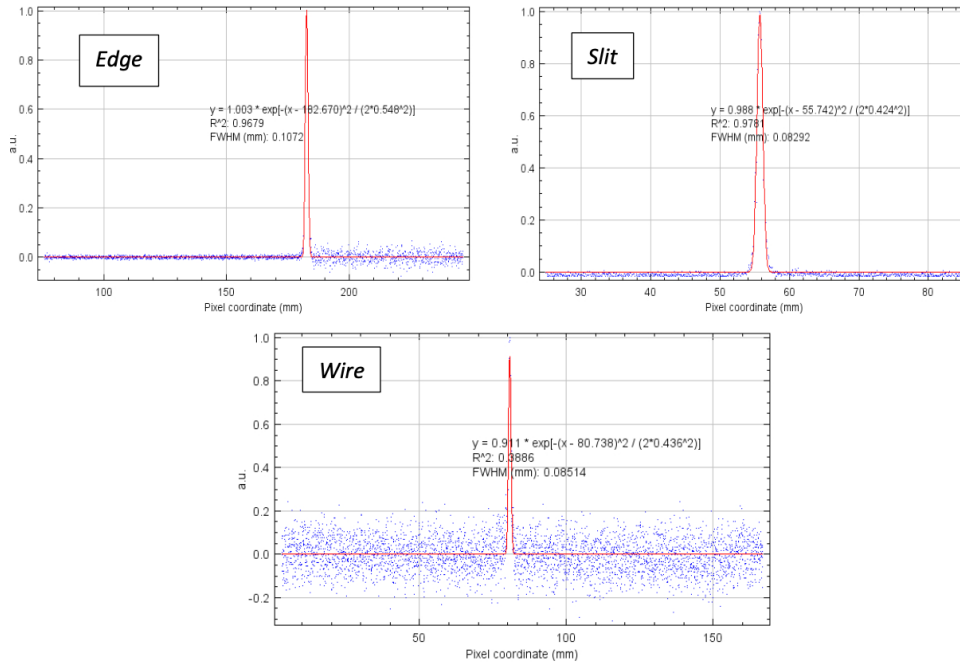


Figure 4.13: From the left to the right: LSF obtained from the derivate of the ESF; LSF obtained directly from the Slit- camera signal; LSF obtained from the tungsten wire profile.

degrees of impact based on the phantom selected for the measurement. For the slit camera the Gaussian fit has much lower impact due to the collimation of the LSF tails directly from the data acquisition. We can observe that the wire method is less stable as it strongly depends on the Gaussian fit conditions. Given the great noise on the tails, it would not be possible to get a meaningful MTF without doing a Gaussian fit.

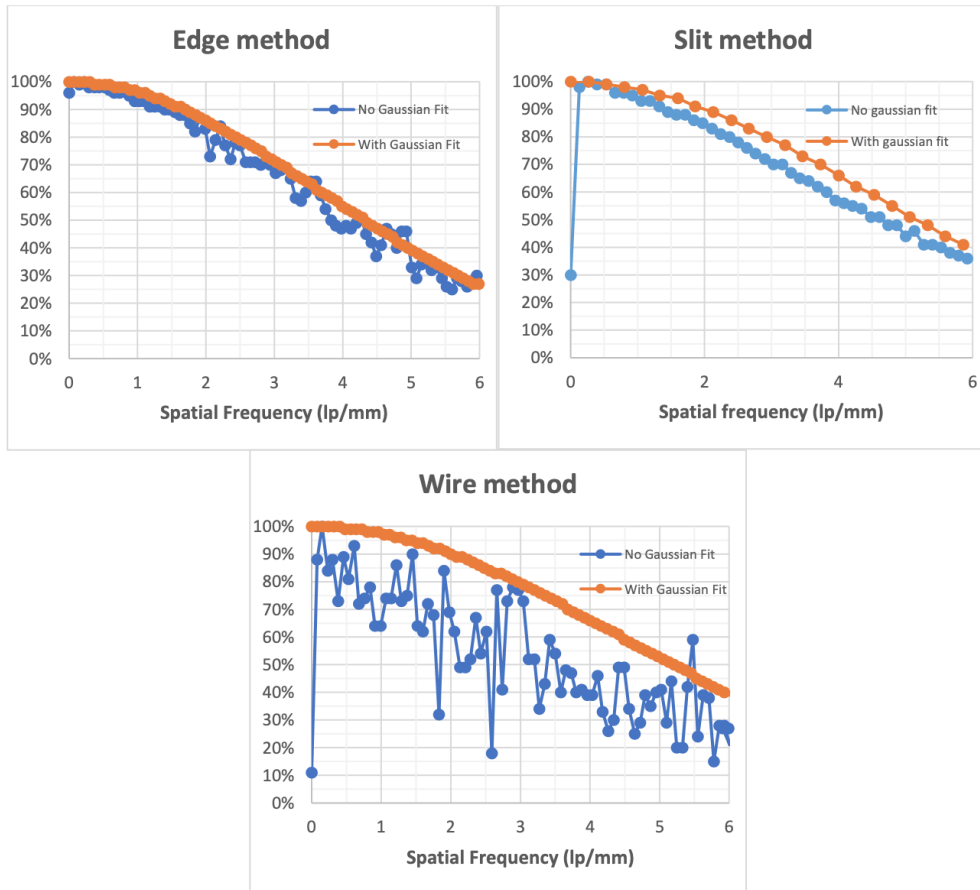


Figure 4.14: Effect of the gaussian fit applied to the LSF on the final MTF for the three phantoms.

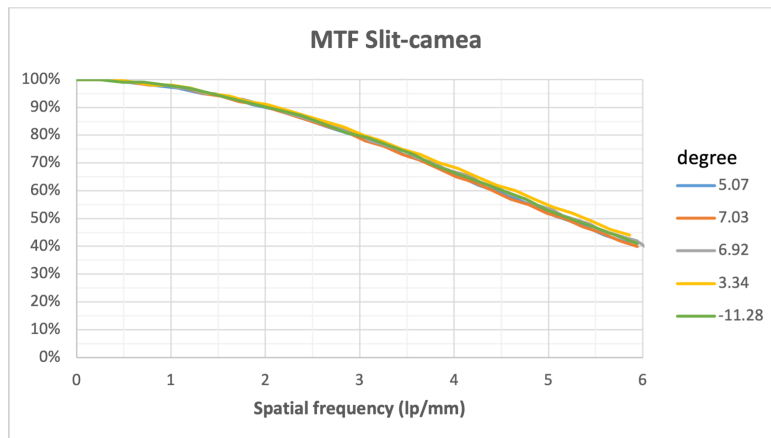


Figure 4.15: Dependence of the MTF from initial positioning of the slit camera obtained at 26 kV and 60 mAs.

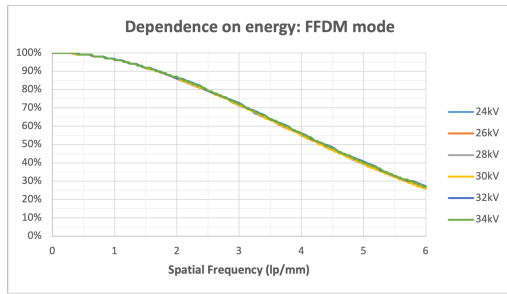
Slit camera

In Figure 4.15 the dependence of the MTF from the positioning (distance from the focal spot projection) of the test device is shown. The slit camera method appears to be very dependent on the position of the device with respect to the geometric projection of the focal spot and, therefore, introduces practical measurement difficulties, especially in the clinical field where it is necessary first to identify the focal spot projection on the detector in order to have a correct positioning. The measurement only makes sense at that precise point and, for that, is not easily repeatable. So, the use of this method requires very precise fabrication and alignment of the device in the radiation beam, and also an high radiation exposure to allow sufficient transmission through the narrow slit.

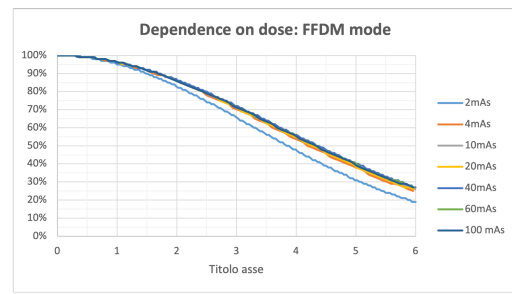
Edge

The measurement of MTF through the use of the edge test device was first introduced by Samei in 1997. The article introduced the possibility to determine the MTF with the measurements of the Edge Spread Function (ESF) using an opaque object with a straight edge and nowadays, this is the method indicated in the IEC 62220-1-2:2007 standard.

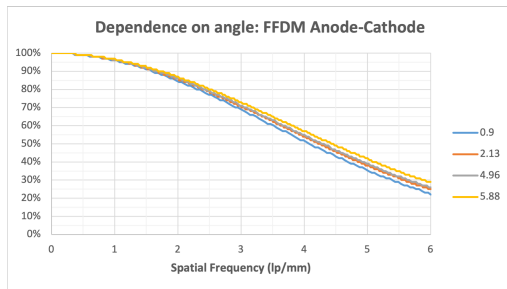
The measurement of MTF from this phantom was investigated in its dependencies on dose (mAs) and voltage (kV). The dose dependence is investigated by acquiring uniformly exposed images under the same conditions expressed in Table 3.2. The voltage dependence is, instead, investigated by acquiring images at the fixed value of 60 mAs for all the voltages reported in the table. The dependence on the initial positioning of the phantom was also investigated. The angle of inclination of the phantom was evaluated both in the anode-cathode and in the left-right directions.



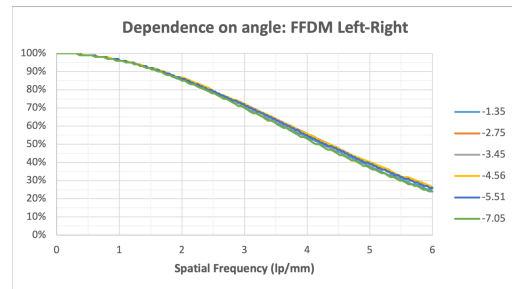
(a) *Dependency on the energy for the MTF obtained with the edge phantom*



(b) *Dependency on the dose for the MTF obtained with the edge phantom*



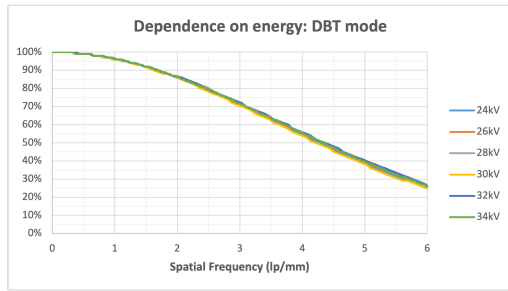
(c) *Dependency on the angle in the Anode-Cathode direction for the MTF obtained with the edge phantom obtained at 26 kV and 60 mAs*



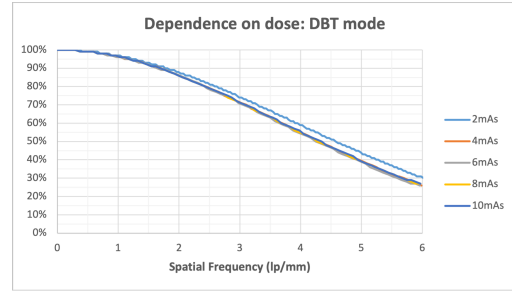
(d) *Dependency on the angle in the Left-Right direction for the MTF obtained with the edge phantom obtained at 26 kV and 60 mAs*

Figure 4.16: The graphs show the dependency on voltage, dose and position for the MTF obtained with the edge phantom.

Results of the obtained MTF curves and relative dependencies are shown in Figure 4.16. Then, we evaluated the impact of the same exposure parameters, however, using the detector in high gain mode, which is used for DBT modality. This was done to investigate the dependence of MTF on the acquisition mode as well. In Figure 4.17 we can appreciate these results. From the graphs we can conclude that the measures of the MTF is independent from the energy. In fact, for each kV value, there is no appreciable spread between the curves in every spatial frequency at which the MTF is computed. Also for the dose the spread between the curves is minimal (even below 3%) at every mAs value except for the 2 mAs curve that appears much lower. This is certainly due to the need to send a minimum quantity of dose to allow the image to be displayed. With a low dose, such as that sent at 2 mAs, the signal is too weak to distinguish objects effectively and, therefore, the evaluation of the spatial resolution of the system appears lower. So we explain this value by arguing that the high noise certainly influenced the result of the



(a) *Dependency on the energy for the MTF obtained with the edge phantom*



(b) *Dependency on the dose for the MTF obtained with the edge phantom*

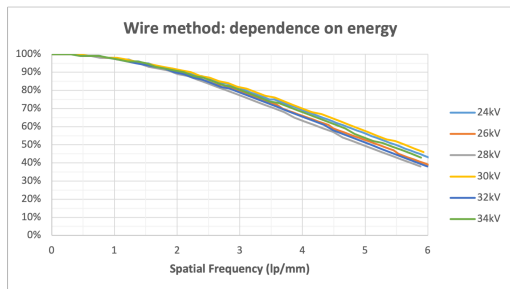
Figure 4.17: The graphs show the dependency on voltage and dose for the MTF obtained with the edge phantom in DBT modality.

Gaussian fit. Also for the DBT modality, the spread between the curves can be considered negligible both for the energy dependency and for the dose dependency, because it is in each case below 5%. As regards the position, we can conclude that the variation evaluated at the point corresponding to 5 lp/mm for the left-right direction can be again neglected as it is below 5%. In the cathode-anode direction the variation is slightly greater than in the previous case as what becomes heavier is the position of the edge with respect to the maximum intensity of the x-rays, therefore with respect to the geometric projection of the focal spot. It is however still negligible as it is below 10%.

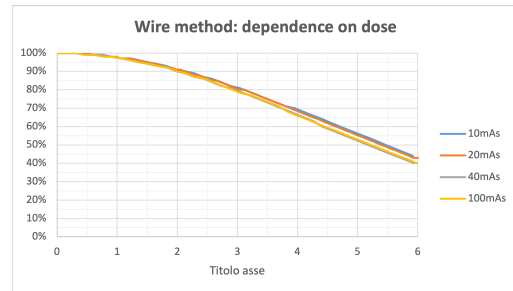
Also the gain mode does not change the spatial resolution characteristics which are an intrinsic characteristic of the detector that depends on the pixel size and the type of conversion.

Wire

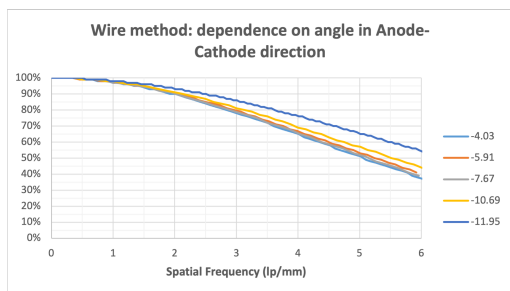
Also for this phantom, dependencies on dose (mAs) and voltage (kV) were investigated acquiring images in the same conditions and same parameters used for the edge phantom. The dependence on the initial positioning of the phantom was also investigated. Both from the distance from the focal spot and from the angle of inclination of the phantom. Results of the obtained MTF curves and relative dependencies are shown in Figure 4.18. From the graphs, we can conclude that the measures of the MTF is independent from the energy. In fact, the greater spread between the curves, evaluated at 5 lp/mm is below 10% can be considered negligible. The same reasoning can be applied to the dose dependence of MTF. In this case the dependence, always evaluated at 5 lp/mm, is even below 5%. As regards the position, on the contrary, we can conclude that the variation evaluated at the point corresponding to 5 lp/mm is much more significant, in fact it even



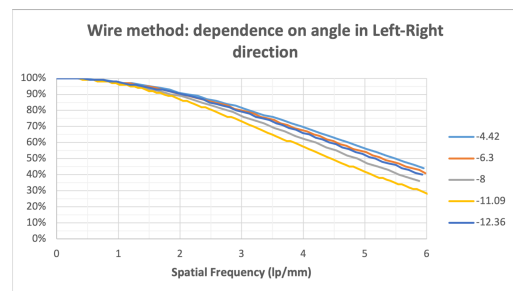
(a) *Dependency on the energy for the MTF obtained with the wire phantom*



(b) *Dependency on the dose for the MTF obtained with the wire phantom*



(c) *Dependency on the angle in the Anode-Cathode direction for the MTF obtained with the wire phantom obtained at 26 kV and 60 mAs*



(d) *Dependency on the angle in the Left-Right direction for the MTF obtained with the wire phantom obtained at 26 kV and 60 mAs*

Figure 4.18: The graphs show the dependency on voltage, dose and position for the MTF obtained with the wire phantom.

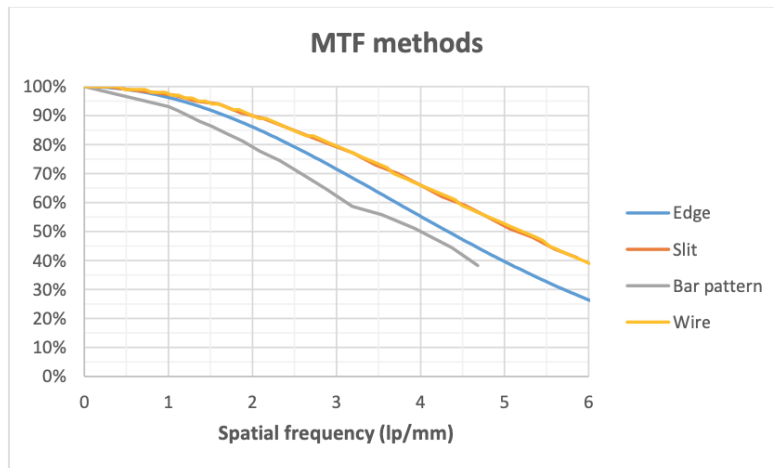


Figure 4.19: Comparison of the different methods for MTF measurement obtained at 26 kV and 60 mAs.

reaches 20% in both the anode-cathode and in the left-right directions, especially when this exceeds 8° . According to the IEC 62220-1-2:2007, the angle that must be considered for the evaluation of the MTF must be between 3° and 5° . This indication must be respected to obtain valid results since, as can be deduced, the measurement strongly depends on the angle of inclination of the test object.

A graph for the direct comparison of all the MTF evaluation methods is reported in Figure 4.19. All curves shown in this graph were calculated under the same measurement conditions. From this it is possible to sum up the main characteristics for each one. The MTF obtained from the bar pattern evaluation results underestimated with respect to the other methods, especially in the high frequency range. The slit camera and the tungsten wire are overestimated with respect to the edge method. The difference, evaluated at 5 lp/mm, between the methods is around 10%. This is mainly due to the data treatment (gaussian fit of the LSF tails) and also to the possible presence of a penumbra created by the edge testing device thickness. Moreover, the position relative to the geometrical projection of the focal spot on the image plane also plays a part.

Net of the evaluation of the different methods and possible phantoms for calculating the MTF, it is chosen which one to use for the design of the phantom for image quality evaluation in the 3D. The edge test device with the oversampling calculation method proposed by Samei is selected for this calculus because of its robustness, its lower sensitivity to angular positioning. In fact, although this method underestimates the MTF compared to others proposed, it was chosen to

design the phantom described in Section 3.1.2. The design presents the edge as interface between PVC and air. This is because aluminum, although it absorbs x-rays better without letting the signal pass under the object, in 3D creates metallic artifacts that distort the image and disturb its visualization. Instead PMMA, of which the body of the phantom is composed, avoids this problem, however, making the signal less clear and subject to penumbra effects. The specific choice of PVC and air materials, on the other hand, is dictated by adherence to the EUREF protocol for dental CBCT, currently the only one existing for CBCT, which describes the positioning and acquisition methods. The tungsten wire was not selected for the phantom design for two main reasons: as with aluminum, tungsten also creates disturbing metallic artifacts for the image; moreover, in 3D it is impossible to control the angle of inclination of the wire. This last reason, as we have seen above and can be seen in Figure 4.18, has a noticeable effect on the final result of the MTF. Therefore, the method cannot be considered as robust in this specific case. However, in the future it could still be interesting to evaluate a phantom with tungsten wire which, although more sensitive to the measurement conditions, adds visual information on the detectability of an object whose physical characteristics are known.

Spatial resolution in CBCT is essentially affected by three scan parameters:

- Field of view. Every CBCT system has a limited number of available field of views, and each one is associated with a voxel dimension and a spatial resolution;
- Number of projection views. Different spatial resolutions could also be selected for different numbers of projection views, obtained for example by partial or full rotation scan or by different rotation times;
- Reconstruction algorithm. The choice of the convolution kernel for back projection methods, or the kind of iterative approach, affect the final spatial resolution and noise of the obtained image.

Another characteristic that is important to underline is that spatial resolution is not stationary inside a CBCT volume, as a consequence of the acquisition process and 3D back projection. MTF values at periphery of the volume could, in fact, differ from that in the centre by about 20-30%.

For the 2D characterization, the MTF obtained with the edge phantom for both the indirect conversion detector (Varex) and the direct conversion detector (Screen-Plus) is reported in Figure 4.20. In the graph also the nominal MTF declared by the detector manufacturer is reported in red and is used to validate the measurements acquired. Evaluating the quality of an MTF curve is a very broad and tortuous speech. In fact, the protocols do not indicate a method for evaluating

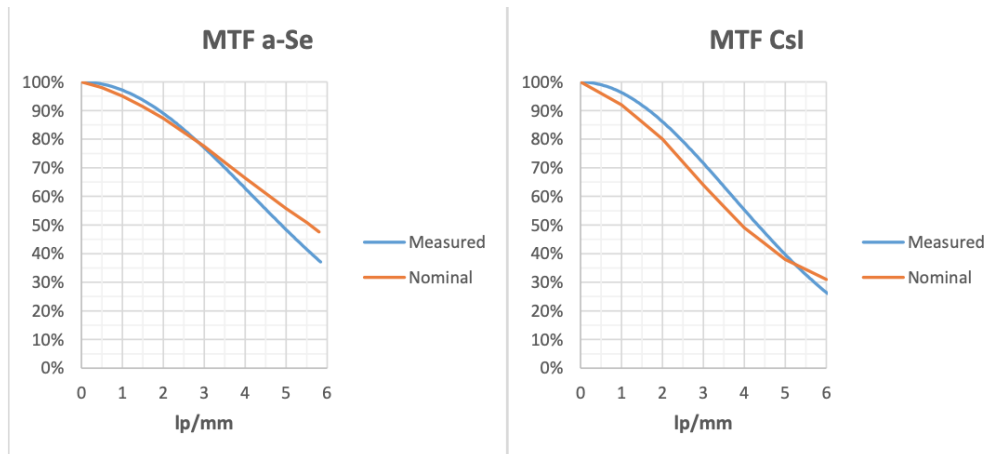


Figure 4.20: MTF for the Varex (CsI) and ScreenPlus (a-Se) detector. Evaluated with the edge test device and compared to the nominal manufacturer MTF obtained at 28 kV.

the quality of the MTF of your detector. Only a range of variation is indicated in which to periodically check that the current MTF is, compared to that measured at the time of installation of the device. Therefore, the only way to compare the MTF obtained and to certify its quality is to compare it with the MTF declared by the manufacturer. Even in this case, however, it must be emphasized that the measures cannot be considered superimposable. In fact, there are many differences behind the simple measurement of the MTF of a detector. First we must consider the possible differences in the chosen test object. As has been seen, changing the test phantom greatly affects the final measurement, but even for the same category, different test devices may have slightly different characteristics. Much more significant is the choice of the methodology with which the calculation of the MTF is carried out. This in fact, unlike the test object, is not regulated by the protocols and therefore the methodology with which to obtain the final measurement can be freely chosen even without being specified. A final difference that deserves to be mentioned is the one in the measurement acquisition configuration. The machine on which the manufacturer carried out the test has a Mo/Mo combination and a corresponding spectrum for 28 kV with 2 mm of Al. Our setup, we remember instead, is W/Ag with 30 kV and 2 mm of Al. Therefore, for the evaluation of the similarity between these curves, the point relative to the lp/mm is taken and the percentage variation between the curves is evaluated. The curve is considered comparable if the variation is below 10-15%. Given that the variation between the two curves shown in Figure 4.20 is below 5% for both cases, the two curves can easily be said to be comparable.

4.3.3 Noise Power Spectrum

We remember that the acquisition configuration is composed according to the IEC 62220-1-2:2007 standard. So, with the addition of a 2 mm of Al foil at the exit of the tube and without the addition of the anti-scatter grid in order to reduce the structured noise. To establish the degree of dependence of the NPS on the variation of the spectrum, measurements were made as the voltage and mAs vary (Table 3.2). Again, as described in the Section 3.2.3, four images for each combination were acquired in the FFDM modality, while for the DBT the angle was kept fixed at 0° in order to already have eleven images.

The individual NPS curves calculated in the range of kV from 24 to 34, according to Table 3.2, are shown in the Appendix.

Below the value of the NPS, for the different kV values considered, is plotted against the increasing dose at fixed spatial frequency (Figure 4.21).

From Figure 4.21 it is possible to witness that, once the value is normalized and the trend of the NPS on the dose is analyzed at a fixed spatial frequency, there is no particular dependence on energy. We can also conclude that the noise is quite flat given that, at the three different frequencies, there is not much variation between the curves, especially in the FFDM modality. At high frequencies, the noise appears slightly lower than the values at low frequencies. This can be due to inhomogeneities in the aluminum foil. Since the latter is not perfect and very close to the source, these slight inhomogeneities are perfectly compensated for the calibration dose, moving from the calibration zone, the inhomogeneities of the filter become more significant on the final NPS especially at low frequencies. This means that the NPS becomes more colorful (less composed of only white noise) and that, as the frequencies increase, the noise spectrum tends to decrease. This effect appears much more evident in the Varex detector than in the ScreenPlus due to the indirect conversion nature of the first. The conversion process from x-rays to visible light that happens in the scintillator, adds a certain auto-filtration effect on the output signal due to light diffusion in the media. A comparison between the NNPS of the two detectors, for both acquisition modalities, is shown in Figure 4.23. We can conclude that for the indirect conversion detector the noise is more colorful and drops more at high frequencies, compared to the noise of the direct conversion detector which is more flat.

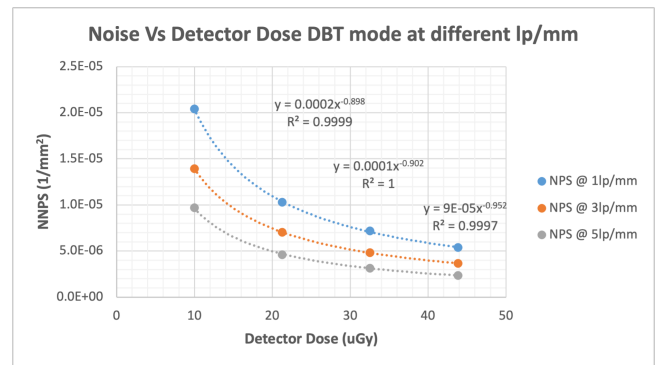
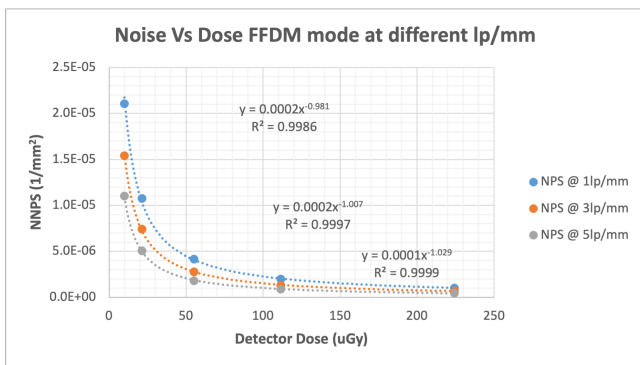
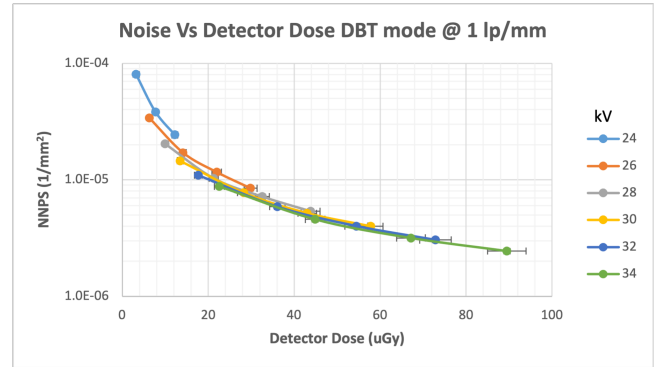
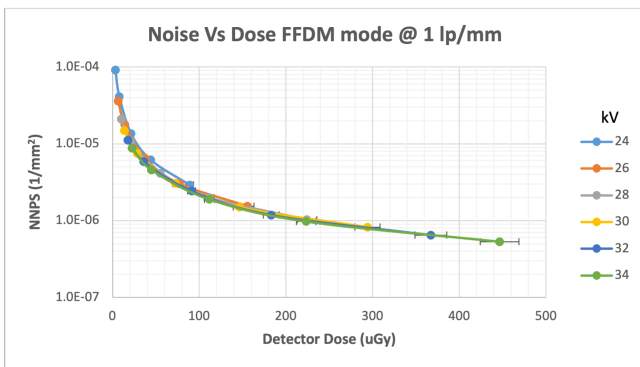


Figure 4.21: In the graphs NPS values, for the different kV considered, are plotted against the increasing dose at fixed spatial frequency for both modalities. Also at a fixed energy, the trend for different spatial frequencies is shown for both modalities. For the Varex detector.

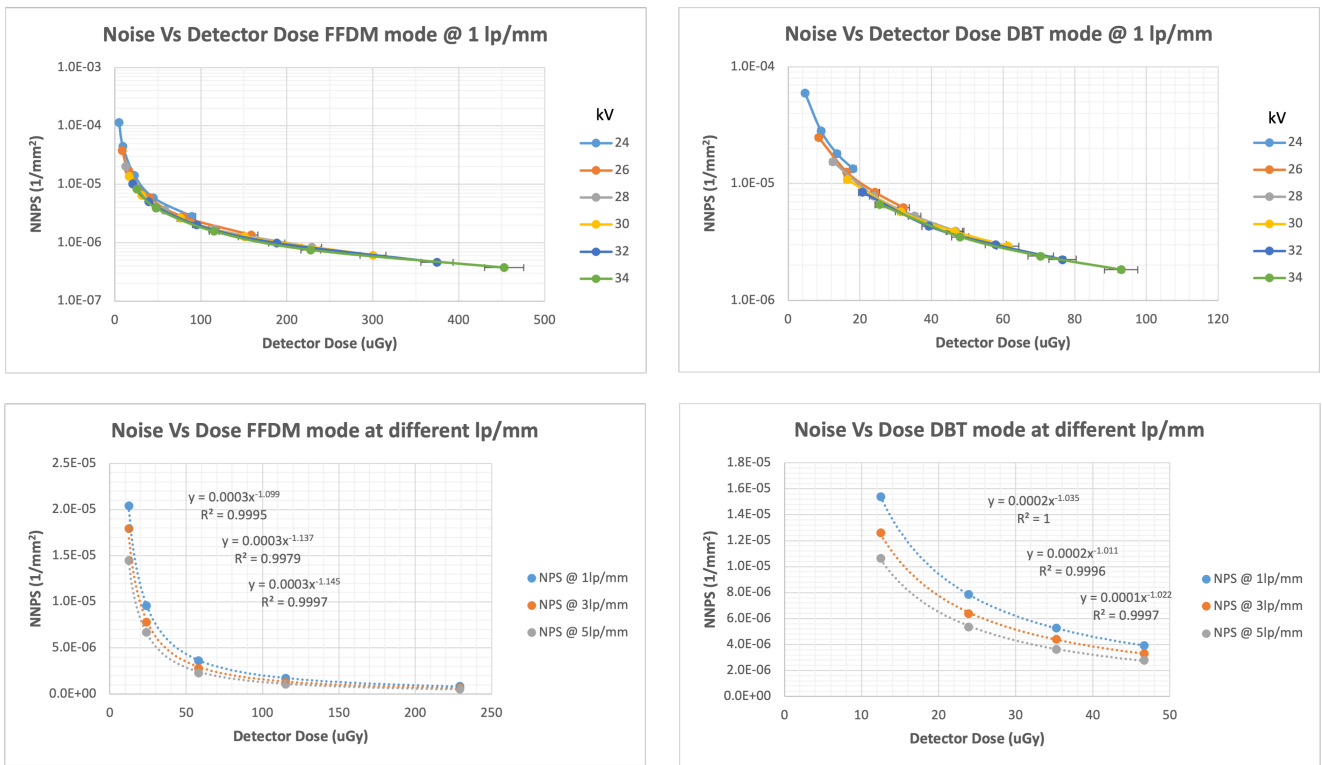


Figure 4.22: In the graphs NPS values, for the different kV considered, are plotted against the increasing dose at fixed spatial frequency for both modalities. Also at a fixed energy, the trend for different spatial frequencies is shown for both modalities. For the ScreenPlus detector.

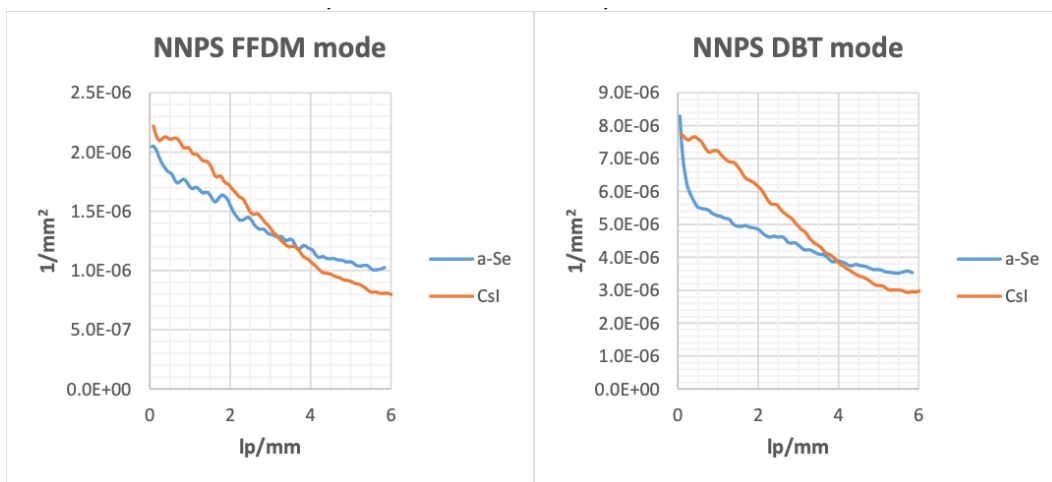


Figure 4.23: NNPS for the Varex (CsI) and ScreenPlus (a-Se) detector obtained at 28 kV.

4.3.4 Detective Quantum Efficiency

After the evaluation of the NPS and MTF, DQE is derived. As previously explained in Section 3.2.3, simulations, in the same acquisition configuration used for the images taken for MTF and NPS, were made in order to calculate the SNR_{in}^2 factors, necessary to perform the DQE calculation. Data obtained are reported in Table 4.5. DQE was calculated for both modalities (FFDM and DBT) and

	Fluence	Air kerma	Mean energy	HVL	SNR_{in}^2
kV	photons/cm ²	μGy	keV	mmAl	
24	1.4E+06	2.3	20.3	0.72	5914
26	2.6E+06	3.9	21.5	0.82	6597
28	3.9E+06	5.6	22.1	0.88	6950
30	5.2E+06	7.2	22.4	0.91	7199
32	6.5E+06	8.7	22.9	0.95	7462
34	8.1E+06	10.4	23.5	0.99	7775

Table 4.5: Values obtained from the Speckpy simulations.

for both the detectors. Results of the single DQE curves obtained for each kV in the 24-34 range, according to Table 3.2, are shown in the Appendix. Below, the value of the DQE, for the different kV values considered, is plotted against the increasing dose at fixed spatial frequency (Figures 4.24,4.25). What is highlighted is therefore the quantum limited range, the range within which the DQE remains constant. In both figures a plateau region can be identified. There, the contribution of quantum noise with respect to electronic noise is compensated, below this region, electronic noise has much more weight than quantum noise and has damaging effect on the image. In both detectors we notice that the DQE collapses at low doses. This behavior is much more impactful for the direct conversion detector (ScreenPlus) than for the indirect conversion one (Varex). This collapse occurs at low doses when significantly deviating from the calibration dose (100 μGy). The latter is fixed and is defined as the incident reference dose on the detector for a standard breast in mammography. In the CBCT case, there is still no precise idea what the size of an uncompressed standard breast can be considered, therefore, the calibration dose that needs to be considered remains the same.

The choice of analyzing a low range of doses and a high range of kV wants to simulate what will be more or less the range of action of the CBCT prototype. In fact, there will be very short pulses (which implies a very low dose per single image and a fairly high noise). So the intention was to explore if, at doses like 10 or 50 μGy, which are more or less the expected doses, the DQE of the dedicated mammography detector (which both are) could give good results.

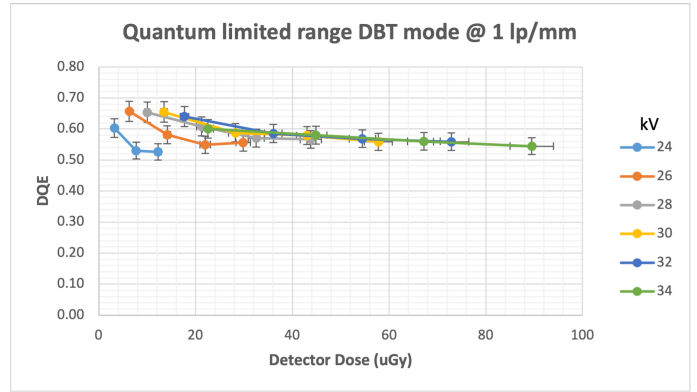
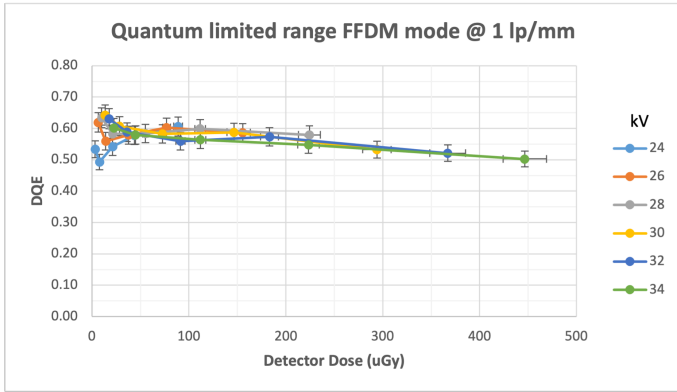


Figure 4.24: DQE calculated both in FFDM and DBT modalities for the Varex detector.

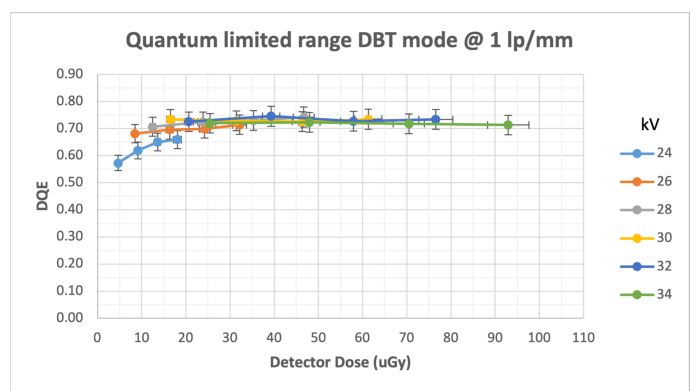
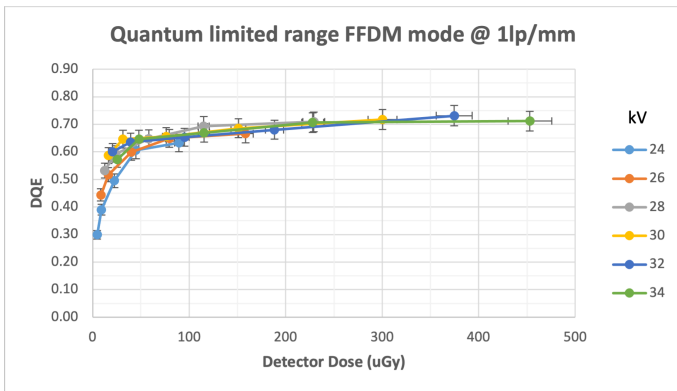


Figure 4.25: DQE calculated both in FFDM and DBT modalities for the ScreenPlus detector.

What we get is that, especially in FFDM mode, at low doses the ScreenPlus detector tends to significantly lower the performance and this is shown by Figure 4.25 where the DQE passes from a plateau of 70% to 30,40%. On the other hand, the Varex detector DQE values appear almost flat, on the contrary they seem to decrease as the dose increases. This counterintuitive behavior can be justified considering that, at low doses there is a higher gain, so maybe the SNR_{in}^2 value, deriving from the simulations, could be underestimated. In this case the photon influx would be higher than the one considered and so DQE appears to be slightly lower. Despite that, focusing at low doses, the DQE is much more stable for the Varex detector and never drops below 50%. In the DBT (high gain) mode, on the other hand, the calibration of the detector and therefore the flat field correction seems to have a greater impact on the final evaluation of the DQE which, however, always shows better results than the ScreenPlus detector.

In the graphs in Figures 4.24 and 4.25, error bars of 5% are shown on both axes. The error on the DQE (Formula 3.4) is the combination of the errors in the measured Modulation Transfer Function (MTF), Normalized Noise Power Spectrum (NNPS) and incident dose at detector level. The source of error in the evaluation of the NNPS is represented in the positioning of the ROIs used for the 2D FFT calculation, and special attention must be made for area presenting local inhomogeneities to avoid high values in the low frequency range (< 1 lp/mm). To obtain a sufficient number of frequency point (128) a ROI dimension of 256 x 256 pixel is suggested to identify eventual structured noise (for example the presence and visibility of the anti-scatter grid for flat-field images obtained in clinical FFDM mode). To smooth the curves of the average noise power spectrum calculated a large number of images is required (4 to 12 per dose point), and the IEC standard suggest to present the result in a binning form, applying by fact an average between different frequency points but the same effect cab be obtained applying a moving average or a median filter with 3 a kernel of points among the NPS values at different frequencies, maintain the possibility to identify noise issues using the Fourier analysis, crucial for x-ray device manufacturer for medical applications and their system diagnosis for production and maintenance purposes. In this study the NNPS curves have been obtained using 4 images per dose point and for each energy spectrum a new calibration is performed to avoid known drift of homogeneity of the image due to the dependence of the flat-field correction process (especially dark frame correction) on the calibration conditions. No smoothing of the NPS curves has been applied. The error in dose and HVL measurements declared by the manufacturer of the x-ray digital multi-meter is 5% for both, so the normalization obtained at different energy spectra and dose levels introduces an error of the same amount and must be considered a contribution in the final DQE value. The SNR_{in}^2 used to normalize the measurements is not measurable in normal clinical

environment but only in special condition using a spectrometer and special geometry. For this reason, the applicable standard provides a table with reference values to be used for different reference spectra. The beam quality W/Ag (0.05 mm) used in normal clinical condition is not present in the IEC 62220-1-2:2007 standard so, as suggested by Annex C of this standard, a software for the simulation of the x-ray beam must be used for the calculation of the normalization factor SNR_{in}^2 . This is the biggest source of error in the DQE evaluation because different spectra simulation software generates different photon fluence and a consequently different value of SNR_{in}^2 . Considering 5% of error from the Dose measurements, and 5% of error in the HVL used to scale the SNR_{in}^2 for direct measurement, the DQE curves should be showed with a minimum percentage error of $\pm 10\%$. Considering the error bars, we see that the differences, especially in the case of the Varex detection, are not significant. In particular in high doses, all the values are completely within the range of experimental uncertainties.

The special conditions of the DQE measurements (no carbon fiber for breast support present, absence of anti-scatter grid, 2 mm Al filter as absorbing object placed close to the tube output for scattering reduction etc.) makes this method good for comparison of the technical characteristics for x-ray digital image receptor but not considerable for extrapolation of clinical performances of the final mammograph system. Especially for detectability of small objects like micro-calcifications, that are detected in the high frequency range, where the errors in the DQE evaluation are higher reducing the sensitivity of the method itself, and where the final clinical image quality is affected by other more significant source of variability (AEC system, local densities and large dynamic range of breast tissues x-ray contrast). Comparing the two detectors, we can conclude that MTF in direct conversion is 10% better at 5 lp/mm. As we can see from the NPS graphs (Figure 4.23), for the indirect conversion detector the noise is more colorful and drops more at high frequencies, compared to the noise of the direct conversion detector which is more flat. If we compare the DQE curves (Figure 4.26), that of the direct conversion detector is about 10% better than the indirect conversion one.

For the comparison of the DQE curves with respect to those declared by the manufacturer (Figure 4.27), the same argument made for the MTF can be applied here. Differences in data processing are unpredictable and significant. In the calculation of the DQE there are also the uncertainties as to which method was used to calculate the SNR value. Furthermore, it is not negligible to consider the electronic environment used to test the detector. The machine electronics introduces an electronic noise level which can also be very different depending on the measurement setup. A mammography system has motors, filters, and power supplies that can introduce a lot of noise. While the probable different spectrum as seen does not

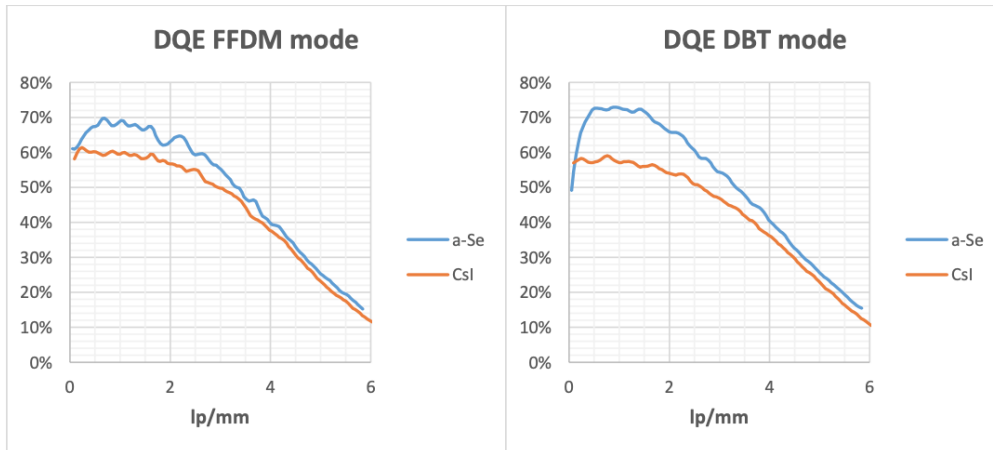


Figure 4.26: DQE for the Varex (CsI) and ScreenPlus (a-Se) detector obtained at 28 kV.

have a great influence on the final result. At the end of all these considerations it is concluded that the most suitable detector for the project is the indirect conversion one (Varex) as it is faster, much less sensitive to electronic noise at very low doses (both in FFDM and in DBT modalities) and it is cheaper.

4.4 Dosimetry

In order to estimate the incident dose at the patient's breast different dosimetric measures have been performed. These measures are performed in a setup (described in Section 3.2.5) that aims to replicate the exam conditions.

4.4.1 Tube output

Tube output is a measure necessary for the calculation of incident air kerma (K_i) when tube loading (mAs) and compressed breast thickness are known. In the CBCT case however the measure is made without the compression paddle in the configuration. In Figure 4.28 results for the tube output measurements are shown. In the graph a distance of 670 mm from the x-ray tube focus is considered. On the x axis the voltage range (19-49 kV) used in clinic can be found. For each of these values, the reported dose value was read directly on the dosimeter. As expected, the trend is quadratic as the correlation coefficient ($R^2 = 0.99$) testifies. In fact, due to the divergence of the radiation, the power of the dose per unit of surface area decreases inversely proportional to the square of the distance as the distance from the radioactive source increases. In general, it is desirable to have a high

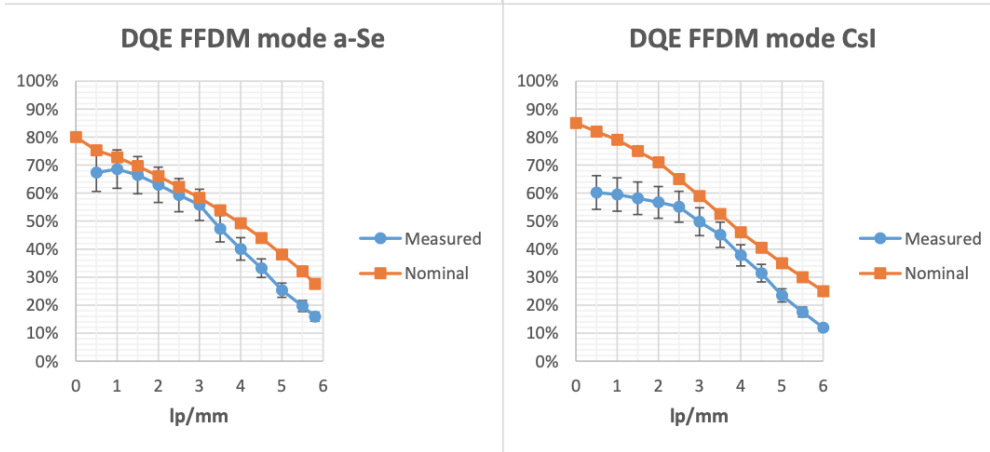


Figure 4.27: DQE for the Varex (CsI) and ScreenPlus (a-Se) detector compared to the nominal manufacturer DQE obtained at 28 kV.

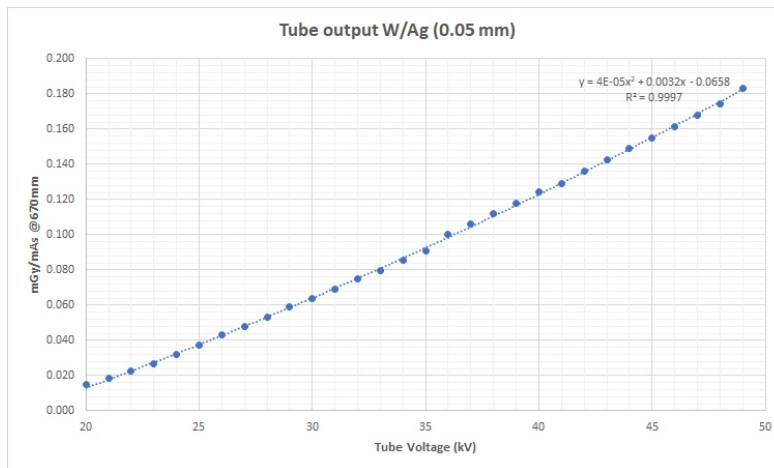


Figure 4.28: Tube output calculated at 670 mm from the x-ray tube focus

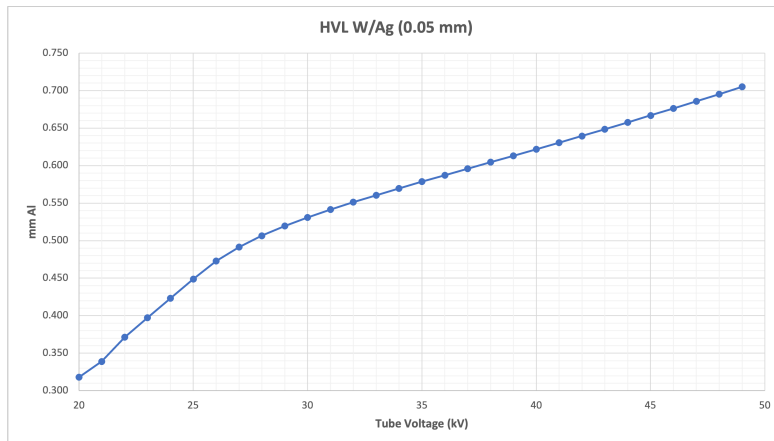


Figure 4.29: HVL values calculated in millimeters of aluminum (mmAl) with respect to the tube voltage applied

output for various reasons. It results in shorter exposure time, minimising the effects of patient movement and ensures an adequate penetration of large or dense breast. On the other hand, a very low tube output can result in a long exposure time, with significant risk of motion artifacts.

4.4.2 Half value layer

Results for the half value layer measurements, directly read on the dose meter, are reported in Figure 4.29. By definition, the HVL values should increase with the tube voltage, for each given anode/filter combination. This trend is confirmed in the graph.

4.5 Initial setting of the Automatic Exposure Control

The objective of this section is to evaluate the number of counts obtainable as the diameter of the phantom varies and to relate it to the dose necessary to produce a signal sufficient for the image visualization. These analyzes will be used to define a range of acquisition parameters to vary, remaining within the permitted clinical dose range, in which to evaluate the quality of the reconstructed image.

The calculations necessary for the initial setup of an AEC system start from the evaluation of the images obtained from the AEC phantom described in Section 3.1.2. First we evaluate the trend of the counts (average gray level) with respect to the dose incident to the detector (670 mm distance) for all the diameters considered

by the layers of the phantom (Figure 4.30). The images were taken in tomography 0° mode without compression paddle. The span considered goes from 30 to 45 kV with steps of 5 kV each for 3, 5 and 10 mAs respectively. As the thickness, and therefore the planes of the phantom vary, a region of interest (ROI) is defined and for each of them. From these the means and standard deviations are taken and the SNR is calculated. As you can see, the detector response remains linear even when the voltage and diameters values vary. This is not to be taken for granted as, as these same parameters vary, the spectrum arriving at the detector (at a distance of 670 mm) changes. However, in the selected energy range the linearity can be considered valid as the DQE of the detector does not drop drastically.

After that, the signal and the SNR obtained in the different kV-mAs combinations are evaluated. Results are shown in Figure 4.31 and 4.32. The trend of the signal is also as expected. As we can see, it grows as the dose increases and decreases as the diameter increases. The SNR, on the other hand, depends strictly on the diameter considered rather than on the dose. The latter in fact seems to play a small difference and only for small diameters, while, at large diameters, the curves are completely overlapping. To get an idea of the expected counts that allow a good visualization on the final image, Table 4.6 shows the AEC table counts for this same detector in FFDM and DBT mode. The values in this table are already used in clinic and therefore are shown for comparison.

In both columns the number of target counts for a given thickness of compressed breast is reported. Both refer to the high gain detector mode, which is currently used to do the tomosynthesis. As you can see, the average counts in the single image for both modes are more or less around 1000-2000 counts on average. This value, as can be seen in Figure 4.31, is always reached only for 45 kV. For all other voltages, the drop in dose leads to a drastic drop in the average number of counts as well, bringing them even below 200 for 30 kV.

Never as in this section is it necessary to remember that the CBCT machine that IMS Giotto intends to create is not a dedicated machine, but a machine capable of carrying out all the examinations possible up to now and, in addition, the CBCT. This is why these results are not too surprising. They only highlight the fact that we are working in sub-optimal conditions and with a detector that could improve both in terms of gain and in reading speed.

From the analysis of the background, on the other hand, the trend of the counts is obtained as a function of the dose at the detector and, from the slope and the intercept of the latter, the saturation dose is obtained for each voltage. Results are shown in Figure 4.33 and 4.34. The saturation dose is used to normalize the image. Going beyond that dose level runs the risk of burning the skin and losing signal in areas that are between tissue and non-tissue.

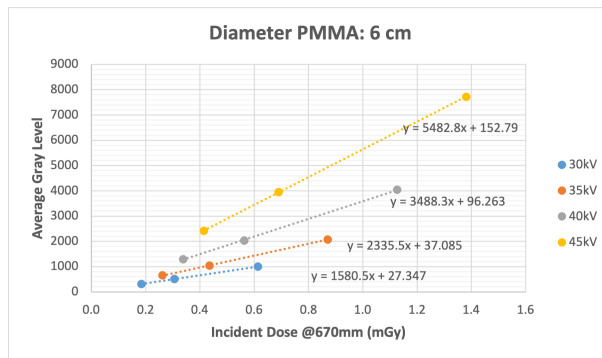
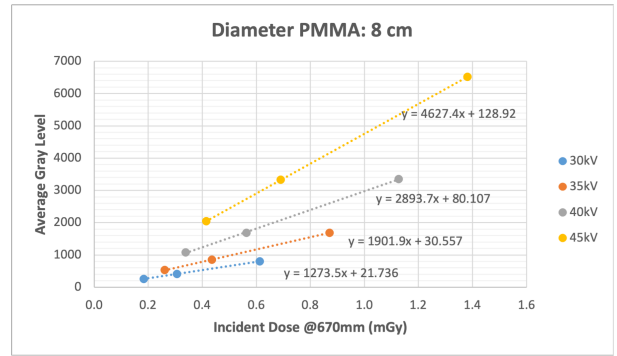
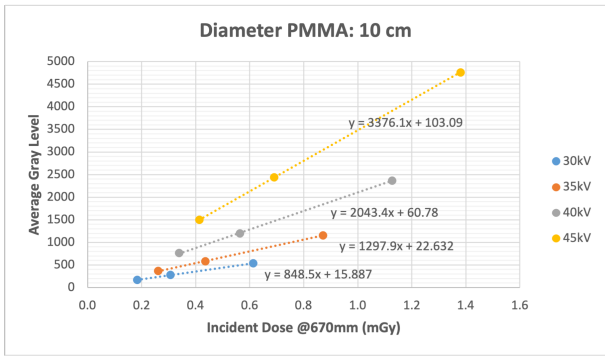
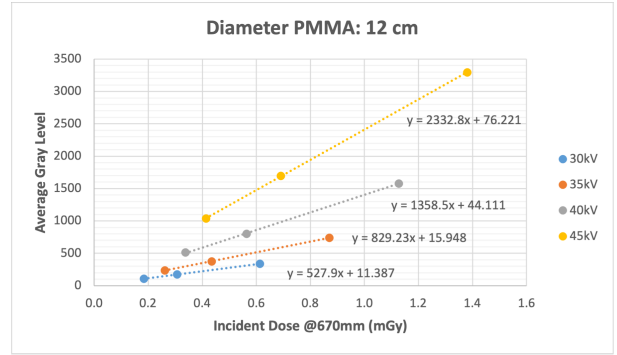
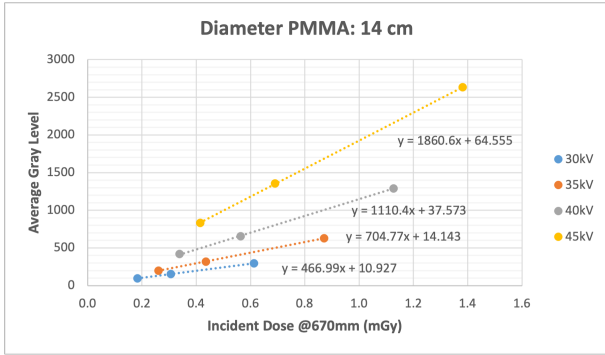


Figure 4.30: The graph shows the trend of the average number of counts and the dose incident at the detector as the voltage considered increases and for the different diameters of the AEC phantom

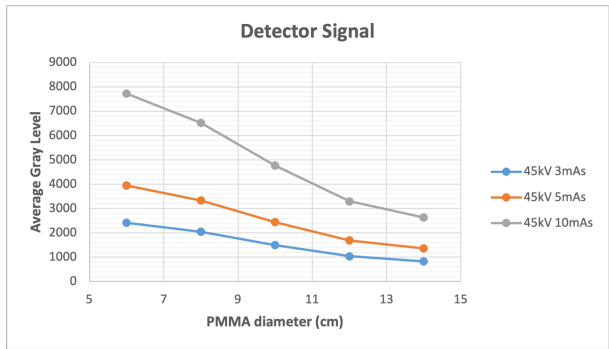
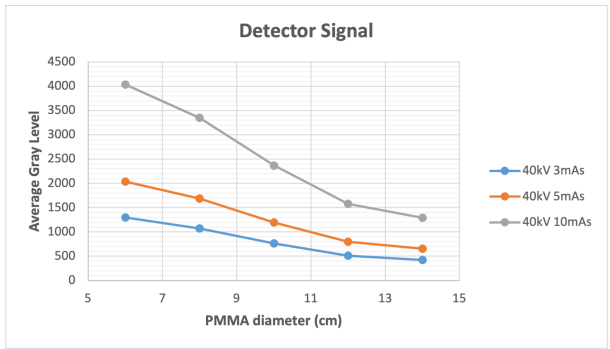
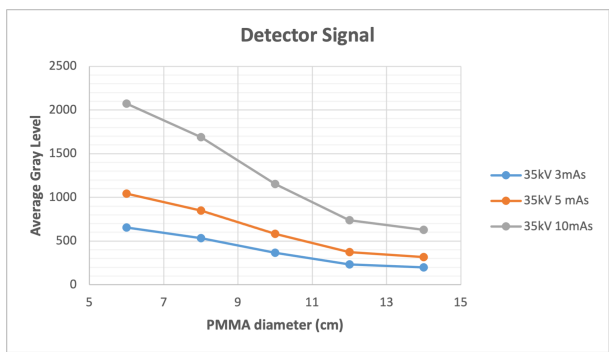
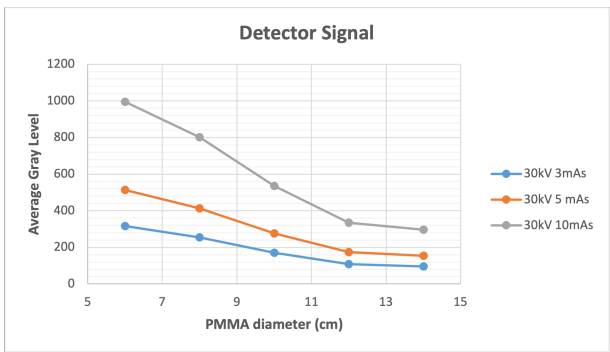


Figure 4.31: The graph shows the trend of the signal to the detector as the diameter of the AEC phantom increases for different combinations of voltages and mAs

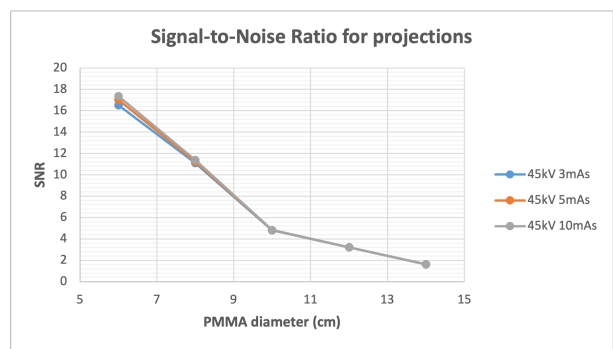
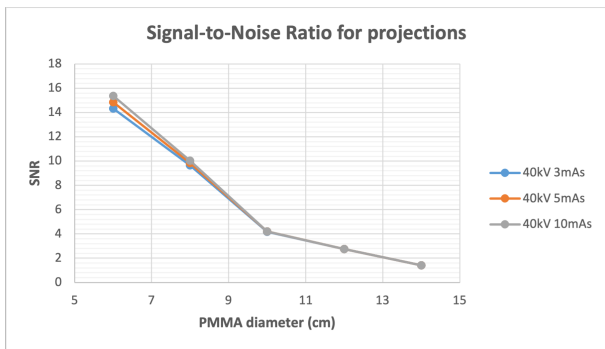
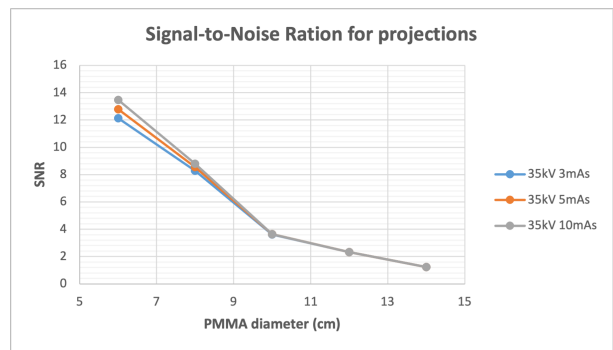
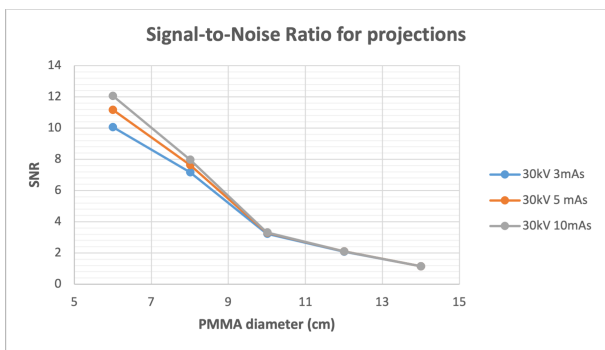


Figure 4.32: The graph shows the trend of the SNR as the diameter of the AEC phantom increases for different combinations of voltages and mAs

Thickness of compressed breast	FFDM	DBT
mm	counts	
5	1990	1000
10	1992	1181
15	1994	1336
20	1999	1472
25	1997	1445
30	2039	1409
35	2109	1545
40	2193	1590
45	2279	1509
50	2361	1581
55	2434	1618
60	2499	1772
65	2557	1845
70	2616	2072
75	2685	2272
80	2778	2454
85	2909	2590
90	3101	2727
95	3200	2881
100	3250	2909

Table 4.6: AEC single image counts set for high dose on IMS Giotto mammographs for FFDM and DBT modalities

The results of this initial setup of the AEC system are concluded by considering the evaluated thicknesses and inserting them into the dosimetric model explained in Section 3.2.6 in order to obtain the MGD values (Tables 4.7, 4.8).

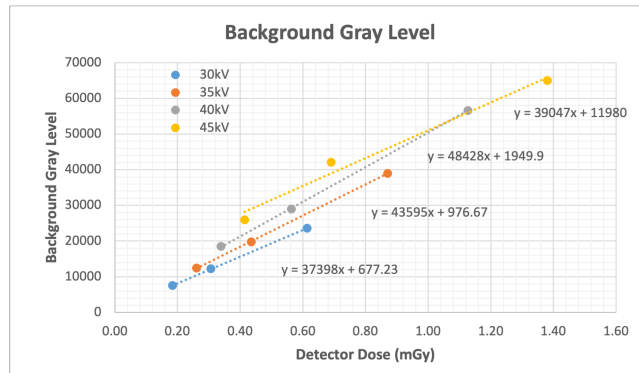


Figure 4.33: The graph shows the trend of the average number of counts in the background and the dose incident at the detector as the voltage considered increases

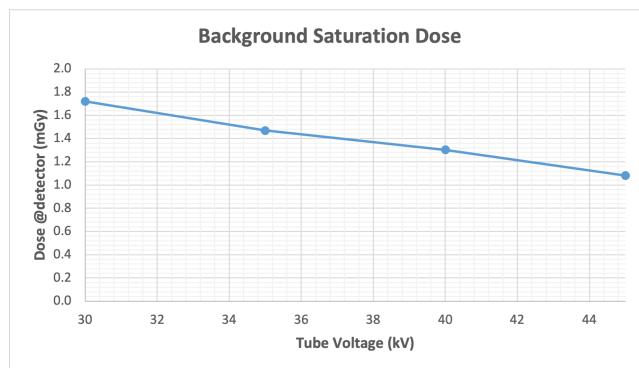


Figure 4.34: Saturation dose plotted against the increasing tube voltage

		Diameter (cm)				
kV	mAs	6	8	10	12	14
30	3	7.1	6.5	5.6	4.8	4.3
30	5	11.7	10.8	9.4	8.2	7.2
30	10	23.4	21.5	18.7	16.4	14.4
35	3	10.3	9.5	8.3	7.2	6.4
35	5	17.2	15.8	13.7	12.1	10.6
35	10	34.3	31.6	27.6	24.1	21.3
40	3	14.5	13.3	11.6	10.2	9.1
40	5	24.2	22.3	19.5	17.1	15.1
40	10	48.4	44.5	39.1	34.1	30.2
45	3	18.5	17.1	14.9	13.1	11.6
45	5	30.9	28.4	24.9	21.8	19.4
45	10	61.8	56.8	49.9	43.8	38.8

Table 4.7: MGD values at the varying diameters, for a fixed height of 10 cm and 80 projections

		Diameter (cm)				
kV	mAs	6	8	10	12	14
30	3	5.3	4.8	4.2	3.6	3.2
30	5	8.7	8.1	7.1	6.1	5.4
30	10	17.6	16.2	14.1	12.3	10.7
35	3	7.6	7.1	6.2	5.4	4.8
35	5	12.8	11.8	10.4	9.1	7.9
35	10	25.6	23.7	20.6	18.1	15.9
40	3	10.8	10.1	8.7	7.7	6.8
40	5	18.1	16.6	14.6	12.7	11.3
40	10	36.3	33.4	29.3	25.5	22.6
45	3	13.9	12.7	11.2	9.8	8.6
45	5	23.2	21.3	18.6	16.4	14.5
45	10	46.4	42.6	37.5	32.7	29.1

Table 4.8: MGD values at the varying diameters, for a fixed height of 10 cm and 60 projections

4.5.1 Image quality evaluation

In this section we proceed to the evaluation and comparison of the image quality in the different reconstruction methods. The ultimate goal is not exactly to obtain absolute values that quantify the image quality, but to obtain comparable quantitative measures that can compare the reconstruction methods considered for the CBCT project. Therefore, both the quantitative and qualitative evaluation of the individual methods is carried out first, and then, a more general evaluation that considers them in comparison is performed.

Six data sets (shown in Table 4.9) acquired with 60,80 projections, 30,35 kV and 2,4,6 mAs/projection were used. The values chosen for the reconstructions were selected based on the results obtained in the previous section. The intent was in fact to explore a range in which there was an acceptable signal level but which still fell within the dosimetry range recommended for the examination. The choice of this dataset derives also from the need to limit the total scan time (keep it under 30 seconds) and from the construction limits of the detector which, as previously mentioned, is not optimized for a CBCT exam. This translates into a buffer limit of the detector which allows a maximum of 80 acquirable projections. The question to which this section answers is, therefore, what are the visual and quantitative results as the physical parameters (voltage and dose) and the reconstruction parameters (number of iterations, voxel size and regularization parameter) vary.

Of all the datasets explored in the analysis, the results of the most significant

n. proj	kV	mAs/proj	mAs tot.	Dose @ SRD (mGy)	MGD (mGy)
60	30	2	120	9.7	2.3
60	30	4	240	19.5	4.5
60	30	6	360	29.1	6.9
60	35	2	120	13.8	3.3
60	35	4	240	27.6	6.7
60	35	6	360	41.5	10.1
80	30	2	160	12.9	3.1
80	30	4	320	25.9	6.1
80	30	6	480	38.9	9.1
80	35	2	160	18.5	4.5
80	35	4	320	36.9	9
80	35	6	480	55.3	13.5

Table 4.9: Datasets considered to evaluate the impact on CBCT reconstruction image quality caused by the variation of some physical parameters

ones are reported for each reconstruction method.

Filtered Back Projection

Results for the FBP method are reported in Figure 4.35. No quantitative measures have been obtained for this method. It was, in fact, rapidly abandoned because of the introduction of geometric artifacts that disturbed the analysis. This is probably due to the low number of projections that, in the FBP reconstruction, strictly limits the quality of the final image.

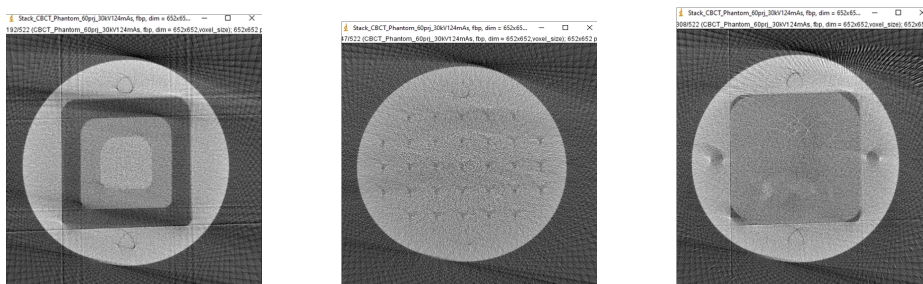


Figure 4.35: Clinical layer, layer for the evaluation of geometric accuracy and layer of the evaluation of MTF and CNR for the FBP reconstruction method

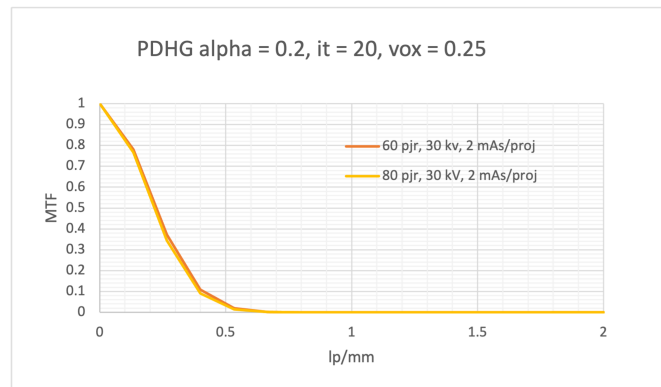


Figure 4.36: MTF plot for determined parameters: 20 iterations, regularization parameter equal to 0.2 and voxel size equal to 0.25 mm. The impact of the change in the number of projections is assessed. For the PDHG reconstruction method.

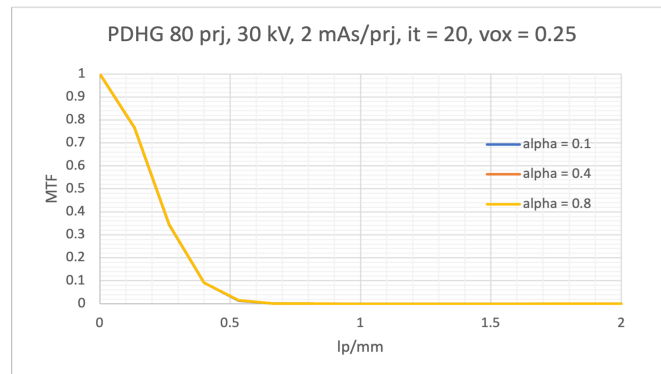
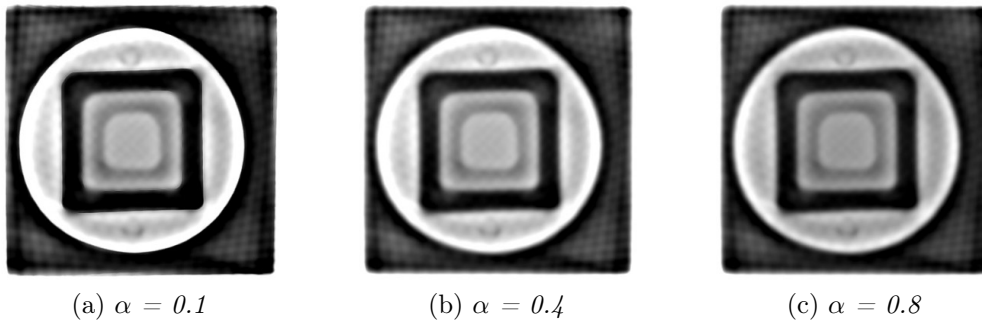
PDHG

As discussed in Section 3.2.4, iterative methods overcome the limitations of the FBP. The parameters that can be changed in these methods are the number of iterations (it) that the system does before stopping and producing the result, the smoothing parameter (α) that introduces a kind of blur in the image and the dimension of the voxel.

As can be seen in Figures 4.36, 4.37, for the PDHG method, the regularization parameter (α) and the number of projections do not seem to impact on the final value of the MTF. In fact, the curves in both figures are completely superimposable as the parameters involved vary. Below are the results for the MTF curves when the alpha parameter changes only in the case of 80 projections, for the equivalent case with 60 projections, please refer to the Appendix.

The same trend can also be observed in the images of the other layers of interest in the image quality phantom. In fact, both for the layer of interest with 1 mm air holes and for that of clinical details, the regularization parameter and the number of projections do not seem to affect the quality of the image in the least. For a visual observation of this trend, see the Appendix.

In the images (Figures 4.38, 4.39) it can be seen that, as α increases, SNR and CNR are quite constant. Instead, they increase with the dose. The SNR is, in fact, directly proportional to the square root of the dose. Therefore, as the latter increases, the signal-to-noise ratio increases and the contrast resolution improves. For this same reason SNR and CNR also increase with the number of projections.



(d) 80 projections, 30 kV, 2mAs/proj

Figure 4.37: Images and graph of the MTF as the α regularization parameter varies (0.1, 0.4, 0.8). The parameters set at 80 projections, 30 kV, 2mAs for projection, 20 iterations and 0.25 mm voxel dimension. For the PDHG reconstruction method.

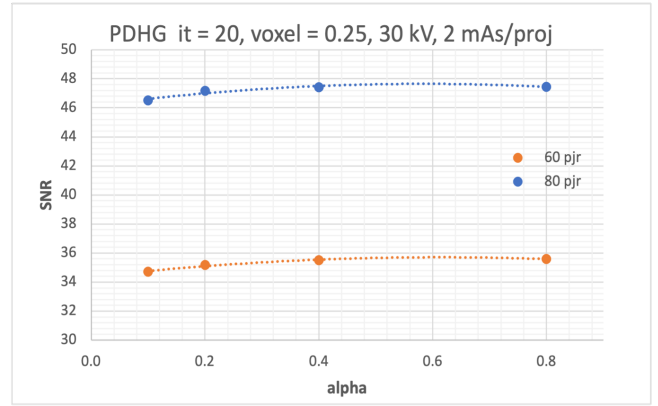
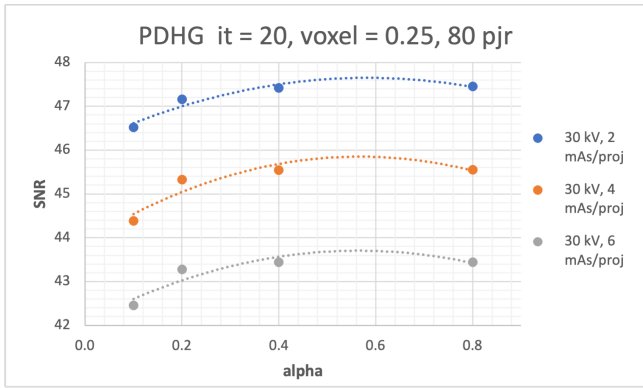


Figure 4.38: SNR graphs with varying α at different dose setups and for different number of projections. For the PDHG reconstruction method.

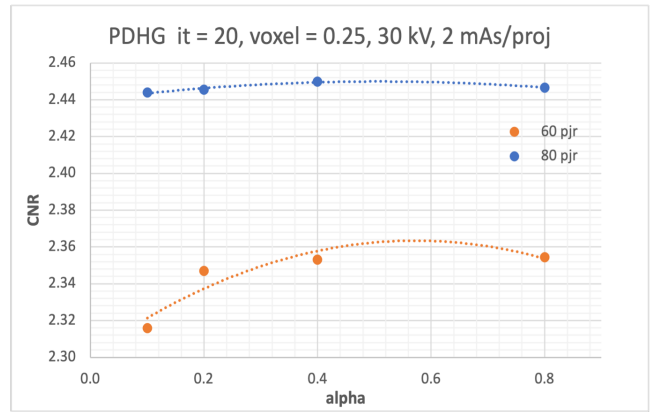
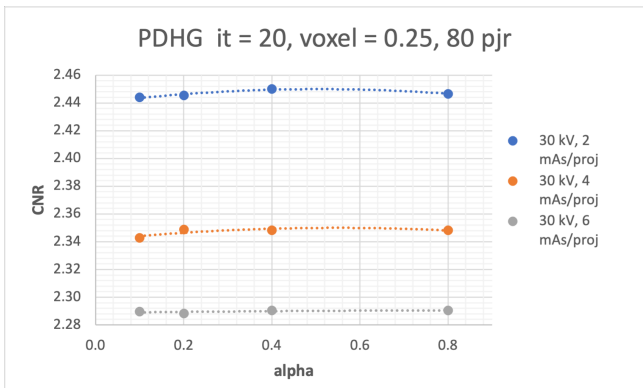
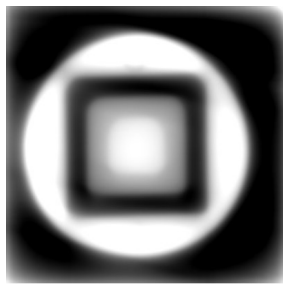


Figure 4.39: CNR graphs with varying α at different dose setups and for different number of projections. For the PDHG reconstruction method.

On the other hand, varying the number of iterations has a significant effect on image quality for the PDGH reconstruction method. As can be seen in Figure 4.40, increasing the number of iterations strongly clarifies the image content and improves the MTF curve. It can also be noted that, by observing the MTF graph, there is a large gap between the 10 and the 20 iterations. While, the distance between the 5 and the 10 and the 20 and the 30 iterations is thinner. This shows us that the significant value of iterations for which the effect on image quality is greater is precisely around 20 iterations. Below the results for the 80 projections case are shown, for the equivalent case with 60 projections, please refer to the Appendix.

Even if visually the spatial resolution seems to increase linearly with the increase of the number of iterations, in Figures 4.41 and 4.42 we witness a drop of both SNR and CNR in correspondence of the 30 iterations. This drop appears to be much steeper for the case of 60 projections than for 80, where SNR and CNR are slightly more constant. Images for the clinical details layer and the 1 mm air holes layer, as the number of iteration varies, are reported in the Appendix.



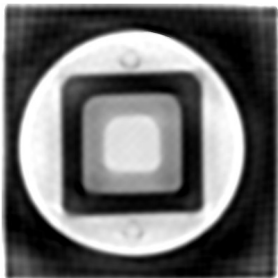
(a) $it = 5$



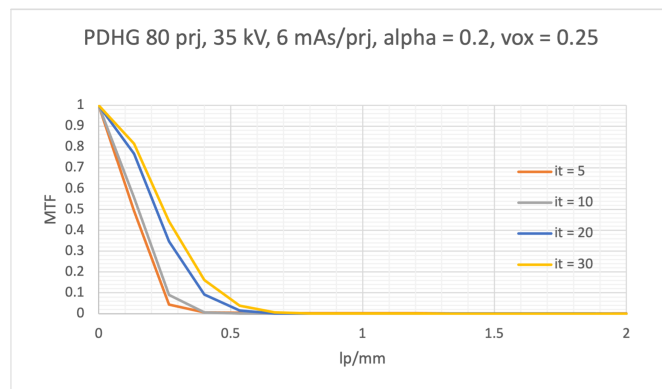
(b) $it = 10$



(c) $it = 20$



(d) $it = 30$



(e) 80 projections, 30 kV, 2mAs/proj

Figure 4.40: Images and graph of the MTF as the number of iterations varies (5, 10, 20, 30). The parameters set at 80 projections, 30 kV, 2mAs for projection, 0.2 regularization parameter and 0.25 mm voxel dimension. For the PDHG reconstruction method.

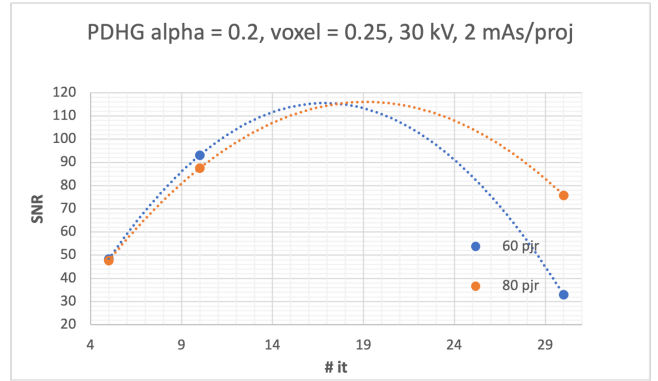
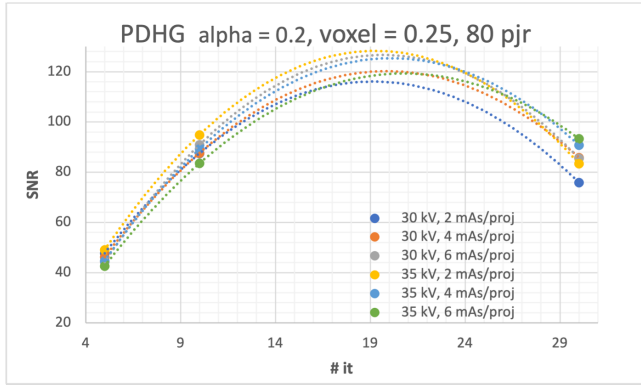


Figure 4.41: SNR graphs with varying number of iterations at different dose setups and for different number of projections. For the PDHG reconstruction method.

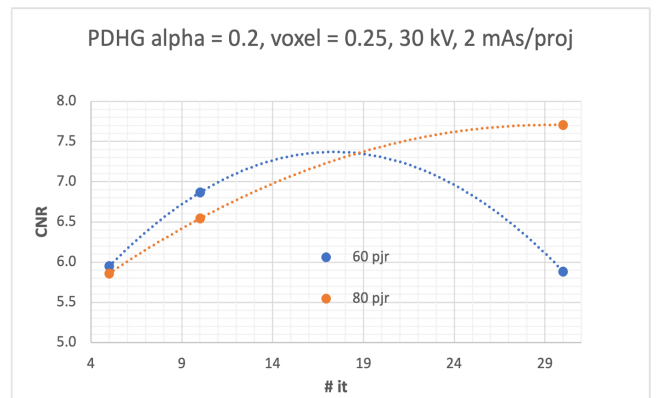
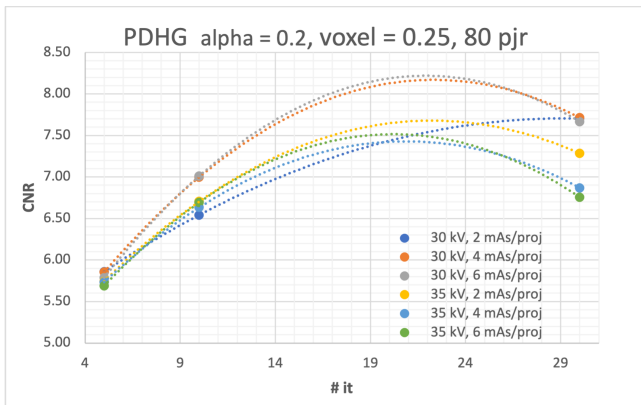
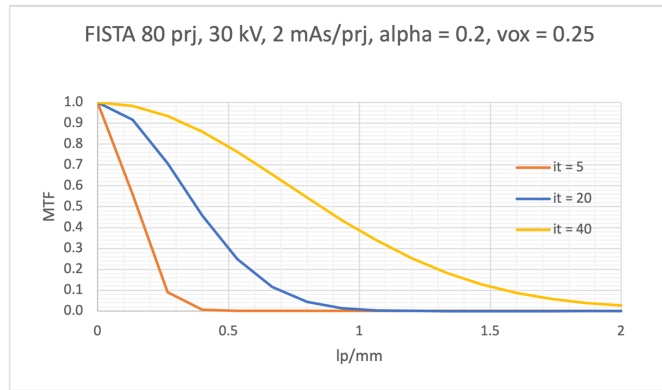
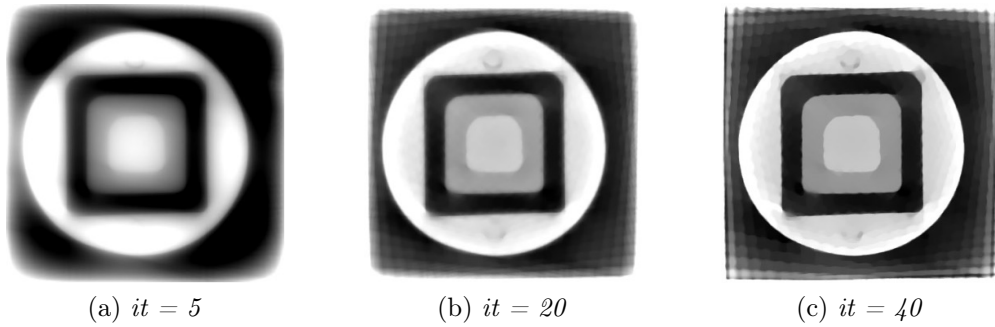


Figure 4.42: CNR graphs with varying number of iterations at different dose setups and for different number of projections. For the PDHG reconstruction method.



(d) 80 projections, 30 kV, 2mAs/projection

Figure 4.43: Images of the CNR and MTF analysis layer of the image quality phantom as the number of iterations varies. The regularization parameter at 0.2 and the voxel size at 0.25 mm are considered fixed. 80 projections, 30 kV, 2mAs/projection case. For the FISTA reconstruction method.

FISTA

The FISTA method has a generally better MTF than PDGH and strictly depends on both the regularization parameter (α) and the number of iterations (it). For the FISTA method, we immediately see that, as the number of iterations increase, the general appearance of the image and also the spatial resolution drastically gets better. This trend can be quantitatively assessed from the MTF graph. For comparison, the images related to the layer of interest for the calculation of the MTF are shown in Figure 4.43 in the same conditions that are reported above for the PDHG method. For a broader view of the range explored, and for the images of the other layers of interest, see the Appendix. From the observation of the images it can be deduced that, in order to have a sufficiently clear view of the structures it is necessary to perform at least 20 iterations.

On the other hand, based purely on the graphs, as the regularization parame-

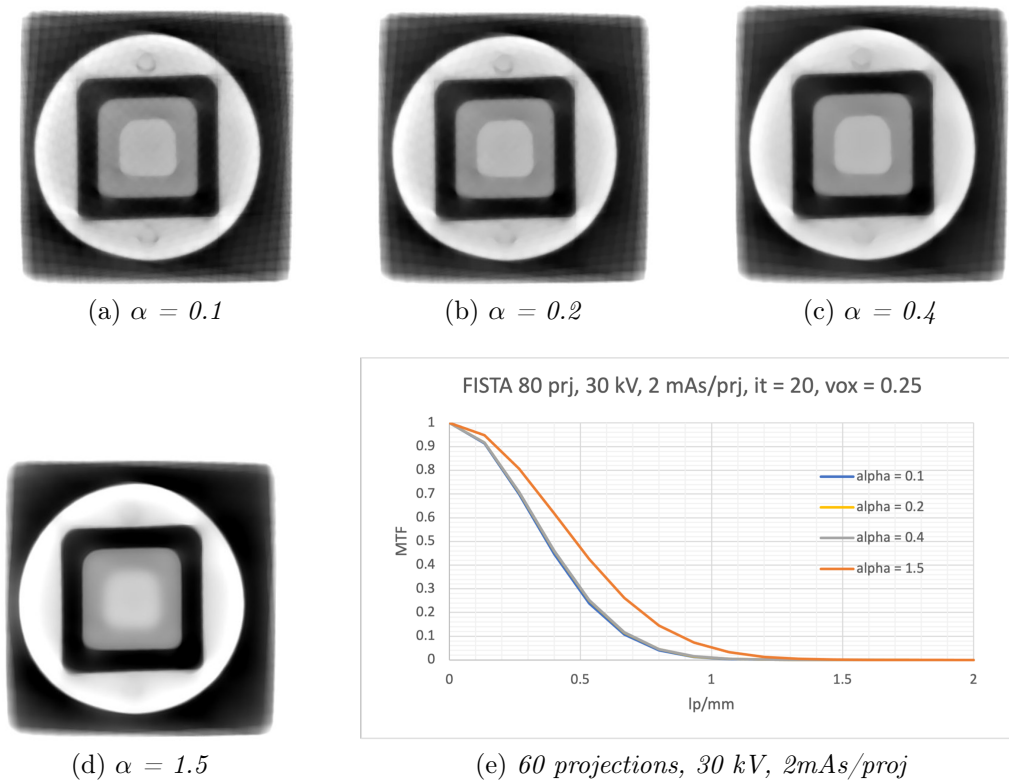
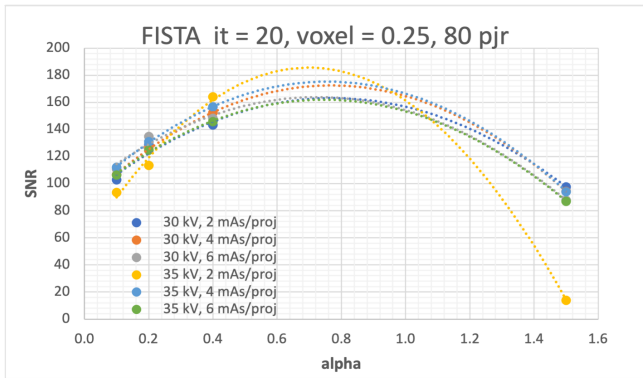
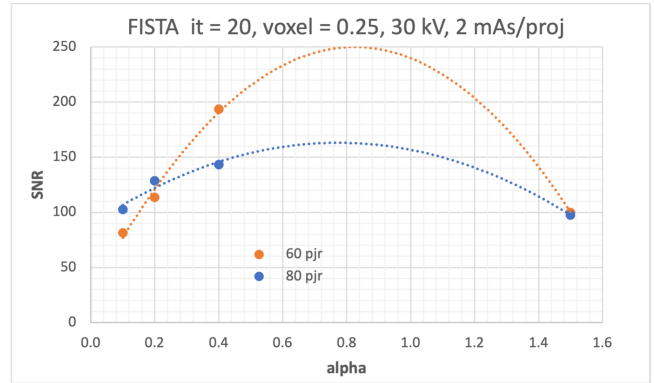


Figure 4.44: Images and graph of the MTF as the α regularization parameter varies (0.1, 0.2, 0.4 0.8, 1.5). The parameters set at 80 projections, 30 kV, 2mAs for projection, 20 iterations and 0.25 mm voxel dimension. For the FISTA reconstruction method.

ter increases, the MTF seems to rise. Despite that, this trend is not confirmed from the images (Figure 4.44) where, an excessively high regularization parameter brings too intensive blurring and loss of information. The effect of increasing the regularization parameter does not appear effective until it becomes exaggerated (in the case $\alpha = 1.5$). In fact, for the first three cases the MTF curves appear to be completely superimposable and also the images are pretty similar. Also SNR and CNR tend to drop drastically for high α values (Figures 4.45, 4.46).

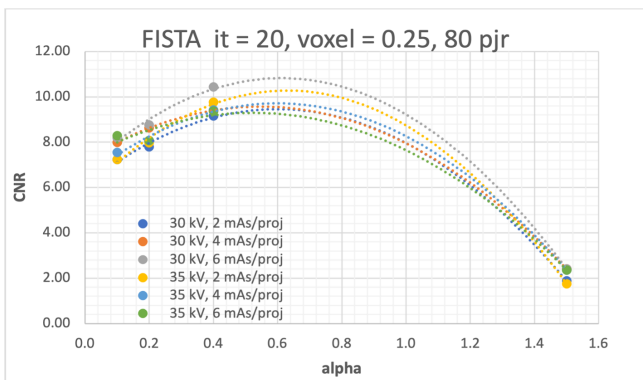


(a)

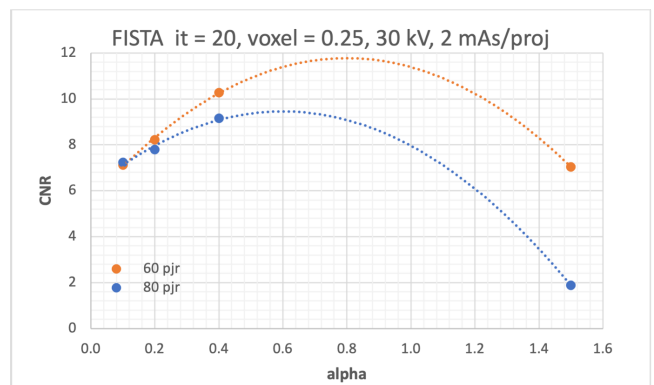


(b)

Figure 4.45: SNR graphs with α at different dose setups and for different number of projections. For the FISTA reconstruction method.

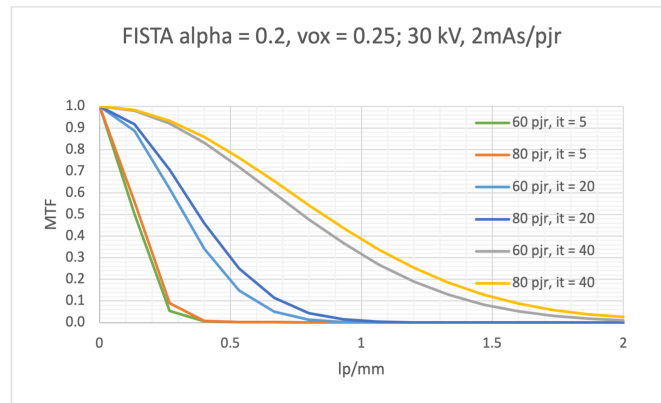


(a)

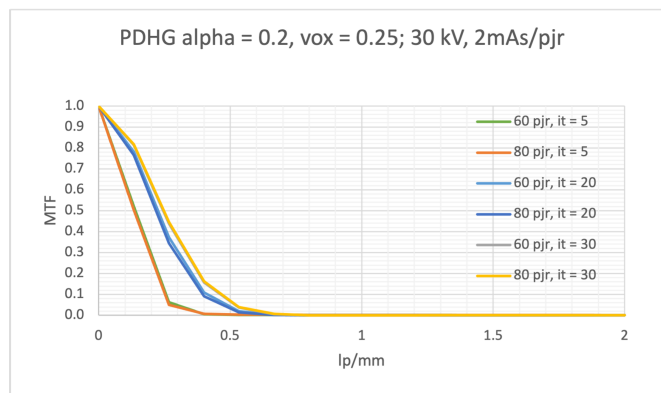


(b)

Figure 4.46: CNR graphs with α at different dose setups and for different number of projections. For the FISTA reconstruction method.



(a)



(b)

Figure 4.47: MTF graphs as the number of iterations and the number of projections vary. For both FISTA and PDHG reconstruction methods.

Figure 4.47 presents a summary of the most important characteristics of the two reconstruction methods analyzed in depth. Given the much greater impact of the number of iterations, this is considered with respect to the regularization parameter. And, for each case, we see the trend of the MTF as the number of projections varies. As can be seen, MTF is generally better for the FISTA method which, as can also be concluded from the previous images, generally provides better results. Moreover, in the latter method the impact of the number of iterations and the number of projections is much greater and it is qualitatively superior to PDHG. FISTA images appear less noisy and with fewer artifacts. It can be seen instead that PDHG images show many more artifacts, i.e. streaks, on which the regularization has little effect.

However, from the proposed images it is easy to realize that, in the FISTA method the proposed regularization is definitely too high, at least two orders of magnitude.

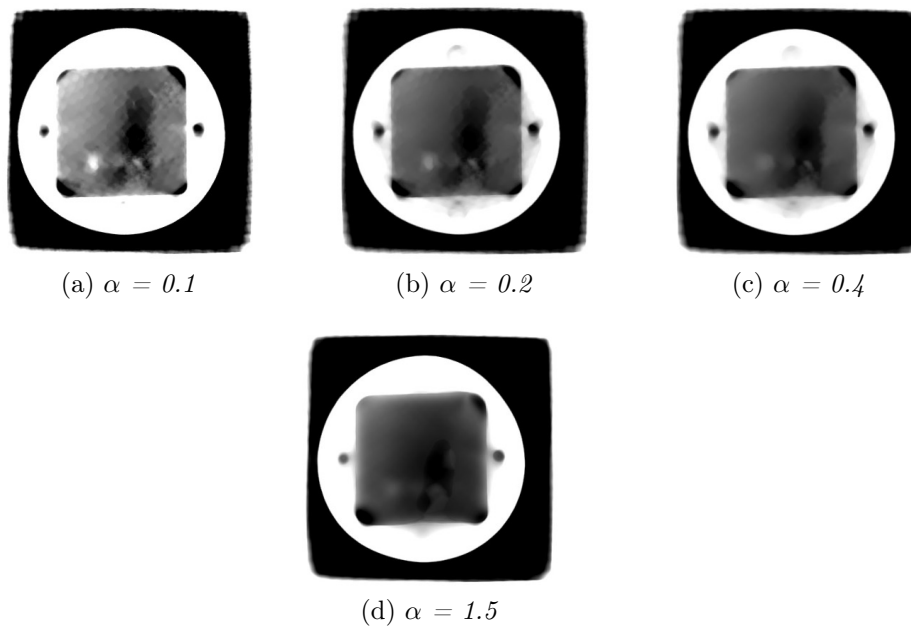


Figure 4.48: Images of the clinical details layer as the α regularization parameter varies. For 80 projections, 30 kV, 2 mAs/proj. For the FISTA reconstruction method.

In fact, especially in the clinical details control layer, we realize how much the blur introduced by the α parameter prevents the correct vision of most of the clinical details of interest (Figure 4.48). Two lower regularization images are proposed in Figure 4.49, where this problem is solved and many more details become visible, while before, the relevant clinical details such as micro-calcifications and fibers disappeared due to excessive filtration.

In both images we find the fibers, which in this case, due to the lower noise, appear more evident than in the FBP reconstruction (Figure 4.35). Also a new group of microcalcifications can be glimpsed. A slight blur persists, caused by a rather consistent binning that was necessary in order to run the reconstructions on the computer. In fact, one of the limitations of using non-optimized software for computational resources is the need to bin the images to speed up reconstruction and testing. This results in a loss of spatial resolution, but at the same time self-filtering of noise. One way to solve this problem and obtain more detailed reconstructions is the setting of a smaller voxel. However, this means a considerable waste of time. Figure 5.23 shows analyses of the time required for reconstructions with the FISTA method. For the same analysis with other parameters configuration see Appendix. The goal is both to give a scale of values that make the

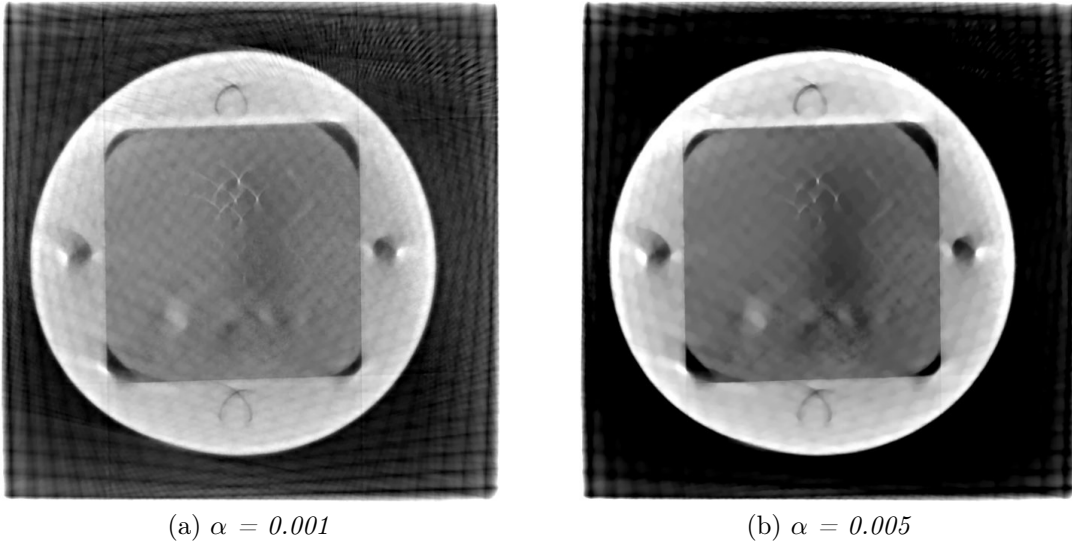


Figure 4.49: Images reconstructed with lower regularization parameter α .

reader aware of the time span we are talking about, and to show how the trend changes based on the number of iterations and the size of the voxel, parameters that strongly influence the reconstruction time.

It should be noted that all the times presented refer to the computer used in the company to run the reconstructions. The computer is equipped with an Intel(R) Core(TM) i7-9700 CPU @ 3.00 GHz 3.00 GHz, with an installed memory (RAM) of 16.0 GB and a GeForce GTX 1650 graphics card from Nvidia version 432.00. All reconstructions were done in GPU. It can be seen that the time required for processing a reconstruction with a very low voxel is considerably greater than that required for a larger voxel, where the time not only decreases significantly but also becomes more stable as the number of iterations.

The last topic to be addressed concerns geometric distortions. As said above, the imperfect description of the scan geometry in the reconstructions generates geometric distortions (non-circular air holes) that are shown in Figure 4.51. From the onset of these geometric distortions we can deduce that the scan geometry is not yet fully described. This is also due to the use of a standard projector described by the python package which implements the FISTA and PDHG codes. In the future it will be necessary to take a step forward and write a brand new and dedicated projector in order to better control the scan geometry entered in the reconstruction algorithm.

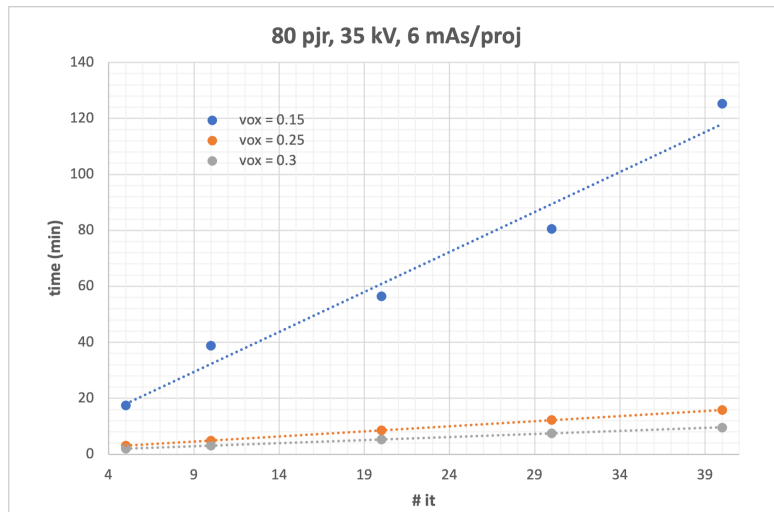


Figure 4.50: The graph shows the trend of the reconstruction time with the increasing number of iterations for different voxel dimensions in the 80 projections, 35 kV and 6 mAs/proj case. For the FISTA reconstruction method.

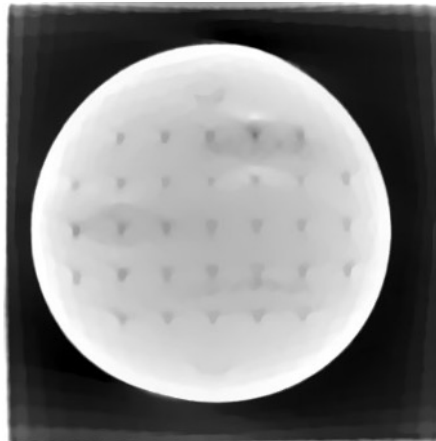


Figure 4.51: Image of the 1 mm air holes layer of the image quality phantom for the 80 projections, 35 kV, 6mAs/projection case. The regularization parameter at 0.2 and the voxel size at 0.25 and it = 40 are considered fixed. For the FISTA reconstruction method.

Chapter 5

Conclusions

The present study aimed to establish a characterization protocol for a prototype for CBCT and to investigate the feasibility of the project on the basis of the first results obtained. In the first part of the work, a measurement protocol, based on the international protocols EUREF, EFOMP (mammography and dental CBCT) and IEC, was set up to fully characterize the machine. The developed protocol includes the characterization of the high voltage generator, the 2D characterization of the detector and of the spectrum. This measurement protocol was needed to ensure that numerical data and quality controls can be produced during the production and prototyping of the device. So to evaluate if there are any changes for the development or for a constancy of quality. But above all, to have objective quantitative measures to be submitted to the ministry of health to obtain approval for a possible clinical study that will be conducted.

The second part of the thesis was, instead, focused on the evaluation, through quantitative and visual analyzes, of the CBCT exam feasibility in the hardware and software conditions currently proposed by IMS Giotto. The prototype was in fact developed differing from the technical choices of competing companies and developed for a different intended use. The objective was, therefore, not to certify the quality of the images obtained with numerical and quantitative results, but rather to investigate the range and characteristics of the machine in which the examination could take place, and evaluate the change in image quality at the vary of these parameters.

In the first part, the entirety of the device components were characterized. Accuracy and reproducibility measurements of tube current, voltage and current were used to characterize the high voltage generator. The tube and the spectrum emitted by the latter were instead characterized by montecarlo simulations carried out with a Python toolkit. In order to validate these simulations various dosimeters were used to compare the HVL values obtained with the simulated ones. Finally, the validity of the simulations carried out was guaranteed. At this point, the

characterization of the machine also included the characterization of the detector. First, a meticulous analysis on the measurement method to evaluate the MTF was conducted. After the evaluation of four measurement phantoms for the MTF it was concluded that the use of the edge device is the most suitable both for the 2D characterization of the detector, than for the evaluation of the image quality in 3D. The method was selected for its mathematical robustness and little dependence on positioning with respect to the focal spot projection.

After that, a real comparison between the two detectors available in IMS Giotto (Varex with indirect conversion and ScreenPlus with direct conversion) was carried out according to measurements of MTF, NPS and DQE in order not only to characterize the part of the image receptor in the machine but also in order to motivate the choice of the detector mounted in the prototype. It could be concluded that Varex responded more precisely to specific requests for this type of examination. In fact, it is concluded that the indirect conversion detector is faster, much less sensitive to electronic noise at very low doses (both in FFDM and in DBT modalities) and it is cheaper. In particular, the low sensitivity to noise at low doses, was decisive for the choice of the detector which, in the CBCT application, will be fundamental. In fact, the exam in question necessarily requires very short pulses, which implies a very low dose per single image and a fairly high noise.

Subsequently, in the thesis work a treatment on dosimetry is carried out with a phantom with variable diameters in order to identify a range of doses that allows to obtain a sufficient signal to the detector and remains, in any case, in the range of clinical limits for the feasibility of the exam. This is a first step in setting up an AEC system in the future. In fact, what IMS Giotto hopes is to be able to create a machine which, unlike competing devices based on semi-automatic systems, is also equipped with a real AEC.

Finally, starting from these dosimetric analyzes on the value of the signal and the corresponding dose value, a range is selected, also net of the technical limitations of the machine that we remember not to be optimized for CBCT, to investigate the variation, in a visual and also quantitative way, of the quality of the image as some physical parameters (voltage and dose) and specific to the mathematical method of reconstruction (number of iterations, voxel size and regularization parameter) vary. We conclude that iterative methods, based on mathematical methods of modeling the image creation process, are more suitable for scans with a low number of projections. In the case of this project this is a fundamental point because of a buffer limit on the detector that allows the acquisition of a maximum of 80 projections. To improve the spatial resolution it is possible to act on the number of iterations, with a consequent cost of computational time. Instead, to reduce the noise and artifacts generated by the low number of projections, a mathematical process called regularization is introduced. The image quality is therefore

a compromise between voxel size, number of iterations, regularization parameter and calculation speed. From the results we can conclude however that, among the tested algorithms, FISTA is the one that performs the best, having a better MTF and better visual results. The parameters that strongly influence this method are surely the number of projections and the number of iteration (to a greater extent). However, in this thesis the choice of the regularization parameter have been too high. Tested values are of the order of (0.1, 0.8, 1) while has been observed how the lowering of this parameter of two orders of magnitude can have an impact on the final result. The problems related to timing and also to the impact of some of these parameters on image quality are also certainly determined by the mathematical projector used by the reconstruction method to obtain the final image. A next step that will be carried out by the company is in fact to proceed with the writing of its own projector and therefore detach itself from the pre-packaged tools used up to this moment.

Appendix

CV					
Nominal kV	kVp	kV_{mean}	mA_{mean}	$A_{filament}$	ms
19	0.5%	0.5%	0.1%	0.1%	0.2%
20	0.4%	0.4%	0.1%	0.1%	0.3%
21	0.4%	0.5%	0.1%	0.1%	0.2%
22	0.3%	0.3%	0.1%	0.1%	0.2%
23	0.3%	0.3%	0.1%	0.1%	0.2%
24	0.3%	0.3%	0.1%	0.1%	0.2%
25	0.3%	0.3%	0.1%	0.1%	0.2%
26	0.3%	0.3%	0.1%	0.1%	0.2%
27	0.2%	0.2%	0.1%	0.1%	0.1%
28	0.3%	0.3%	0.1%	0.1%	0.2%
29	0.2%	0.2%	0.0%	0.1%	0.1%
30	0.2%	0.1%	0.1%	0.1%	0.2%
31	0.2%	0.3%	0.1%	0.2%	0.5%
32	0.2%	0.2%	0.1%	0.2%	0.2%
33	0.2%	0.2%	0.1%	0.1%	0.1%
34	0.2%	0.2%	0.0%	0.1%	0.4%
35	0.3%	0.3%	0.1%	0.1%	0.3%
36	0.2%	0.2%	0.1%	0.1%	0.2%
37	0.2%	0.2%	0.1%	0.2%	0.3%
38	0.2%	0.2%	0.1%	0.1%	0.2%
39	0.3%	0.3%	0.1%	0.1%	0.2%
40	0.2%	0.2%	0.1%	0.1%	0.2%
41	0.2%	0.2%	0.1%	0.2%	0.3%
42	0.2%	0.2%	0.1%	0.2%	0.2%
43	0.1%	0.1%	0.1%	0.2%	0.2%
44	0.2%	0.1%	0.1%	0.2%	0.3%
45	0.2%	0.2%	0.0%	0.2%	0.2%
46	0.1%	0.1%	0.1%	0.1%	0.3%
47	0.2%	0.2%	0.1%	0.2%	0.2%
48	0.1%	0.1%	0.1%	0.2%	0.1%
49	0.1%	0.2%	0.1%	0.1%	0.2%

Table 5.1: Variation coefficients (CV) obtained for each nominal kV value in the 19-49 range for all the control parameters (kV, mA, filament current and exposure time).

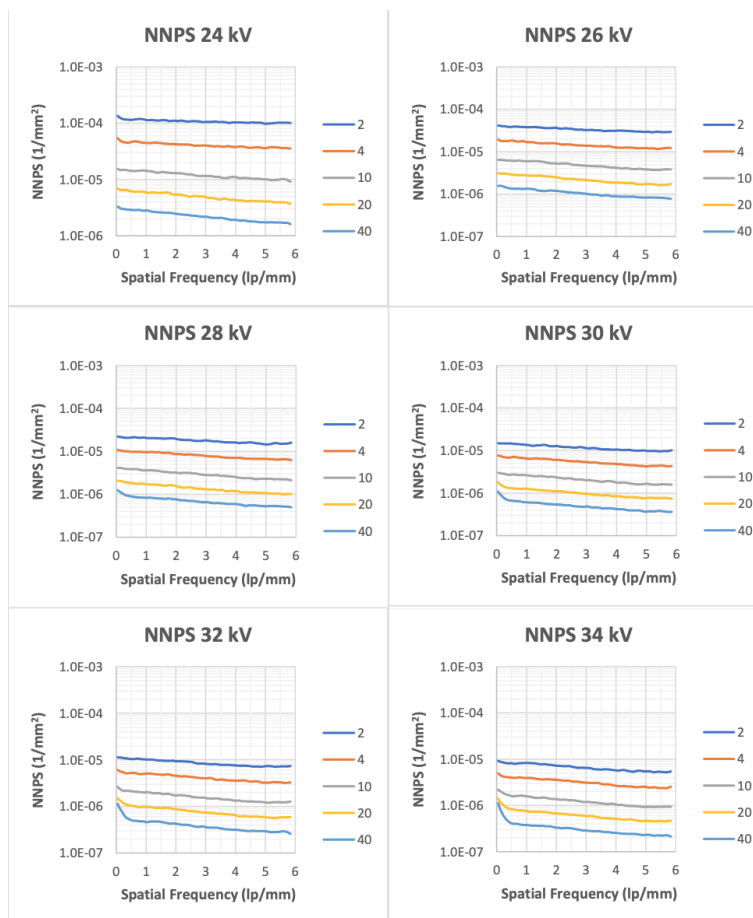


Figure 5.1: NNPS graphs, calculated at different energies, in FFDM mode for direct conversion detector.

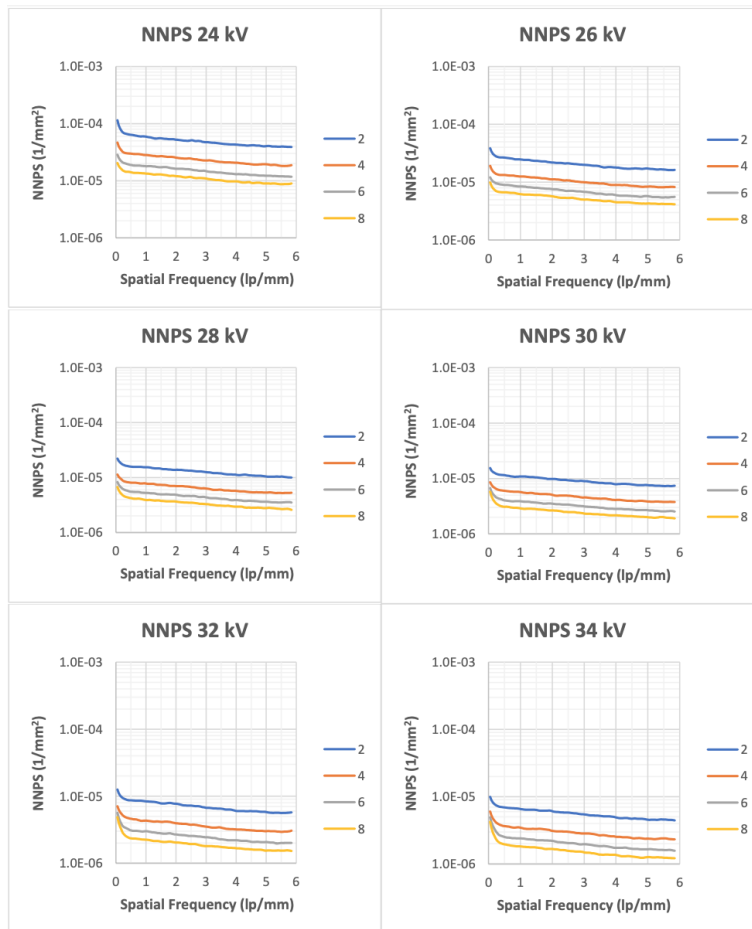


Figure 5.2: NNPS graphs, calculated at different energies, in DBT mode for direct conversion detector.

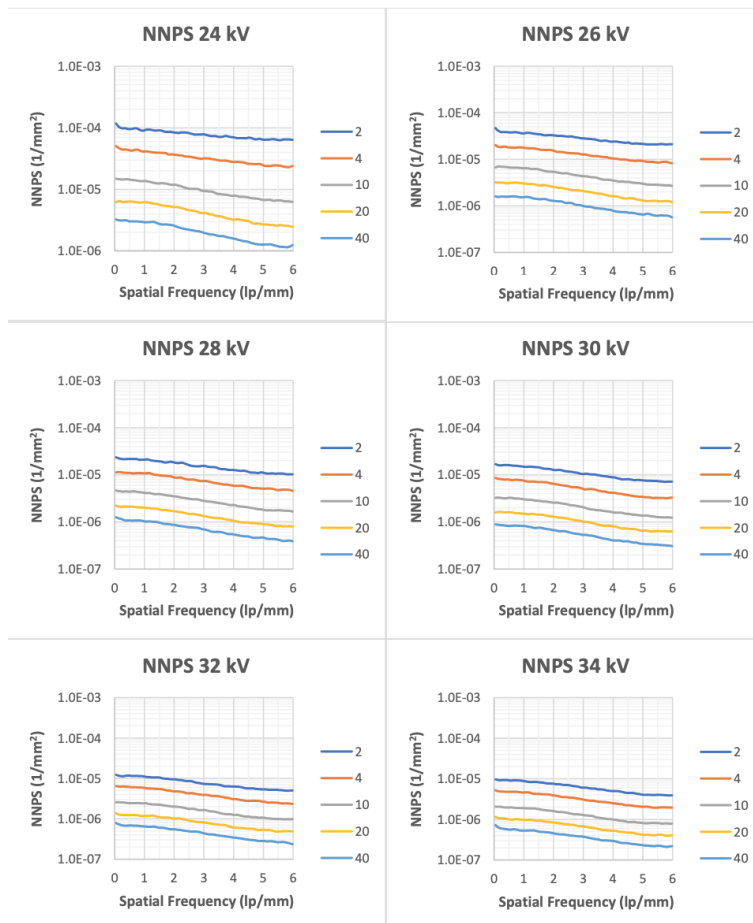


Figure 5.3: NNPS graphs, calculated at different energies, in FFDM mode for indirect conversion detector.

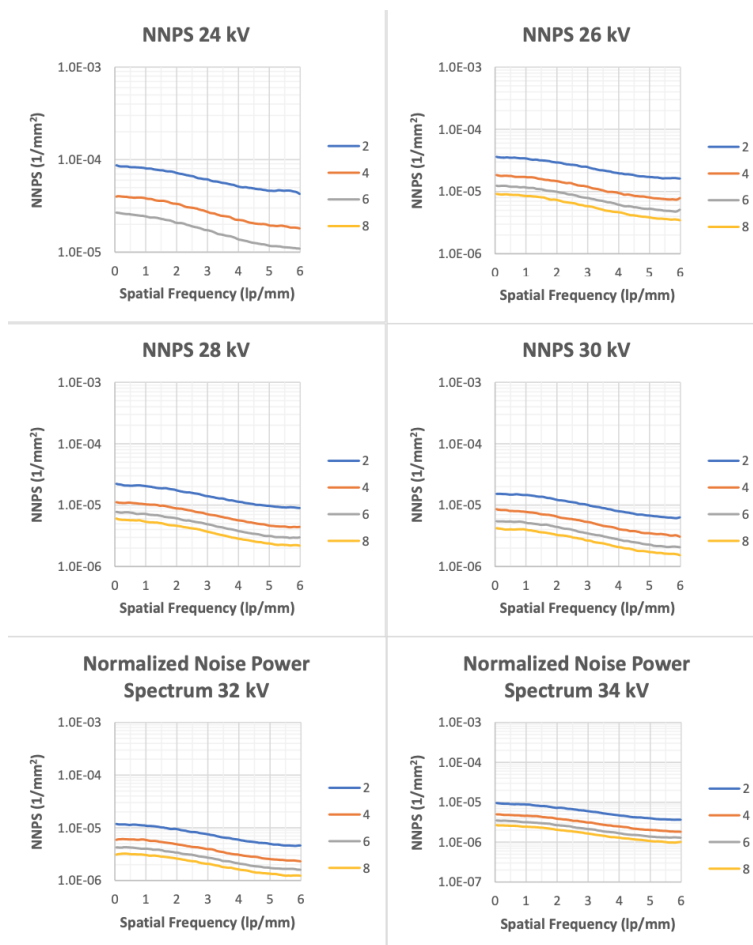


Figure 5.4: NNPS graphs, calculated at different energies, in DBT mode for indirect conversion detector.

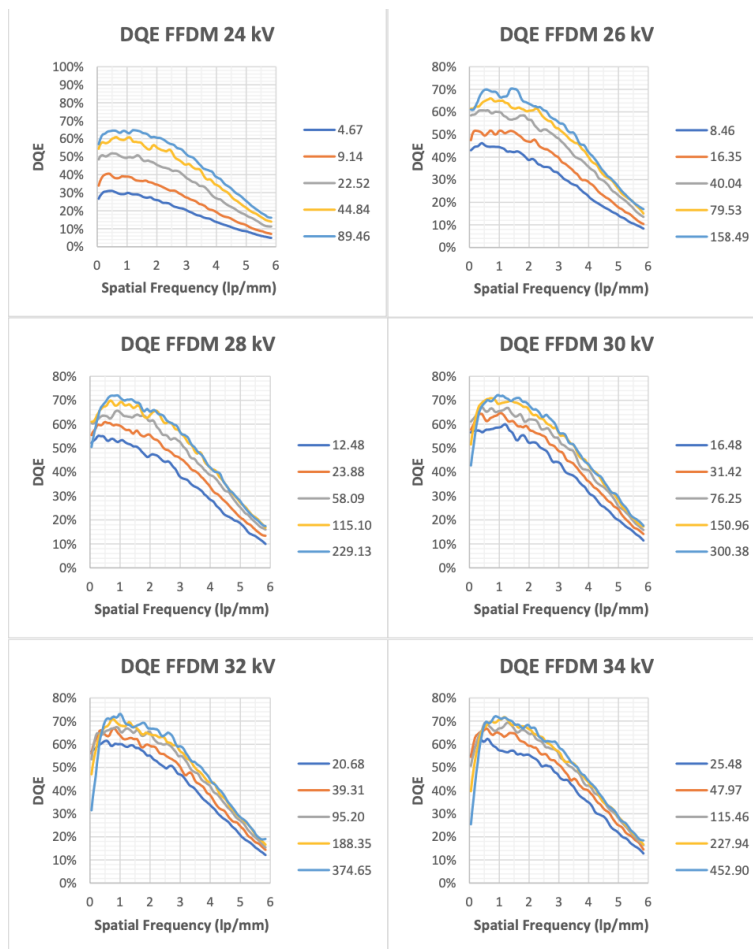


Figure 5.5: DQE graphs, calculated at different energies, in FFDM mode for direct conversion detector.

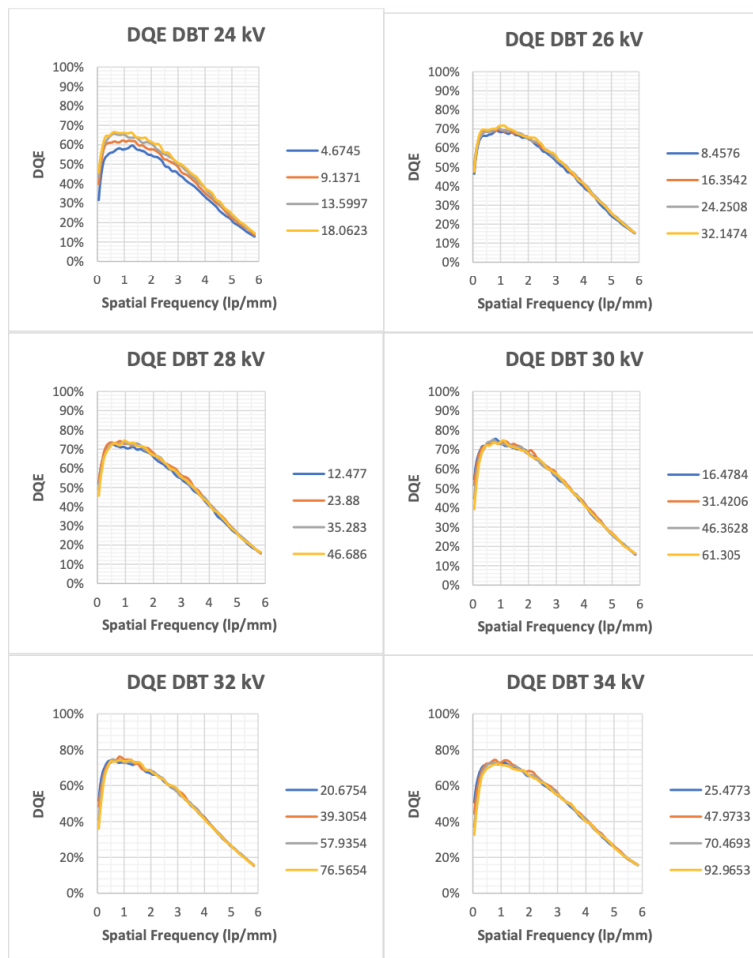


Figure 5.6: NNPS graphs, calculated at different energies, in DBT mode for direct conversion detector.

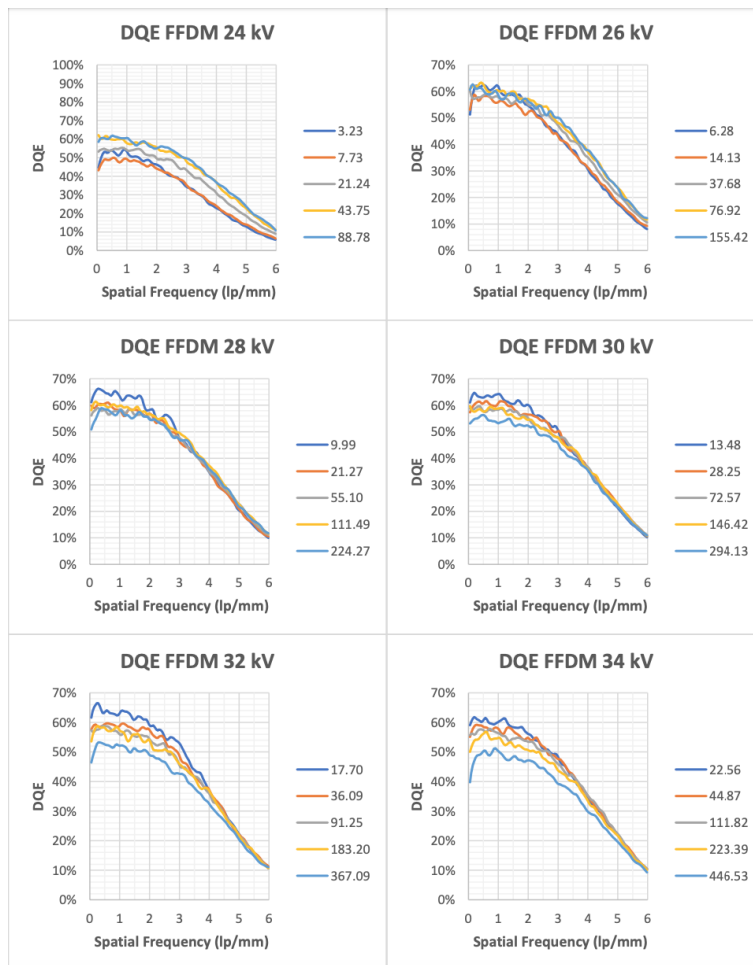


Figure 5.7: DQE graphs, calculated at different energies, in FFDM mode for indirect conversion detector.

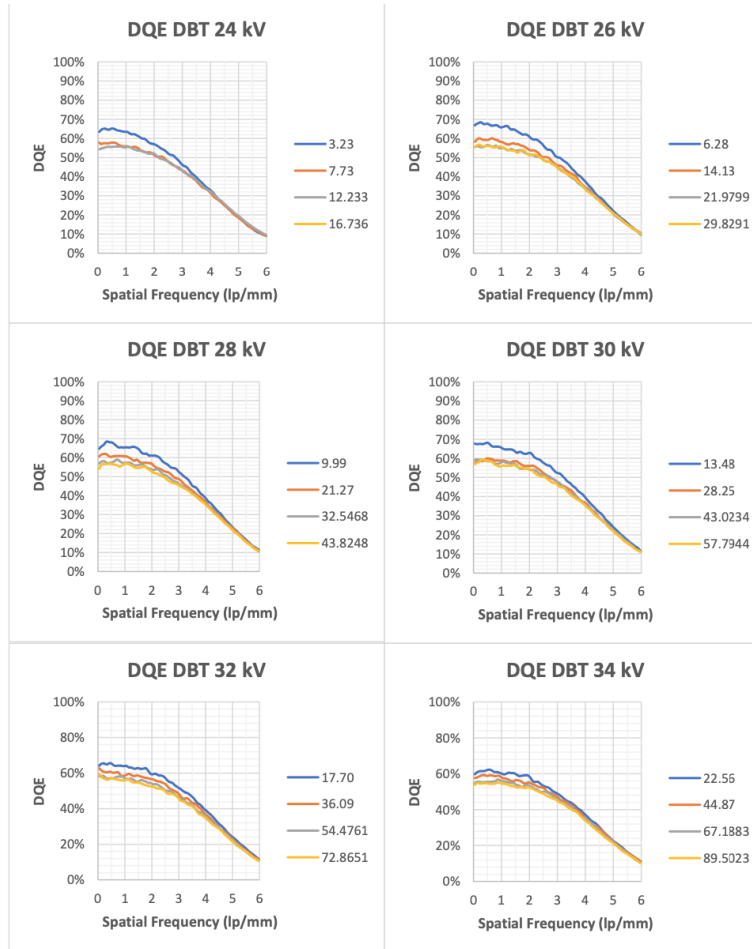
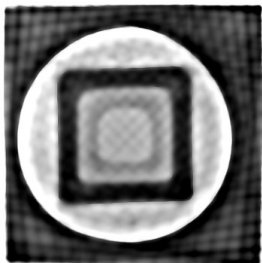
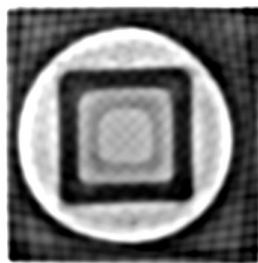


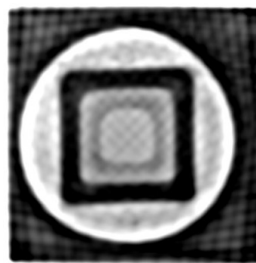
Figure 5.8: DQE graphs, calculated at different energies, in DBT mode for indirect conversion detector.



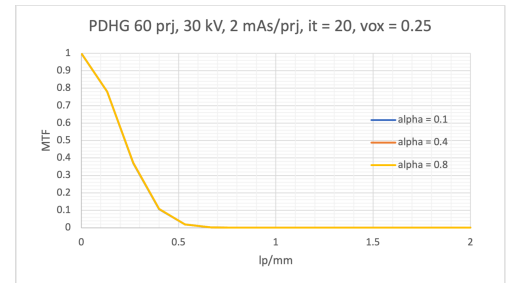
(a) $\alpha=0.1$



(b) $\alpha=0.4$

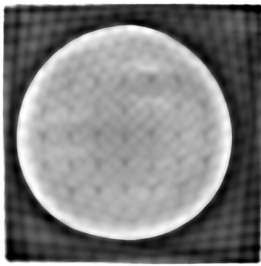


(c) $\alpha=0.8$

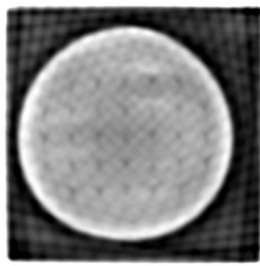


(d) 60 projections, 30 kV, 2mAs/proj

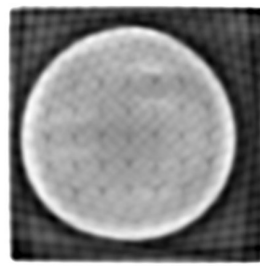
Figure 5.9: Images and graph of the MTF as the α regularization parameter varies (0.1, 0.4, 0.8). The parameters set at 60 projections, 30 kV, 2mAs for projection, 20 iterations and 0.25 voxel dimension. For the PDHG reconstruction method.



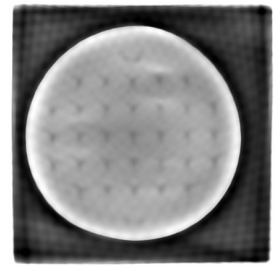
(a) $\alpha=0.1$, 60 projections, 30 kV, 2mAs/projection



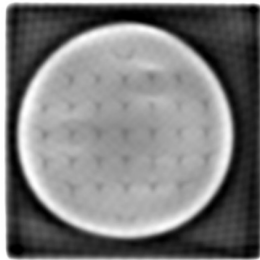
(b) $\alpha=0.4$, 60 projections, 30 kV, 2mAs/projection



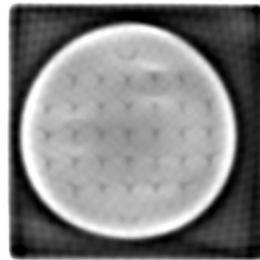
(c) $\alpha=0.8$, 60 projections, 30 kV, 2mAs/projection



(d) $\alpha=0.1$, 80 projections, 30 kV, 2mAs/projection

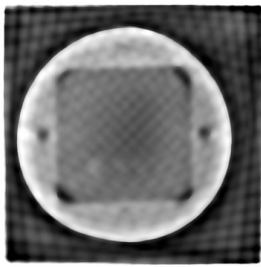


(e) $\alpha=0.4$, 80 projections, 30 kV, 2mAs/projection

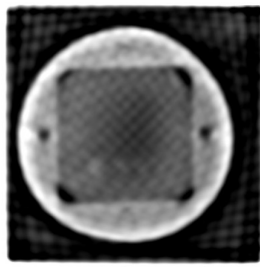


(f) $\alpha=0.8$, 80 projections, 30 kV, 2mAs/projection

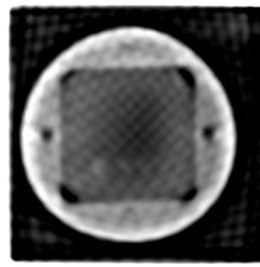
Figure 5.10: Images of the 1 mm holes layer, used for the evaluation of geometric distortions, as the α regularization parameter varies (0.1, 0.4, 0.8). For the two cases of 60 and 80 projections. For the PDHG reconstruction method.



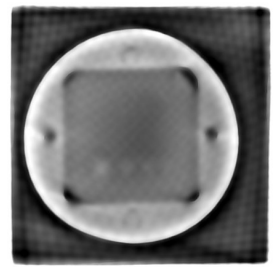
(a) $\alpha=0.1$, 60 projections, 30 kV, 2mAs/projection



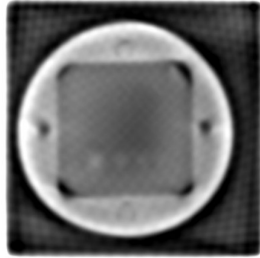
(b) $\alpha=0.4$, 60 projections, 30 kV, 2mAs/projection



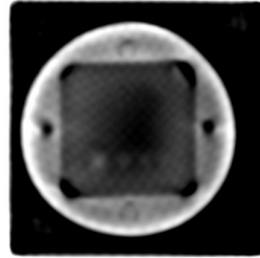
(c) $\alpha=0.8$, 60 projections, 30 kV, 2mAs/projection



(d) $\alpha=0.1$, 80 projections, 30 kV, 2mAs/projection

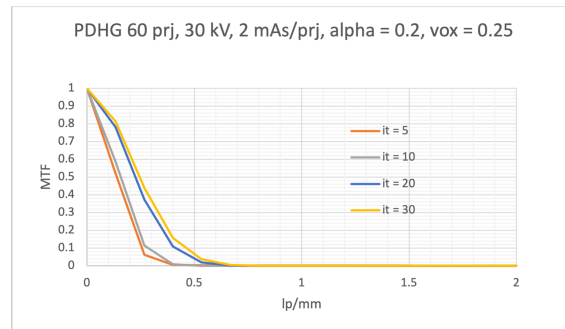
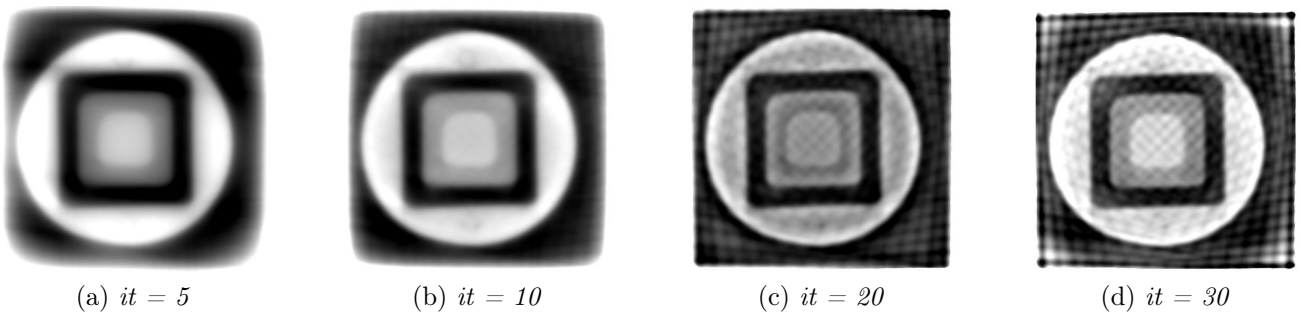


(e) $\alpha=0.4$, 80 projections, 30 kV, 2mAs/projection



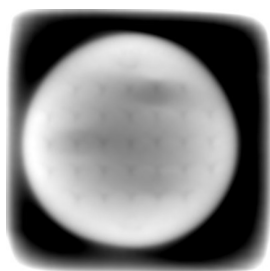
(f) $\alpha=0.8$, 80 projections, 30 kV, 2mAs/projection

Figure 5.11: Images of the clinical details layer as the α regularization parameter varies (0.1, 0.4, 0.8). For the two cases of 60 and 80 projections. For the PDHG reconstruction method.

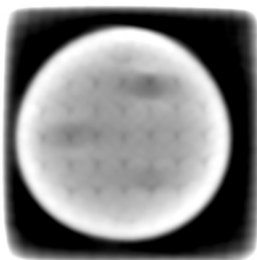


(e) 60 projections, 30 kV, 2mAs/proj

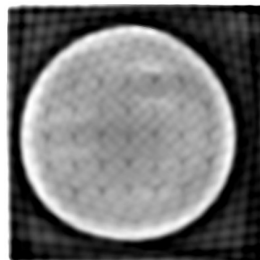
Figure 5.12: Images and graph of the MTF as the number of iterations varies (5, 10, 20, 30). The parameters set at 60 projections, 30 kV, 2mAs for projection, 0.2 regularization parameter and 0.25 voxel dimension. For the PDHG reconstruction method.



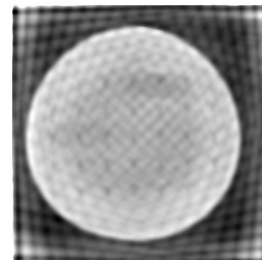
(a) *it=5, 60 projections, 30 kV, 2mAs/projection*



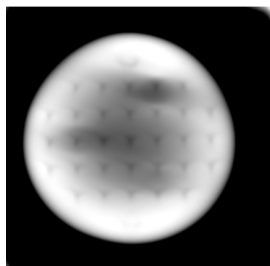
(b) *it=10, 60 projections, 30 kV, 2mAs/projection*



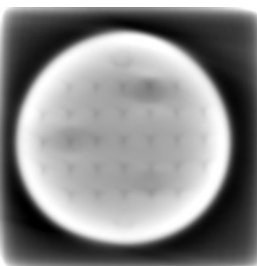
(c) *it=20, 60 projections, 30 kV, 2mAs/projection*



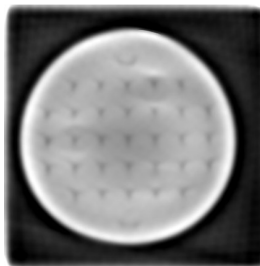
(d) *it=30, 60 projections, 30 kV, 2mAs/projection*



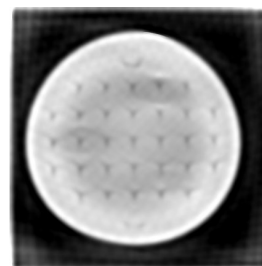
(e) *it=5, 80 projections, 30 kV, 2mAs/projection*



(f) *it=10, 80 projections, 30 kV, 2mAs/projection*

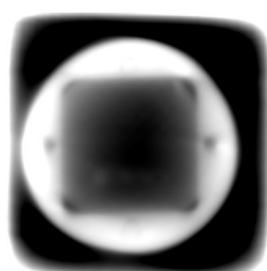


(g) *it=20, 80 projections, 30 kV, 2mAs/projection*



(h) *it=30, 80 projections, 30 kV, 2mAs/projection*

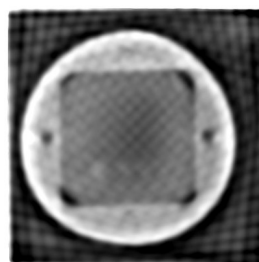
Figure 5.13: Images of the 1 mm holes layer, used for the evaluation of geometric distortions, as the number of iterations varies (5, 10, 20, 30). For the two cases of 60 and 80 projections. For the PDHG reconstruction method.



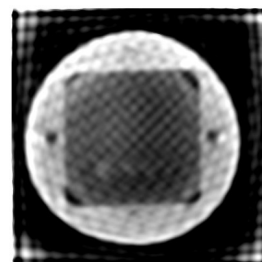
(a) $it=5$, 60 projections, 30 kV, 2mAs/projection



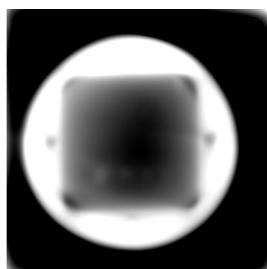
(b) $it=10$, 60 projections, 30 kV, 2mAs/projection



(c) $it=20$, 60 projections, 30 kV, 2mAs/projection



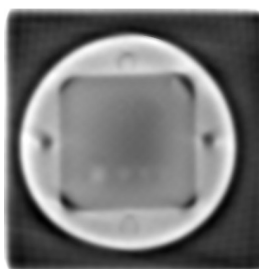
(d) $it=30$, 60 projections, 30 kV, 2mAs/projection



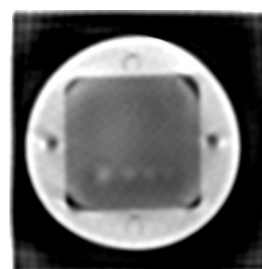
(e) $it=5$, 80 projections, 30 kV, 2mAs/projection



(f) $it=10$, 80 projections, 30 kV, 2mAs/projection



(g) $it=20$, 80 projections, 30 kV, 2mAs/projection



(h) $it=30$, 80 projections, 30 kV, 2mAs/projection

Figure 5.14: Images of the clinical details layer as the number of iteration varies (5, 10, 20, 30). For the two cases of 60 and 80 projections. For the PDHG reconstruction method.

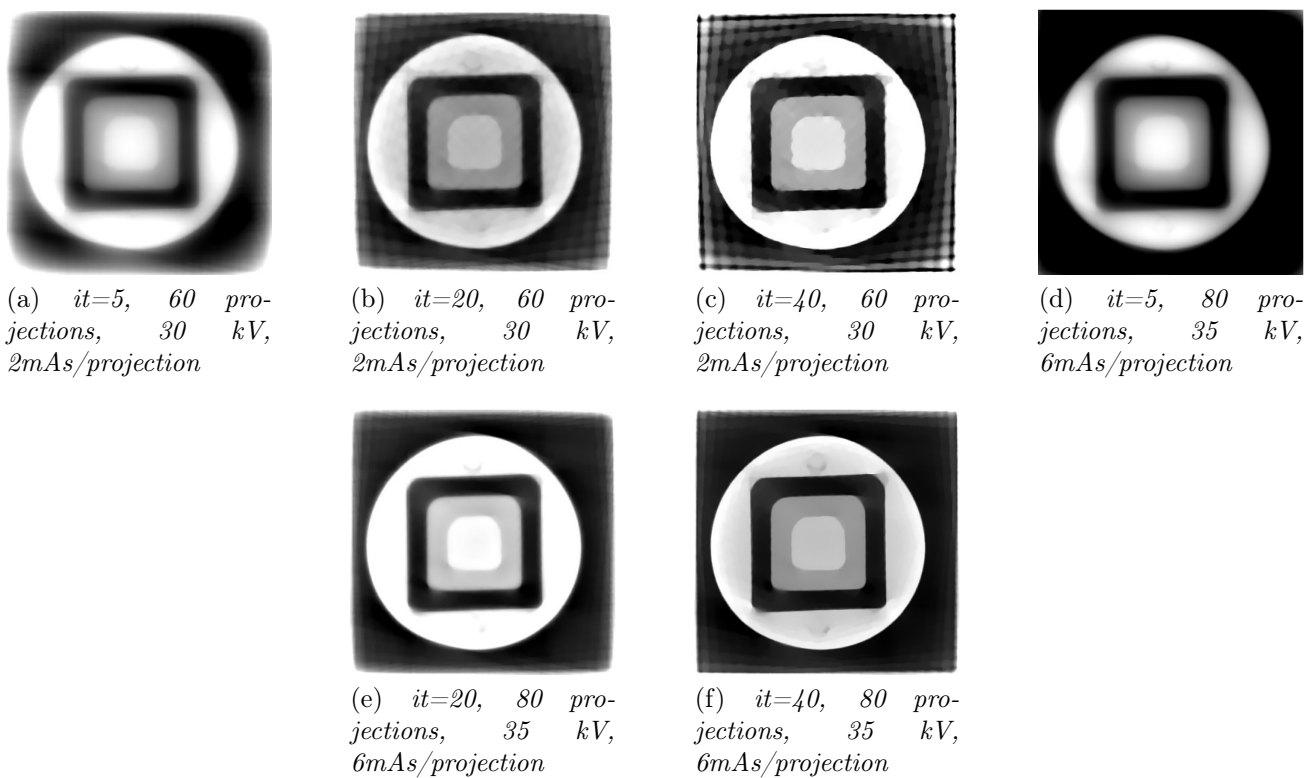
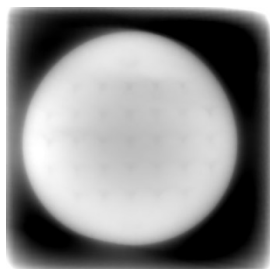
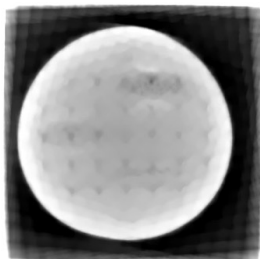


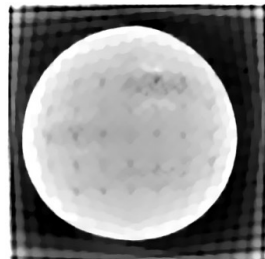
Figure 5.15: Images of the CNR and MTF analysis layer of the image quality phantom as the number of iterations varies. The regularization parameter at 0.2 and the voxel size at 0.25 are considered fixed, different dose cases are evaluated. For the FISTA reconstruction method.



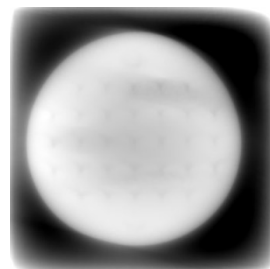
(a) *it=5, 60 pro-
jections, 30 kV, 2
mAs/projection*



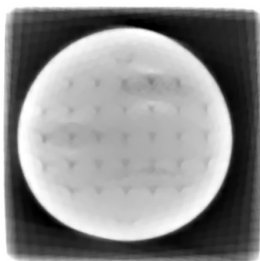
(b) *it=20, 60 pro-
jections, 30 kV, 2
mAs/projection*



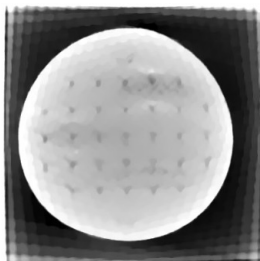
(c) *it=40, 60 pro-
jections, 30 kV, 2
mAs/projection*



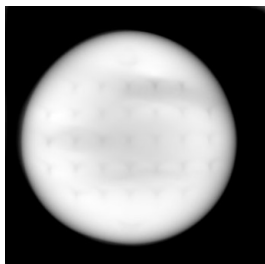
(d) *it=5, 80 pro-
jections, 30 kV, 2
mAs/projection*



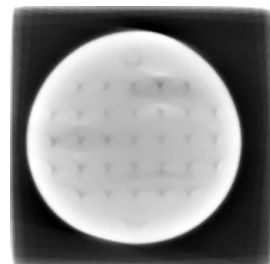
(e) *it=20, 80 pro-
jections, 30 kV, 2
mAs/projection*



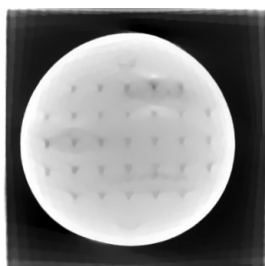
(f) *it=40, 80 pro-
jections, 30 kV, 2
mAs/projection*



(g) *it=5, 80 pro-
jections, 35 kV, 6
mAs/projection*

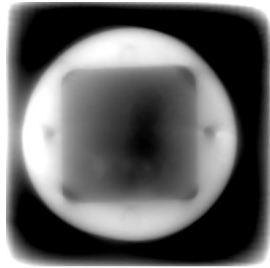


(h) *it=20, 80 pro-
jections, 35 kV, 6
mAs/projection*

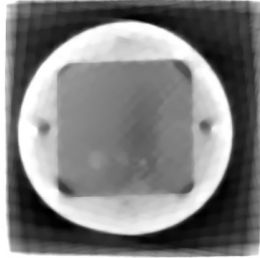


(i) *it=40, 80 pro-
jections, 35 kV, 6
mAs/projection*

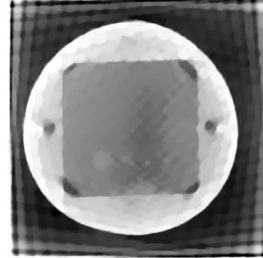
Figure 5.16: Images of the 1 mm air holes layer of the image quality phantom as the number of iterations varies. The parameters are fixed at $\alpha = 0.2$, voxel size = 0.25, for different dose cases. For the FISTA reconstruction method.



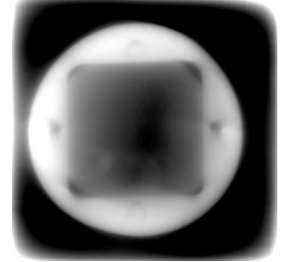
(a) *it=5, 60 projections, 30 kV, 2mAs/projection*



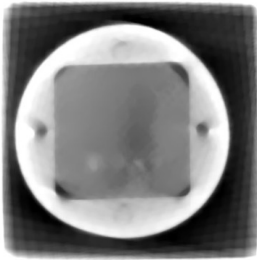
(b) *it=20, 60 projections, 30 kV, 2mAs/projection*



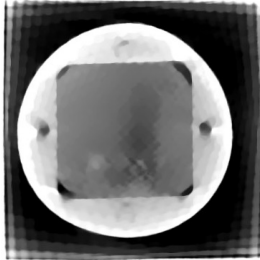
(c) *it=40, 60 projections, 30 kV, 2mAs/projection*



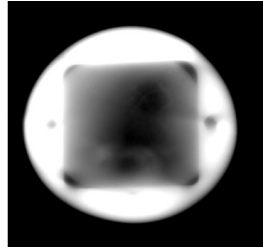
(d) *it=5, 80 projections, 30 kV, 2mAs/projection*



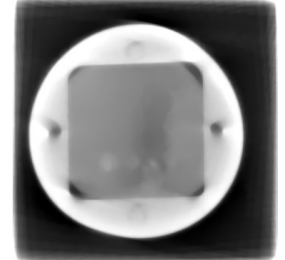
(e) *it=20, 80 projections, 30 kV, 2mAs/projection*



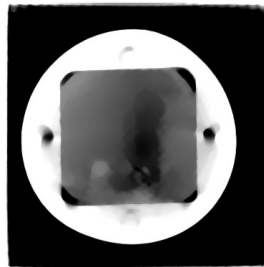
(f) *it=40, 80 projections, 30 kV, 2mAs/projection*



(g) *it=5, 80 projections, 35 kV, 6mAs/projection*

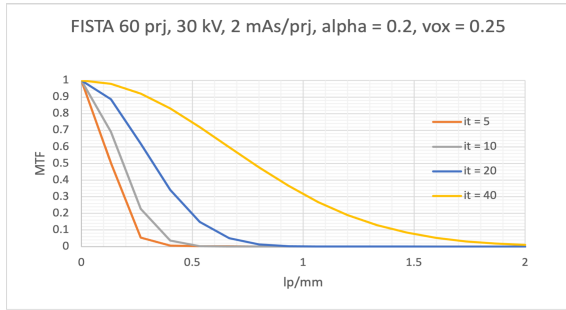


(h) *it=20, 80 projections, 35 kV, 6mAs/projection*

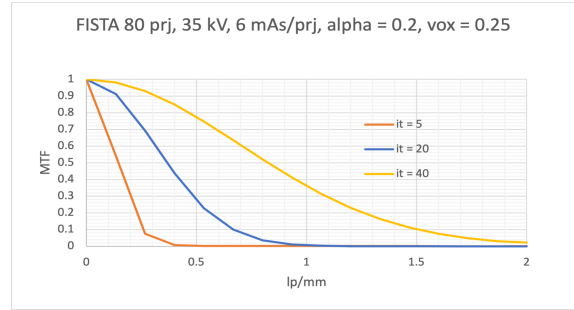


(i) *it=40, 80 projections, 35 kV, 6mAs/projection*

Figure 5.17: Images of the clinical details layer as the number of iterations varies. The regularization parameter at 0.2 and the voxel size at 0.25 are considered fixed, different dose cases are evaluated. For the FISTA reconstruction method.

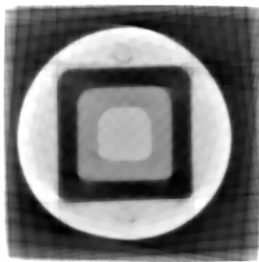


(a) 60 projections, 30 kV, 2mAs/projection

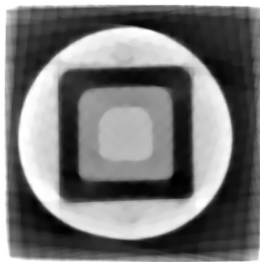


(b) 80 projections, 35 kV, 6mAs/projection

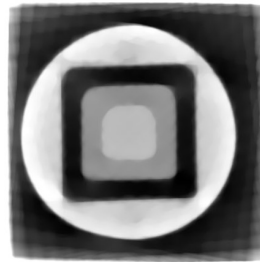
Figure 5.18: MTF graphs as the number of iteration varies. The regularization parameter at 0.2 and the voxel size at 0.25 are considered fixed. 80 projections, 30 kV, 2mAs/projection case. For the FISTA reconstruction method.



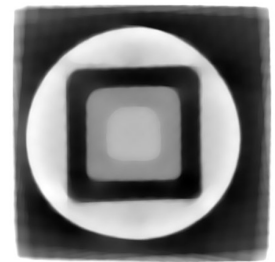
(a) $\alpha = 0.1$



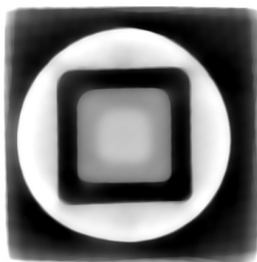
(b) $\alpha = 0.2$



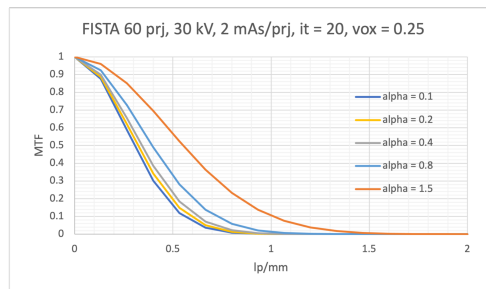
(c) $\alpha = 0.4$



(d) $\alpha = 0.8$

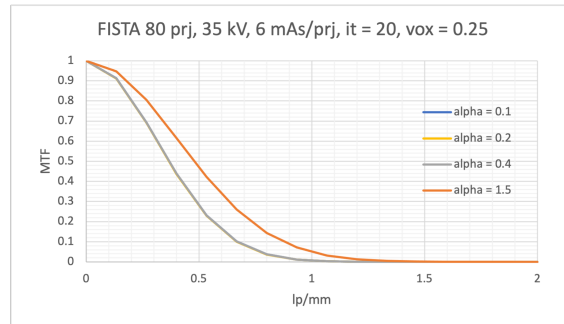
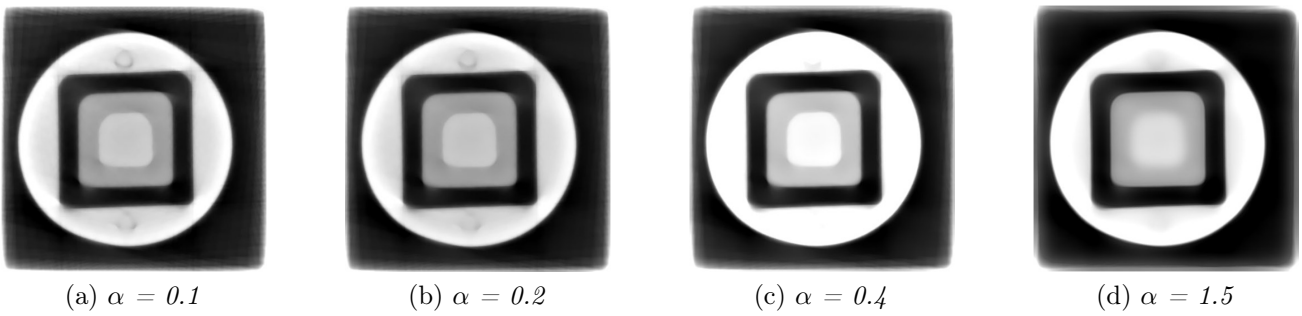


(e) $\alpha = 1.5$



(f) 60 projections, 30 kV, 2mAs/proj

Figure 5.19: Images and graph of the MTF as the α regularization parameter varies (0.1, 0.2, 0.4 0.8, 1.5). The parameters set at 60 projections, 30 kV, 2mAs for projection, 20 iterations and 0.25 voxel dimension. For the FISTA reconstruction method.



(e) 60 projections, 30 kV, 2mAs/proj

Figure 5.20: Images and graph of the MTF as the α regularization parameter varies (0.1, 0.2, 0.4 0.8, 1.5). The parameters set at 80 projections, 35 kV, 6mAs for projection, 20 iterations and 0.25 voxel dimension. For the FISTA reconstruction method.

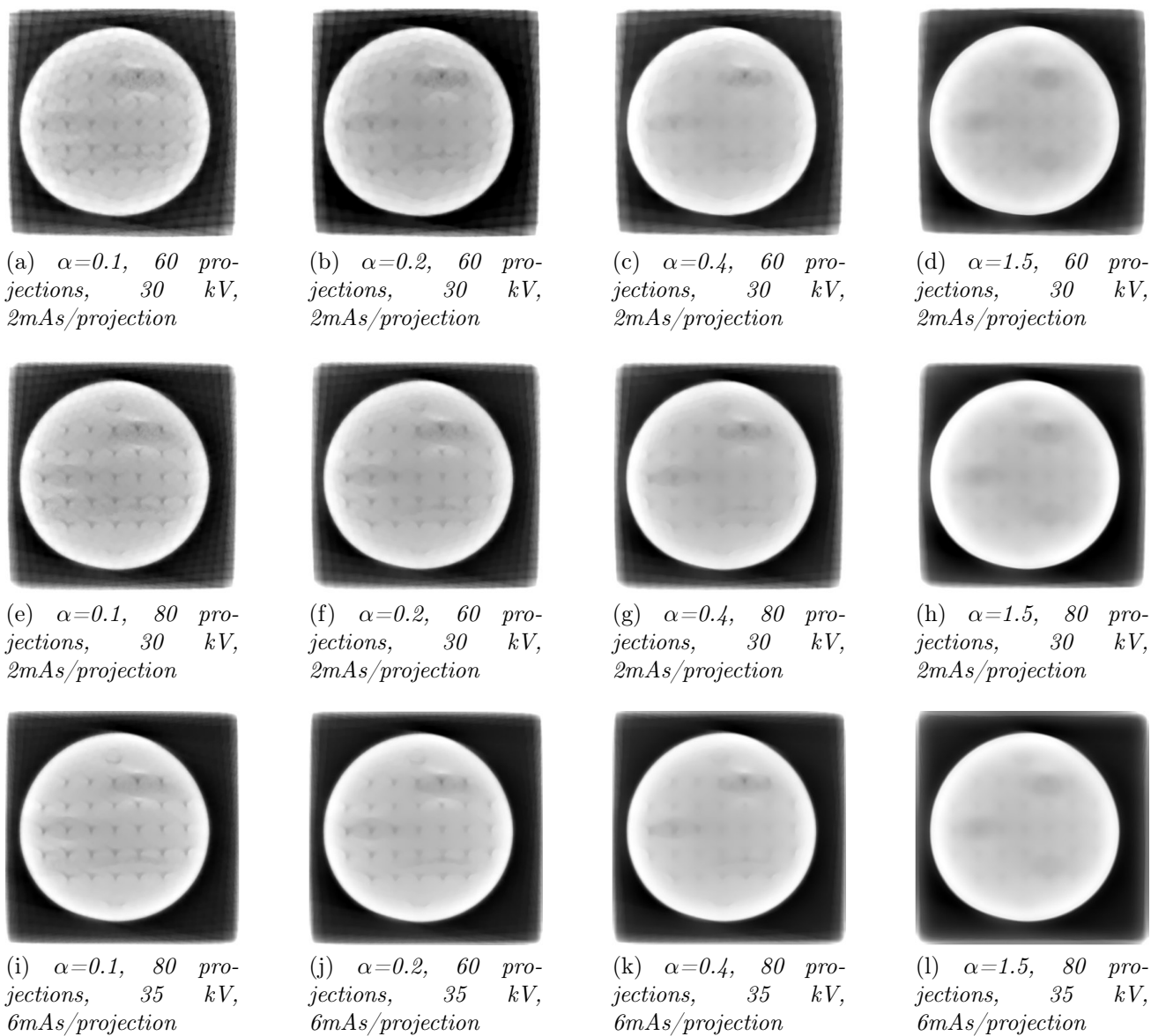


Figure 5.21: Images of the 1 mm holes layer, used for the evaluation of geometric distortions, as the α regularization parameter varies (0.1, 0.2, 0.4, 1.5). For 60 and 80 projections and for 30, 35 kV in the last case. For the FISTA reconstruction method.

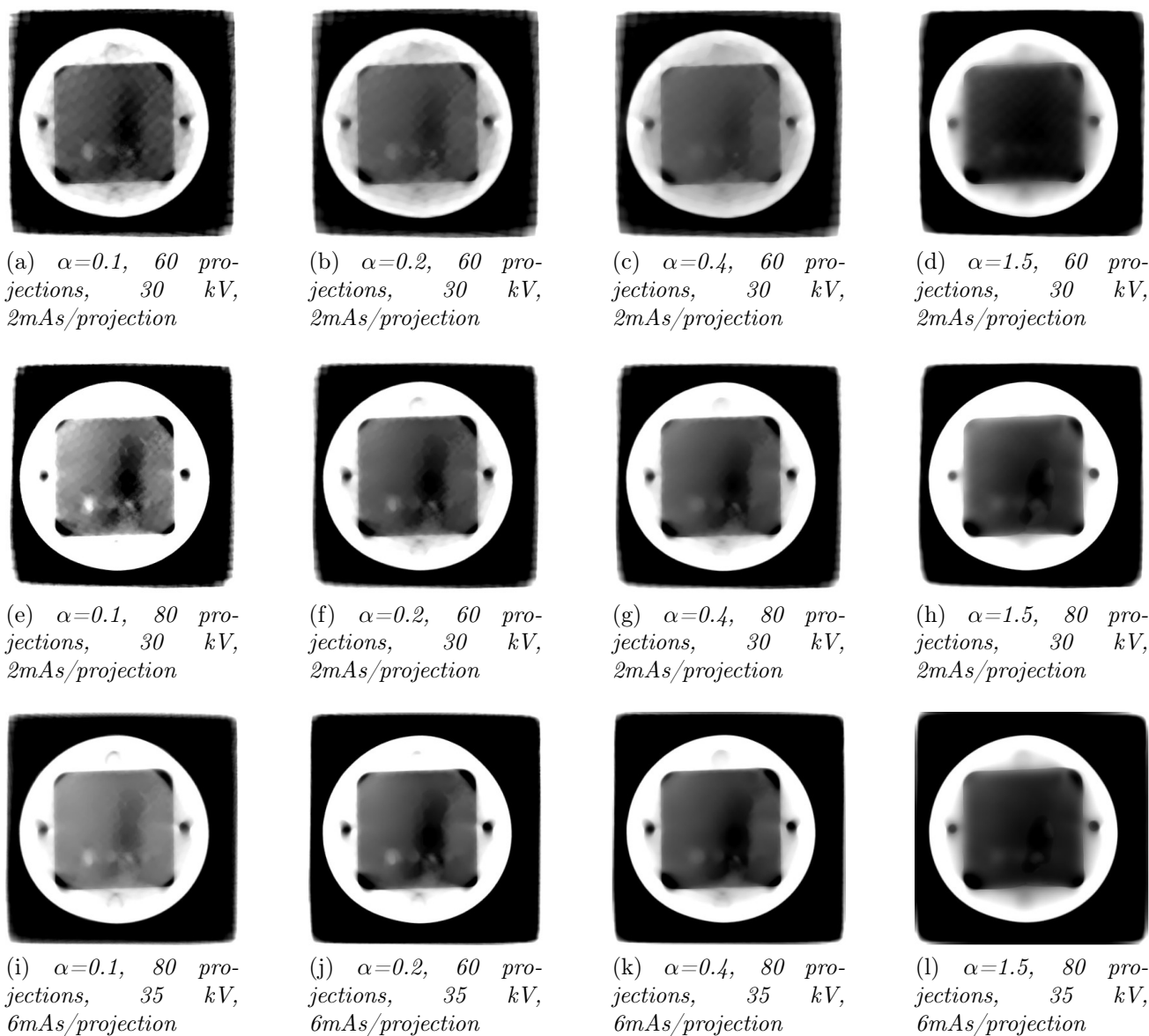


Figure 5.22: Images of the clinical details layer as the α regularization parameter varies (0.1, 0.2, 0.4, 1.5). For 60 and 80 projections and for 30, 35 kV in the last case. For the FISTA reconstruction method.

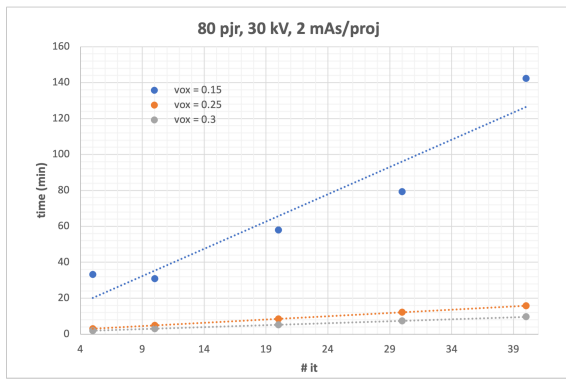
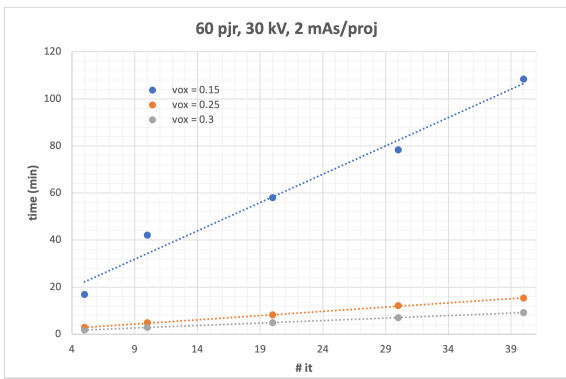


Figure 5.23: The graph shows the trend of the reconstruction time with the increasing number of iterations for different voxel dimensions in different dose setups case. For the FISTA reconstruction method.

Bibliography

- [1] Robert Bujila and Artur Omar and Gavin Poludniowski, *A validation of SpekPy: A software toolkit for modelling X-ray tube spectra*, Physica Medica, 2020, <https://doi.org/10.1016/j.ejmp.2020.04.026>
- [2] Jae Joon Hwang, Hyok Park, Ho-Gul Jeong, Sang-Sun Han, *Change in Image Quality According to the 3D Locations of a CBCT Phantom*, Plos One, 2016, [10.1371/journal.pone.0153884](https://doi.org/10.1371/journal.pone.0153884)
- [3] Wei Kang, Wuning Zhong and Danke Su, *The cone-beam breast computed tomography characteristics of breast non-mass enhancement lesions*, Acta Radiologica, 2020, [10.1177/0284185120963923](https://doi.org/10.1177/0284185120963923)
- [4] Gerald R. Torgersen et al., *A phantom for simplified image quality control of dental cone beam computed tomography units*, 2014, <http://dx.doi.org/10.1016/j.oooo.2014.08.003>
- [5] Avice O'Connell et al., *Cone-Beam CT for Breast Imaging: Radiation Dose, Breast Coverage, and Image Quality*, AJR, 2010, [10.2214/AJR.08.1017](https://doi.org/10.2214/AJR.08.1017)
- [6] Cherie Marie Kuzmiak et al., *Dedicated Three-dimensional Breast Computed Tomography: Lesion Characteristic Perception by Radiologists*, Journal of Clinical Imaging Science, 2016, [10.4103/2156-7514.179428](https://doi.org/10.4103/2156-7514.179428)
- [7] Ruben Pauwels et al., *Development and applicability of a quality control phantom for dental cone-beam CT*, Journal of applied clinical medical physics, 2011
- [8] J. H. Siewerdsen et al., *Cone-beam CT dose and imaging performance evaluation with a modular, multipurpose phantom*, American Association of Physicists in Medicine, 2019, <https://doi.org/10.1002/mp.13952>
- [9] Hsin Wu Tseng et al., *Radiation dosimetry of a clinical prototype dedicated cone-beam breast CT system with offset detector*, American Association of Physicists in Medicine, 2021, <https://doi.org/10.1002/mp.14688>

- [10] Yueqiang Zhu et al., *Dedicated breast CT: state of the art—Part I. Historical evolution and technical aspects*, European radiology, 2021, <https://doi.org/10.1007/s00330-021-08179-z>
- [11] Arthur G. Haus et al., *Image Quality in Mammography*, Diagnostic Radiology, 1977
- [12] Ehsan Samei et al., *A method for measuring the presampled MTF of digital radiographic systems using an edge test device*, American Association of Physicists in Medicine, 1997
- [13] Antonio Sarno et al., *Monte Carlo evaluation of glandular dose in cone-beam X-ray computed tomography dedicated to the breast: Homogeneous and heterogeneous breast models*, Physica Medica, 2018, <https://doi.org/10.1016/j.ejmp.2018.05.021>
- [14] J. Nederend et al., *Impact of transition from analog screening mammography to digital screening mammography on screening outcome in The Netherlands: a population-based study*, Annals of Oncology, 2012, 10.1093/annonc/mds146
- [15] Elham Abouei, *The influence of filtration, tube current and number of projections on CBCT image quality*, Sharif University of Technology, Vancouver, 2014
- [16] Marina Carozza, *Ricostruzione di immagini 3D per Cone Beam Breast Computed Tomography*, Alma Mater Studiorum, University of Bologna, Bologna, 2021
- [17] Adeola Olubamiji, *Quantitative performance characterization of image quality and radiation dose for dental CBCT machine*, Tampere University of Technology, 2011
- [18] Megan Alexis Brydon, *Transition to full-field digital mammography: the impact of technology change on mammography volumes in nove scotia*, Dalhousie University, Bologna, 2018
- [19] Steve Si Jia Feng, *Enhancing the image quality of digital breast tomosynthesis*, Georgia Institute of Technology and Emory University, Georgia, 2013
- [20] Guang Yang, *Numerical Approaches for Solving the Combined Reconstruction and Registration of Digital Breast Tomosynthesis*, University College London, London, 2012

- [21] N. Perry, M. Broeders, C. de Wolf, S. Törnberg, R. Holland, L. von Karsa, *European guidelines for quality assurance in breast cancer screening and diagnosis, fourth edition*, European Communities, 2006, 92-79-01258-4
- [22] N. Perry, M. Broeders, C. de Wolf, S. Törnberg, R. Holland, L. von Karsa, *European guidelines for quality assurance in breast cancer screening and diagnosis, fourth edition, supplements*, European Union, 2013, 978-92-79-32970-8
- [23] *International standard IEC, 62220-1-2*, IEC Central Office, 2007
- [24] Hugo de las Heras Gala et al., *Quality control in cone-beam computed tomography (CBCT) EFOMP-ESTRO-IAEA protocol*, 2019, <http://dx.medra.org/10.19285/CBCTEFOMP.V1.0.2017.06>
- [25] Gisella Gennaro et al., *Quality controls in digital mammography protocol of the EFOMP MAMMO working group*, 2015
- [26] Koning Corporation, *User's Manual for the Koning Breast CT System*, www.koningcorporation.com
- [27] J M Boone 1 , T R Fewell, R J Jennings, *Molybdenum, rhodium, and tungsten anode spectral models using interpolating polynomials with application to mammography*, *Med Phys.*, 1997, 10.1118/1.598100
- [28] Dance, *Monte Carlo calculation of conversion factors for the estimation of mean glandular breast dose*, *Phys Med Biol.*, 1990, 10.1088/0031-9155/35/9/002